# Discharge instabilities in high-pressure Fluorine based excimer laser gas mixtures

Discharge instabilities in high-pressure fluorine based excimer laser gas mixtures

By Denny Mathew

Ph.D. Thesis, University of Twente, Enschede, The Netherlands, 2007.
ISBN: 978-90-365-2503-9



Printed by Wöhrmann Print Service, Zutphen, The Netherlands, 2007.

The work described in this thesis was performed at the Laser Physics and Non-linear Optics group, Faculty of Science and Technology, University of Twente, P.O. Box 217, 7500 AE Enschede, The Netherlands. This research was supported by the Technology Foundation STW (project number TTF.5696), applied science division of NWO and the technology programme of the ministry of Economic Affairs.

# DISCHARGE INSTABILITIES IN HIGH-PRESSURE FLUORINE BASED EXCIMER LASER GAS MIXTURES

## DISSERTATION

to obtain
the doctor's degree at the University of Twente,
on the authority of the rector magnificus,
prof. dr. W.H.M. Zijm,
on account of the decision of the graduation committee,
to be publicly defended
on Friday, 27th April 2007 at 13.15

by

**Denny Mathew**
born on $16^{th}$ April 1979
in Kolenchery, Kerala, India

This thesis has been approved by,

Promotor: Prof. K. J. Boller

Assistant Promotor: Dr. H. M. J. Bastiaens

*To My Family & Sabichayan*

# Contents

# Chapter 1

# General Introduction

Since the invention of the first laser half a century ago, lasers are now wide-spread and highly important tools in science and industry. According to the gain medium used, lasers can be classified as gas lasers, solid state lasers, liquid (dye) lasers, free electron lasers, semiconductor lasers and their wavelengths cover almost the entire spectral range from the far infrared to short wavelengths such as in the ultraviolet and beyond.

An essential precondition to obtain laser emission is a sufficiently strong light amplification. This is obtained via providing a population inversion in the laser medium, i.e., where the upper laser level carries more population than the lower laser level. In most of the named spectral ranges, particularly in the infrared, there are a number of different pump mechanism available to provide the required inversion, even when the lower laser level remains populated to a significant degree. However, when moving towards short wavelengths, such as in the ultraviolet, creating a strong population inversion becomes increasingly difficult because here spontaneous emission rapidly empties the upper laser level. As a result, ultraviolet lasers require, for their operation, very strong and, therefore, pulsed pumping. Additionally, the lower laser level of the gain medium should decay extremely rapidly such that no inversion-reducing population can collect there. In order to fulfill these conditions and thereby provide laser radiation in the ultraviolet, Houtermans proposed in 1960 to use, as the laser medium, special gas molecules which are stable in the upper energy level, such that pumping can collect population here, but where the lower laser level is unstable [1]. In 1971, Basov demonstrated the first laser based on this principle [2]. In his experiments he used a

pulsed discharge to form Xenon-dimer molecules in a stable and highly excited state ($Xe_2^*$) while the ground state of that molecule ($Xe_2$) rapidly decays into two separate Xe atoms. The wavelength of this first type of excited dimer laser, now commonly called excimer laser, fell in the range of the vacuum ultraviolet (VUV), at 172nm. However, since then, quite a number of excimer lasers based on other molecules were realized with wavelengths ranging from about 660 nm to 126 nm. Today, excimer lasers are well known for their high efficiency and capability to generate high output powers (up to GW's) in the ultraviolet(UV) and vacuum-ultra violet(VUV) part of the electromagnetic spectrum. The named properties, in particular the combination of short wavelength and high power have led to a widespread commercial availability and use in applications.

However, in spite of this widespread use and a correspondingly high maturity of the involved technology of excimer lasers, an absolutely central and fundamental problem with excimer lasers, particularly for those with the shortest wavelengths, has remained largely unsolved. This problem, as will be detailed below, is that the spatial quality of the laser output beam remained rather poor and, in fact, resembles more that of a directional lamp-like source. Actually this is a tremendous disadvantage for numerous applications. The goal of this thesis is to investigate the physical reasons for such lack of beam quality in those excimer lasers that provide the shortest available wavelengths, namely Fluorine based excimer lasers. A second goal of this thesis is to, possibly, identify a method that can eliminate this problem and thereby would open up a wide-spread range of improved or even novel applications of such high-beam quality Fluorine based excimer lasers. For a more detailed view on the underlying problems and the named objectives of this thesis, we present in the following a brief overview on the working principle and pumping technology of such excimer lasers, in particular the Fluorine based excimer lasers.

## 1.1 Basic principle of an excimer laser

An excited dimer is a class of molecules that is formed by the combination of two identical atoms in the excited state. Examples of such excited dimers are $Ar_2^*$, $Kr_2^*$, $Xe_2^*$, $Hg_2^*$, $Cd_2^*$. However, the most common excimer molecular lasers with a dissociating ground state used today are based on two different atoms, a rare gas atom bound to a halide atom. These rare gas monohalides can be formed under certain excitation conditions from Ar, Kr, or Xe and F or Cl. Among all known excimers, the $F_2$-based excimers ($F_2$, ArF and KrF) are the most important ones as they offer the shortest wavelengths and have a high potential for applications. A list of the most

common excimer lasers and their lasing wavelengths are shown in Table 1.1.

| | Halogen | Rare gas halides | | | | | |
|---|---|---|---|---|---|---|---|
| Excimer molecules | $F_2$ | ArF | KrCl | KrF | XeBr | XeCl | XeF(B-X) |
| Wavelength | 157 | 193 | 222 | 248 | 262 | 308 | 351 |

*Table 1.1: Emission wavelengths of the most common excimer lasers. It can be seen that the shortest wavelengths are offered by $F_2$-based excimer molecules, particularly $F_2$, ArF, and KrF (taken from refs. [3–6]).*

Figure 1.1 shows a schematic potential energy diagram of an example of a $F_2$-based excimer molecule, namely $ArF^*$ [6]. The upper state consists of two levels B (upper curve) and C (lower curve), which may be treated at low internuclear spacing as a single state [6–8]. The lower states A and X can also be considered as a single state [6–8]. It can be seen in the figure that $ArF^*$ has a minimum in its potential energy curve so that the excited state exists as a vibrating molecule in an electronic state. The excited molecule $ArF^*$, can give up its excess energy by undergoing spontaneous or stimulated emission, in a transition to the repulsive ground state, which very quickly dissociates into two unbound atoms of Ar and F. Thus, population inversion for the laser transition is readily achieved in these class of molecules, which makes them an ideal candidate for lasers. However, due to the short wavelength and broad line profiles of the transition, high pump power densities (in the order of MW $cm^{-3}$) are required for the excitation of excimer lasers. Such high pump power densities in high pressure gas mixtures can only be reached in pulsed systems.

The excitation technology for excimer lasers is based either on high-energy electron-beams (e-beam) that deposit their energy in the laser gas [9–11] or self-sustained glow discharges [12–16]. Sometimes, a combination of both techniques can be advantageous as demonstrated in e-beam sustained discharge systems [17–19]. However, the self-sustained discharge pumping of an excimer laser is easier to implement and has many advantages such as high repetition rate operation and generation of high average powers reaching the kW level, such that by now almost all excimer lasers, particularly in industrial applications, are pumped this way.

## 1.2 Goal and research overview

As seen above, among the various types of excimer lasers, the $F_2$-based lasers are of highest interest because they offer the shortest wavelengths. As an example, the short

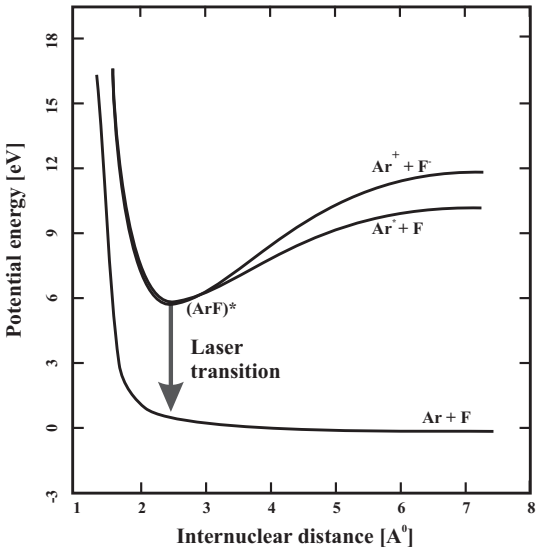


*Figure 1.1: Schematic potential energy diagram of a $F_2$-based excimer molecule, namely $ArF^*$, showing the main formation channels and radiative transition to the repulsive lower level [3].*

wavelengths makes them suited best for numerous applications in nano-lithography, material processing, micro-machining and surface ablation. However, the low beam quality, far below the fundamental diffraction limit, of the output radiation limits extensive usage of these lasers in precision applications like multiple hole drilling and micromachining of metals, glasses and various kind of composites. The reason for the low beam quality is that in these lasers oscillation terminates typically after 20 to 30 ns, such that the number of round trips within the resonator is insufficient rendering an output which mostly consists of amplified spontaneous emission.

This short duration of oscillation can be traced back to a fundamental problem in the pump mechanism. In high-pressure glow discharges, spatio-temporal instabilities, called streamer formation, filamentation or micro-arc formation, force the laser pulse to terminate before the end of the pump pulse [20–24], as described below. When discharge instabilities occurs, the plasma volume and thus the spatial region where light amplification occurs, shrinks or constricts into one or more tiny filaments whose axes

directed along the applied electric field. Due to a poor overlap with the laser beam, this terminates the initial phase of efficient pumping. In addition, the nonuniform distributions of the refractive index in the inhomogeneously excited medium refractively and diffractively perturbes the beam which had built up so far. The premature termination of the homogeneous phase of the discharge, together with ineffective excitation due to the nonuniform current distribution in the presence of severe arcing, leads to the termination of the laser pulse well before the end of the discharge pumping current pulse. In view of these problems and in order to still obtain at least a high pulse energy (though with low beam quality), the present strategy of excitation is to deposit as much energy into the medium as possible, before filamentation sets in. This, however, leads to yet another drawback. The high peak intensity associated within the resulting short laser pulse quickly causes damage to the optical components.

Thus, identifying the origin of these discharge instabilities and eliminating them is a highly desired goal. This is true especially for $F_2$-based lasers because, here, the named instabilities are strongest, while the promise for short wavelength and high-quality radiation is greatest.

## 1.3 Outline of the thesis

The objective of this thesis is to find the cause of the discharge instabilities and to eliminate or suppress the growth of these instabilities, thereby extend the homogeneous phase of the discharge in Fluorine based excimer laser gas mixtures. For this purpose, a small volume x-ray preionised discharge set-up is built and optimized for the optical monitoring of the onset and development of discharge instabilities in Fluorine based excimer laser gas mixtures. The spatial and temporal development of the discharge is recorded via its fluorescence with a fast, intensified gated CCD camera (ICCD) having a minimum gating time of 300 ps. Our extensive experimental investigations in this optimised set-up succeeded to identify the cause of the origin of the discharge instabilities and to extend the stable phase of the discharges in $F_2$-based excimer laser gas mixtures.

A brief outline of this thesis is as follows. Chapter 2 discusses the key issues associated with the homogeneous initiation of a self-sustained high-pressure glow discharge in $F_2$-based excimer laser gas mixtures. The experimental set-up and its characterisation are given in Chapter 3. Here, the optimum starting conditions required for the initiation of a homogeneous discharge are determined experimentally and described. In chapter 4, the experimental results on the dependence of spatio-temporal devel-

opment of discharge instabilities on the electrode materials and its surface roughness are presented. In this chapter we present a new method to quantitatively analyse the discharge quality so as to provide a measure for the discharge homogeneity which can be compared with the prediction of theoretical models. Chapter 5 presents a detailed experimental characterization of discharge instabilities in $F_2$-based excimer laser gas mixtures ($F_2$, KrF, ArF). After identifying the cause of discharge instabilities, further experiments are focused on ways to stabilise and extend the homogeneous phase of the discharge in $F_2$-based excimer laser discharges. Chapter 6 reports on the effect of the buffer gas (either He or Ne) and on the effect of addition of small amounts of heavy rare gases like Xe or Kr on the discharge uniformity in $F_2$ and ArF excimer laser gas mixtures.

# Chapter 2

# High-pressure discharges in excimer laser gas mixtures

Fluorine based excimer lasers such as KrF, ArF and $F_2$ are generally pumped by pulsed high-pressure transversal glow discharges. In this chapter, a brief description is given of the main kinetic reactions involved in the formation of excimer molecules, as well as the key issues associated with the initiation of a high-pressure glow discharge in excimer laser gas mixtures. Additionally, the mechanisms that drive the formation of instabilities in large-volume, high-pressure excimer laser gas discharges are reviewed.

## 2.1 Self-sustained discharge-pumped excimer lasers

Discharge excitation forms a convenient method for the pumping of excimer lasers [16, 25–33]. The required upper state population in the lasing medium in which the population inversion is provided by means of a glow discharge [34]. The laser gas mixtures are typically at multi atmospheric pressure and consist of a small amount (about 0.1%) of a halogen or a halogen containing molecule (e.g. HCl or $F_2$), about 10% of a heavier rare gas (Ar, Kr or Xe) and a lighter rare gas, called the buffer gas (He or Ne). Although excimers are to be formed only by the rare gas and halogen atoms, a buffer gas must be added to decrease the otherwise large momentum transfer cross section of the mixture [35]. The cross sections for the electron impact momentum

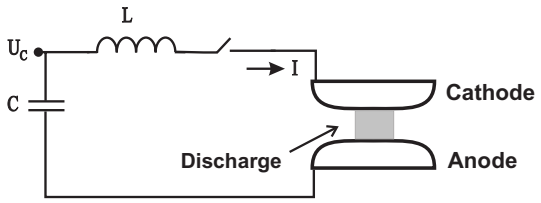


*Figure 2.1: Basic electrical scheme used to pump gas lasers*

transfer cross sections, $\sigma_m$, of Ar, Kr and Xe exceed 10 $\AA$ for energies in the range of 5-10 eV. These relatively high values of $\sigma_m$ would require high operating and breakdown voltages for large aperture discharges (greater than a few centimeters). Therefore, the average $\sigma_m$ of the rare gas/halogen mixture is reduced by diluting with either He or Ne, both of which have much lower $\sigma_m$ compared to the heavier rare gases.

The basic electrical circuit used for discharge excitation of excimer lasers is shown in Fig. 2.1. A capacitor C, charged to a voltage $U_c$, is applied to the discharge electrodes through a switch , e.g., a spark gap or saturable inductors. Free electrons present in the laser gas mixture, usually produced by an external preionisation source, are accelerated towards the anode under the influence of the applied electric field ($E = U/d$, where U is the voltage applied at the electrodes and d is the electrode gap). This causes the initially low level of ionisation within the discharge gap to grow exponentially via an electron avalanche, until the discharge impedance becomes limited by the output impedance of the driving electrical circuit [36]. At this point, the discharge reaches the so-called steady state as will be discussed in Sec. 2.1.2, such that the voltage across the discharge gap varies very little with increasing current. This regime of the discharge is called the glow discharge regime [34]. In this regime the laser gas is only weakly ionised by the discharge with a low fractional ionisation of about of $10^{-5}$ - $10^{-4}$. The mean electron energy in the plasma is in the order of a few electron volts.

For the excitation of the discharge different driving circuits are in use. Examples are the charge transfer circuit which provides a single excitation pulse [37–41] and the pre-pulse main-pulse circuit which generates a double-excitation pulse [42–48]. Instead of using a standard switch in the driving circuit like a spark gap, rail gap or a saturable inductor, the laser gas discharge itself can also be used as a switch [49–51]. The advantage of the charge transfer circuit is that it is technically simple to realise. The pre-pulse main-pulse circuit on the other hand, though technically more involved,

provides a more efficient transfer of energy by voltage matching. For the excitation of discharges in our test cell we used a pulse forming line that provides a rectangular current pulse suited for the study of the temporal development of discharges [41].

### 2.1.1 Discharge kinetics

The production of excimer molecules in a self-sustained volume-stabilised glow discharge relies on complex formation processes in the discharge plasma. The electrical excitation of the gas mixture results mainly in the formation of excited atoms and atomic ions of the heavy rare gas (for rare gas-halide excimers) or of the dominant buffer gas (e.g. He in $F_2$ laser gas mixture). Only a small part of the ions is generated by direct impact ionisation. The reason for this is that the mean electron energy in the discharge is only a few eV, such that just a small fraction of the electrons, those in the high-energy tail of the energy distribution, are capable of directly ionising the gas [6]. The major part of ions are formed by two or multi-step ionisation processes. From the energy deposited in the discharge, only a small part is used for the production of excited and ionised atoms or molecules and the major part of the energy is lost in elastic collisions with heavy atoms and molecules. The formation of the desired excimer molecule ($ArF^*$ in ArF and $F_2(D')$ in $F_2$ lasers) occurs at the end of the kinetic reaction chain. Depending on the specific excimer, there can be more than 60 different reactions occurring in the discharge and here, only the most important reactions are addressed. A detailed description of the major chemical reactions in ArF and $F_2$ laser discharges can be found in [24, 52].

The electrons in the high energy tail of the electron energy distribution function excite or directly ionise rare gas atoms via inelastic collisions:

$$\mathrm{Rg} + e \rightarrow \mathrm{Rg}^* + e \tag{2.1}$$

$$\mathrm{Rg}^* + e \rightarrow \mathrm{Rg}^+ + 2e \tag{2.2}$$

$$\mathrm{Rg} + e \rightarrow \mathrm{Rg}^+ + 2e \tag{2.3}$$

where Rg denotes a rare gas atom.

The negative Fluorine ion which is a precursor in the formation channel for excimer molecules in $F_2$-based discharges is produced in a fast exothermic dissociative attachment reaction [53] such as:

$$\mathrm{F}_2 + e \rightarrow \mathrm{F}^- + \mathrm{F} \tag{2.4}$$

The main kinetic processes which lead to the formation of the excimer laser molecules in the ArF and $F_2$ lasers are discussed below.

### ArF laser

The discharge excited ArF laser [54–56] operates in gas mixtures with small amounts of Ar and $F_2$ admixed with He or Ne as buffer gas. The excited complex, $ArF^*$, which is the lasing species in the ArF laser is formed by two main processes [57–59]:

(a) Neutral channel or harpooning reaction:

$$Ar^* + F_2 \rightarrow ArF^* + F \tag{2.5}$$

(b) Ion channel reactions:

$$Ar^+ + F^- + Rg \rightarrow ArF^* + Rg \tag{2.6}$$

and:

$$Ar_2^+ + F^- \rightarrow ArF^* + Ar \tag{2.7}$$

For discharge pumped KrF lasers [37, 60–62], the same gas mixture is used except that Ar is replaced by Kr. Usually, He is used as buffer gas [63–65] and the kinetic processes in the KrF laser are very similar to those in ArF laser.

### $F_2$ laser

The discharge excited $F_2$ laser [30, 66, 67] operates in gas mixtures of Helium with a small content of Fluorine. The upper laser level $F_2(D')$ in the $F_2$ laser can also be formed via both a neutral channel reaction (energy transfer) and an ion channel reaction (ion-ion recombination) [68, 69]:

(a) Neutral channel reaction:

$$F^* + F_2 \rightarrow F_2^*(D') + F \tag{2.8}$$

where F* indicates a low lying excited state of the F atom.

(b) Ion channel reaction (ionic recombination):

$$F^- + F^+ + Rg \rightarrow F_2^*(D') + Rg \tag{2.9}$$

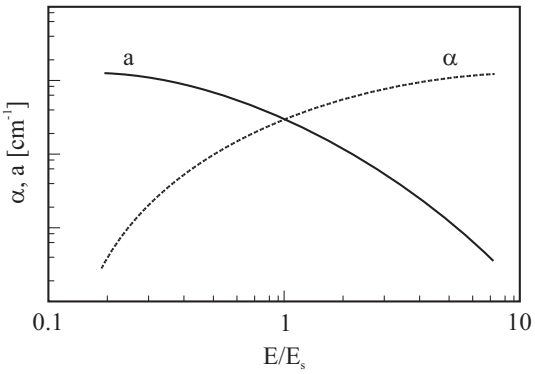


*Figure 2.2: Schematic diagram of the ionisation coefficient, $\alpha$, and the attachment coefficient, a, as a function of the electrical field (E) normalised on the steady-state field ($E_s$) (Taken from [24, 70]).*

### 2.1.2 Steady-state operation

After the breakdown, the electric field E across the discharge settles at a value such that the electron production and the electron loss rates are in equilibrium. In an excimer laser discharge, electron loss by diffusion is negligible, and ionic recombination ($Rg + Rg^+ + e \rightarrow Rg + Rg$) or dissociative recombination (${Rg_2}^+ + e \rightarrow Rg + Rg^*$) is a minor loss mechanism, since the rates for these reactions are much slower than those of the electron loss by attachment (see Eq. 2.4). Therefore, the steady-state electric field $E_s$ settles at that value which results in a balance between the electron-impact ionisation (Eq. 2.2 and 2.3) and the electron loss by attachment to the halogen donor (Eq. 2.4). The rate equation can be written as:

$$\frac{dn_e}{dt} = n_e \left[\alpha(E) - a(E)\right] v_{\mathrm{d}}(E) \tag{2.10}$$

where $n_e$ is the number of electrons, $\alpha(E)$ is the first Townsend ionisation coefficient for the gas mixture, $a(E)$ is the electron attachment coefficient, $v_{\mathrm{d}}(E)$ is the drift velocity of the electrons in the electric field.

The ionisation coefficient, $\alpha$, and attachment coefficient, a, are functions of the electric field strength, E. The ionisation coefficient, $\alpha(E)$, increases with the electric field whereas the attachment coefficient, $a(E)$, decreases with electric field as shown in Fig.

2.2. The intersection of these two curves [i.e., $\alpha(E) = a(E)$] determines the operating steady-state field ($E_s$) of the discharge and with that the steady-state voltage ($V_s$) for a given electrode distance. If the voltage is increased above the steady-state voltage, more ionisations and less attachment will occur and consequently the electron density increases. This means that more current is flowing through the discharge. Then the voltage across the impedance of the driving circuit will increase and the voltage across the discharge electrode will drop back to the steady-state voltage. The ionisation and attachment rates will be again in balance, however, at a higher current flowing through the discharge.

In steady-state, the voltage drop across the electrodes is independent of the current through the discharge [36]. $F_2$-based excimer lasers are excited in a pulsed glow discharge under steady-state operating conditions. As it is shown in Sec. 2.1.1, the chain of kinetic reactions leading to the formation of excimer molecules in gas discharges is mainly based on three body collisions (Eq. 2.6 and 2.9). For those collisions to be effective, it is required to work at multi-atmospheric gas densities. This fundamental condition has a strong impact on the discharge stability of $F_2$-based excimer laser gas mixtures: such multi-atmospheric self-sustained discharge systems are, by nature, mostly unstable [34, 71–73] as explained below.

## 2.2 Initiation of a high-pressure glow discharge

At moderate to high pressures, the electric breakdown of a gas between two parallel electrodes can occur by two different breakdown mechanisms [34, 71–73], namely the conventional Townsend (or Paschen) mechanism or the streamer (or Kanal) breakdown mechanism. For both types, the primary breakdown process is a collisional electron avalanche that develops in the gas when a sufficiently strong, homogeneous electric field is applied to it via the electrodes.

Townsend breakdown occurs when the space charge electric field is negligible compared to the applied electric field. The exponential increase of the electron current within the discharge gap is assumed to be maintained by a positive feedback to the Townsend avalanche process through secondary electron emission at the cathode surface, e.g., emission of electrons by ion bombardment and through the photoelectric effect. This gives rise to the well known Paschen-breakdown law [34]:

$$p\,d\,(\alpha/p) = ln\left(1 + \frac{1}{\gamma}\right) \tag{2.11}$$

where p is the gas pressure, d is the electrode gap, $\alpha$ is the first Townsend coefficient and $\gamma$ is the second Townsend coefficient, which describes the effective secondary electron emission from all sources associated with a primary single electron, including positive ion bombardment and the photoelectric effect. This kind of breakdown mechanism will normally give rise to a self-sustained homogeneous glow discharge for low pd values ($<$ 260 cm mbar) at small overvoltages (low E/N) with a relatively long formative time delay ($\sim 10^{-6}$ sec).

### 2.2.1 Streamer or Kanal breakdown

At high pd values and considerable higher voltages, the breakdown mechanism does not rely on the secondary electron generation at the cathode surface because the current conducting channel is formed much faster than the time needed for an ion to cross the electrode gap, so that the Townsend breakdown model is not applicable. The quick multiplication of electrons in the discharge gap gives rise to a rapidly growing space charge field which becomes comparable to the applied electric field [34, 71–73]. The condition, under which a streamer breakdown takes place, is given by the equality of the space charge field to the applied electric field and is known as Raether's criterion which is (in air, in m.k.s.units):

$$p\,d \cdot (\alpha/p) = 20 \; + \; ln\; d \tag{2.12}$$

Streamer breakdown theory is based on the concept of the growth of a thin ionized channel called streamer [74, 75] as illustrated in Fig. 2.3. When a sufficiently high electric field is applied to a gas volume, an avalanche starts from an electron present in the gas, for example by natural ionisation as from cosmic radiation. Due to the electric field this electron gains sufficient kinetic energy to ionise an atom or molecule thereby producing a second electron and so on. This local avalanche propagates under the influence of the applied electric field by ionising collisions. The positive ions generated have a relative low mobility compared to electrons and can be considered at rest. This leads to a space charge formation which gives rise to an electric field. The propagating avalanche head is filled mostly with free electrons and can be idealised as a negatively charged sphere which leaves behind a positive space charge cone as shown in Fig. 2.3(a). The shape of this avalanche cone is determined mainly by electron diffusion.

When the space charge field of the avalanche head becomes comparable to that of the applied electric field, streamer development begins. A crucial role is played by the energetic photons that are emitted by the excited atoms in the avalanche head. These

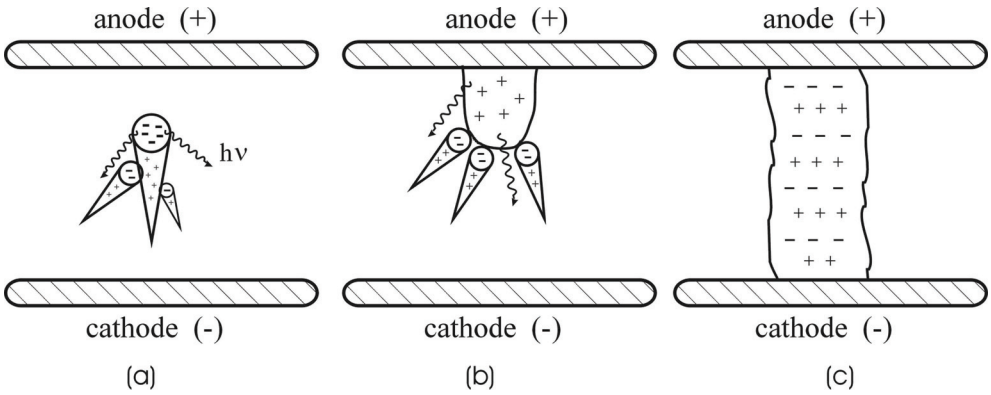


*Figure 2.3: Schematic diagrams showing (a) streamer development around a single primary electron avalanche when its space charge field is comparable to the applied electric field, (b) continuous backward propagation of the cathode-directed plasma streamer after the arrival of the primary avalanche head at at the anode, and (c) completed bridging of the electrode gap by the plasma streamer. (Taken from [75])*

photons produce electrons, by photoionisation, which initiate secondary avalanches in the vicinity of the primary avalanche. The negative heads of secondary avalanches are attracted towards the primary positive space charge cone under the strong influence of the high local space charge field and a quasi neutral plasma is formed. New photons are also created during this process by the excitation of atoms. The secondary avalanche ions enhance the positive space charge near the cathode and this attracts the electrons of the next generation avalanche. This way an ionised thin channel grows rapidly towards the cathode, which is called a cathode directed streamers (Fig. 2.3(b)).

The electrons in the primary avalanche head are accelerated towards the anode in the enhanced electric field (resultant of applied field and space charge field) and form a so-called anode directed streamer. The negatively space charged avalanche head propagates towards the anode and the positive space charge left behind the head grows towards the cathode until these self-propagating streamers connect the anode and cathode as shown in Fig. 2.3(c). The formative time delays for streamer breakdown can be as short as $10^{-9}$ sec.

Excimer laser gas discharges, generally, operate at high *pd*-values and need consider-

able over-voltages for breakdown. This imply high E/N values for these discharges. In our experimental setup *pd* amounts to 3.4 cm bar and E/N to about 25x$10^{-17}$ V $cm^2$. At these values, the space charge field imparts a strong local gradient in the applied electric field and then the second equation (Eq. 2.12) is easily satisfied (i.e., $\alpha\, d > 20$). Clearly, these high-pressure discharges rather favour a streamer mode of initiation than a Townsend (glow like) mode of initiation. The current density in the streamers is higher than in the bulk of the discharge which results in a non-uniform energy deposition in the discharge and causes arcing in the discharge chamber. It should be noted that such arcing leads to a strong erosion of the electrodes. Most importantly, this streamer breakdown leads to a poor laser performance in terms of pulse duration and the output energy.

### 2.2.2 Suppression of streamer formation by preionisation

Streamer formation during the breakdown phase of the discharge can be inhibited by introducing a suitable number density of free electrons uniformly distributed over the whole volume prior to the initiation of the main discharge [74–76]. If the density of such preionisation electrons is high enough, the heads of primary avalanches start overlapping (see Fig. 2.4) before the space charge field becomes comparable with the applied electric field. Strong overlapping of the secondary ionisation generated by the individual primary avalanches will homogenise the plasma density in the discharge as well as smooths out the local gradients of the space charge field. In this way, the electron density can grow uniformly in the discharge volume via the avalanche process driven by the applied electric field, such that the steady state operation of a homogeneous glow discharge can be established without streamer formation.

The minimum preionisation electron density necessary to achieve overlap of the individual avalanches depends on the voltage rise time, gas pressure and various properties of the gas mixture such as electron drift velocity, diffusion coefficient and attachment coefficient, which governs the rate of change of the first Townsend coefficient ($\alpha$) as a function of the varying applied electric field. According to the calculations of Levatter and Lin [75], preionisation electron densities in the range of $10^6$ to $10^7$ are required for the homogeneous discharge formation in $F_2$-based excimer laser gas mixtures. The spatial uniformity of the preionisation electron density is considered important as it is necessary for achieving a proper overlap of the primary avalanches.

In $F_2$-based excimer laser gas mixtures, it is far more critical than in other mixtures because the generated preionisation electrons will be more rapidly quenched by dissociative attachment to $F_2$ (according to Eq. 2.4) when there is no voltage applied

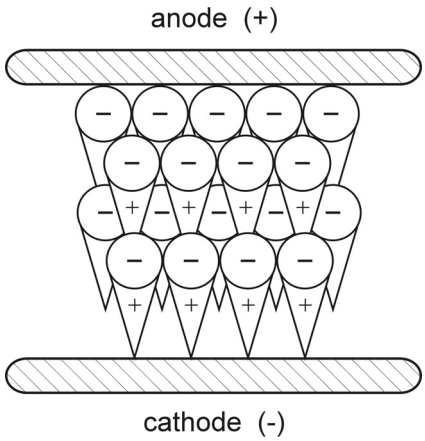


*Figure 2.4: The effect of a homogeneous pre-ionisation electron density: the avalanche heads and positive cones overlap, yielding a homogeneous plasma density and thus a homogeneous discharge.*

across the discharge electrodes. To diminish this effect, these mixtures should be preionised simultaneously with the application of the voltage across the electrodes. The preionisation electrons introduced to the gas volume at voltages higher than the steady state voltage will be not be lost due to attachment, since, for $V > V_s$, the ionisation rate is higher than the attachment rate as shown in Fig. 2.2. However, to obtain sufficient overlap of primary avalanches in this case, the preionisation source must produce the minimum required electron density on a time scale shorter than the time scale on which avalanches can develop to such an extent that streamer formation starts. Therefore, the preionisation should be applied in a short pulse (< a few tens of nanoseconds) or in a long pulse with a short rise time [24, 77, 78].

If the preionisation is applied while the electric field strength remains below the breakdown threshold, a significant amount of preionisation electrons produced in front of the cathode will be attracted by the anode leaving behind a spatial region deficient of free electrons (depletion region). Applying the preionisation on the rising edge of the voltage will help to minimise the depletion region in front of the cathode.

The overlap of the primary avalanches, shown in Fig. 2.4, would become better when the radius of the avalanche head is larger [75]. Decreasing the voltage rise time will result in a higher breakdown voltage of the gas discharge. A higher voltage on the

electrodes (due to high E/N) will allow the preionisation avalanche to grow to a larger size and a better overlap will be obtained. Moreover, application of a voltage pulse with a short rise time will decrease the depletion region in front of the cathode.

The effect of the preionisation on the initiation of the discharge is discussed in Ch.3 on the basis of experiments in $F_2$-based high pressure laser gas mixtures. The initial conditions required for the homogeneous initiation of a glow discharge, such as preionisation uniformity, minimum preionisation electron density and the optimum time delay between preionisation and the application of the voltage across the electrodes, are obtained from these experiments.

## 2.3 Discharge instabilities

Even under optimum preionisation conditions, instabilities appear in a homogeneously initiated discharge and after some time the discharge becomes filamentary in nature. Under these conditions the pump power is primarily deposited in small, randomly distributed thin channels of enhanced electron density in the bulk of the discharge, called filaments. The progressive growth of these filaments results in the collapse of the glow discharge into an arc which leads to the termination of lasing before the end of pump pulse [20, 21, 52, 67, 78–82]. The conditions for the onset of instabilities depend on a local imbalance between electron production and loss in the discharge. Consequently, the factors that cause the inhomogeneities are related to processes that control the density of electrons, viz. their production, loss/removal and spatial transfer rates.

The rate equation (a generalised version of Eq. 2.10) in a discharge is:

$$\frac{dn_e}{dt} = \textit{ electron production rate } - \textit{ electron loss rate} \tag{2.13}$$

The steady-state condition is:

$$\frac{dn_e}{dt} = 0 \tag{2.14}$$

In a stable discharge, the steady-state condition is always satisfied, i.e., electron production rate = electron loss rate. The electron density in steady-state is given by the steady-state electron density $n_{e0}$ which is ultimately determined by the magnitude of the discharge current, which is controlled by the impedance of the driving circuit.

A discharge becomes unstable when there is a local perturbation or deviation from the steady-state electron density:

$$\frac{\delta n_e}{\delta t} > 0 \tag{2.15}$$

Although the tendency of high-current discharges in high-pressure gas mixtures containing electronegative components to constrict into filamentary channels has been known for many years, a clear and definitive theoretical description of the constriction process is still not available. There are two main theoretical models available which explain the growth mechanism of instabilities in a high-pressure glow discharge, namely, the stepwise ionisation instability [22,23,83,84] and the halogen depletion instability [85–87].

### 2.3.1 Stepwise ionisation instability

The core idea of stepwise ionisation instability [22] is as follows. As was mentioned in Sec.2.1.1, the electron temperature in excimer laser discharges is low (a few eV) and only the electrons in the high-energy tail of the distribution function can directly ionize a ground state molecule or atom. Therefore, the major part of the electron production proceeds via two-step ionisation (see Eq. Eq. 2.1, 2.2) involving electronically excited states (denoted as $Rg^*$ with a spatial density $m^*$). The loss of electrons is governed by attachment to $F_2$.

The balance of the electron density $n_e$ and the excited particle density $m^*$ can be described by two coupled kinetic equations [22,23,84] as follows:

$$\frac{dn_e}{dt} = {k_i}^*\, m^*\, n_e - \nu_a\, n_e \tag{2.16}$$

$$\frac{dm^*}{dt} = \nu^*\, n_e - \nu_{qe}\, n_e - \nu_{qm}\, m^* \tag{2.17}$$

where $k_i^*\, m^*$ represents the ionisation frequency $\nu_i^*$ of the excited states, $k_i^*$ is the rate constant for the ionisation of excited states, $\nu_a$ is the attachment frequency of electrons to $F_2$ as determined by $k_a\,[F_2]$, $\nu^*$ is the excitation frequency of the rare gas atom Rg and $\nu_{qe}$ and $\nu_{qm}$ are the quenching frequencies of excited states by electrons and heavy particles, as shown in Eq. 2.2 and 2.5.

In e-beam sustained discharges, as direct consequence of the mechanism for production of excimer molecules, the electronically excited state populations $m^*$ are driven out of equilibrium by the competition between electron and heavy particle collisional

process. From Eq. 2.17, it is clear that the heavy particle quenching process tends to reduce the excited state populations, whereas the collisions with electrons increase them. Consequently, the electron density increases and therefore the excited state density also increases. Since the total ionisation rate constant is proportional to the excited state population, the total ionisation rate constant increases as the electron density increases, which further increases the electron density and eventually turns the discharge in to an arc.

An initial study of this two-step ionisation instability was performed by Daugherty et. al [23] on an e-beam-sustained KrF laser. Based on Eq. 2.16 and 2.17, Daugherty et. al [22, 23] derived a stability criterion for these lasers:

$$\nu_a > 2\,\nu_i^* \tag{2.18}$$

Eq. 2.18 states that when the attachment frequency exceeds twice the ionisation frequency of excited states by the e-beam, the discharge will be stable. On the other hand, for low halogen densities the attachment frequency will be smaller than twice the ionisation frequency and consequently the discharge will become unstable. By increasing the density of the halogen donor, the attachment increases thereby stabilizing the e-beam sustained discharge. This implies that with increasing concentration of the halogen donor, the attachment exceeds the stepwise ionisation and the stability of the discharge increases, i.e., high halogen concentration and large attachment rate constant are beneficial to discharge stabilisation in e-beam sustained discharges.

However, experimental evidences [21,25,78,81,85] obtained in self-sustained XeCl laser discharges show that the onset of filamentation is temporally advanced by increasing HCl concentration. Obviously Eq. 2.18 can not satisfactorily explain the adverse effect of an increasing halogen donor density on discharge instability. To directly account for the prominent role of halogen donors, Hogan et. al proposed the local halogen depletion model of instability [21, 25, 85], which will be discussed in the next Section.

Later, Borisov [84] put forward a modification on the stepwise ionisation instability theory in order to make it applicable for the case of self-sustained discharges. According to his theory and experiments, the discharges in self-sustained $F_2$ laser gas mixture are highly stable even at elevated (2 %) $F_2$ concentration. Napartovich [24, 88] has supported this prediction within a numerical model for such $F_2$ laser gas mixtures, concluding that initial small electron density or electric field perturbations would not grow up into filaments in these discharges. Further, Borisov concluded from his experiments and theoretical modeling that the instabilities in a KrF laser are associated with the presence of heavy rare gas (Kr in KrF laser), only in whose presence the

addition of more $F_2$ accelerates the growth of instabilities. We note that these are the only studies available in $F_2$-based excimer laser gas mixtures which deal with the discharge instabilities. In order to provide more reliable information in this field, detailed experimental results are presented in Chapter 5 which question the validity of this thoery and observations.

### 2.3.2 Halogen depletion model

The spatial inhomogeneity and the time dependence of the density of the attaching gas, i.e., the density of the halogen donor such as HCl or $F_2$, plays an important role in this instability mechanism [21, 25, 78, 81, 85].

During the discharge, $F_2$ is mainly consumed through electron attachment leading to the formation of atomic F (see Eq. 2.4). The recombination of atomic Fluorine to $F_2$ proceeds on a slower time scale compared to the duration of the discharge (hundreds of $\mu$s). The concentration of $F_2$ is, therefore, progressively reduced throughout the duration of the discharge. This affects the electron kinetics within the discharge since the predominant electron loss mechanism is dissociative attachment (Eq. 2.4).

Following Eq. 2.10, the electron balance equation can be written as:

$$\frac{dn_e}{dt} = k_i\, n_e\, [\mathrm{Rg}] - \mathrm{k_a\ n_e\ [Halogen]} \tag{2.19}$$

where $k_i$ and $k_a$ are the effective rate coefficients for ionisation and attachment.

A local rise in the electron density will lead to a local depletion of the halogen density as a result of the higher electron attachment rate. This decrease in the local halogen density reduces the electron loss rate by attachment, resulting in an even further increase of the local electron density, thereby creating an undesired feedback loop. This feedback loop in the electron-Fluorine kinetics gives rise to a runaway of the local electron density, $\frac{dn_e}{dt} > 0$, which is considered to govern the transformation from a homogeneous glow into a discharge containing numerous filaments.

A theoretical analysis of the halogen depletion instability carried out by Coutts and Webb [85] for XeCl laser gas discharges indicates that the electron density $n_e(t)$ during the early stages of a uniform glow discharge grows according to,

$$n_e(t) \sim n_{e0}\,[1 + (1/2)\,{k_a}^2\, n_{e0}\,[HCl]_0\, t^2 + ....] \tag{2.20}$$

where $k_a$ is the electron dissociative attachment rate and where $n_{e0}$ and $[\mathrm{HCl}]_0$ are the concentrations of the electrons and HCl (halogen donor) at the start of the glow

phase of the discharge, respectively. Hence, the duration of the glow phase, $\tau'$, defined as the time it takes for a local discharge electron density perturbation to double with respect to its value at the start of the glow phase ($n_{e0}$), is given by,

$$1/\tau'^2 \sim \frac{1}{2} {k_a}^2 n_{e0} [HCl]_0 \tag{2.21}$$

For later times, the runaway of the discharge instabilities would even be more rapid than predicted by Eq. 2.21 due to the effect of the higher order terms in Eq. 2.20.

Experiments on a XeCl laser confirmed the predictions of the theoretical model of Coutts and Webb [85]. To answer the question of which instability mechanism plays a major role in $F_2$–based excimer laser gas mixtures, we carried out experimental investigations in $F_2$-based excimer laser gas mixtures as will be described in Chapter 5.

## 2.4 Other causes of discharge instabilities

Kushner developed a numerical kinetic model in which both macroscopic (mm's to cm's) and microscopic ($<$ 10's - 100's $\mu$m) instabilities are simulated [89]. He suggested that the termination of laser oscillation in KrF lasers prior to the end of the pump pulse is due to operating point instabilities (OPI) which are analogues to the halogen depletion instabilities. These instabilities are driven by a perturbation in the spatial uniformity of E/N that arise from the non-uniform distribution of preionisation electron density or halogen density in the gas mixture. These perturbations would then become the seed for the formation of micro-arcs or filaments which dominate over macroscopic discharge constrictions and can lead to arcing in the discharge volume.

The uniformity of power deposition during the pump pulse in an excimer laser discharge is largely determined by the uniformity of the electric field distribution provided by the electrode profiles. For example, the distortions in the electric field due to sharp-edged electrode boundaries can cause discharge filamentation [90]. Several authors have developed analytical expressions for the design of electrodes which cause minimum electric field distortions and thereby reducing the propensity towards arcing or generating discharge instabilities [91–93].

Several studies have been conducted in XeCl lasers to investigate the dependence of discharge homogeneity on the electrodes [94,95] and the processes that happen near to the electrode surface [96,97]. In particular, it has been shown [31,78,82,98–100] that

hot spots at the cathode surface are the main cause of discharge filamentation in high-pressure HCl-based laser gas mixtures. The hot spots are heated spots of electrode material with reduced work function, emitting more electrons than the otherwise cold cathode and appearing much brighter than the homogeneous glow discharge. These hot spots are formed due to a localized modulation of some property of the cathode surface (e.g. protrusions on the cathode surface or due to the dynamics of the formation of cathode sheath) and perturb the quasi-steady state of the discharge. The hot spot bridges the bulk of the discharge with a small filament. As time progresses these small filaments grow brighter, grow towards the anode under the influence of the applied electric field. Finally, it results in arcs between the electrodes. The rate of growth of this current filamentation is governed by local halogen depletion.

## 2.5 Summary

In contrast to the elaborate studies carried out on XeCl laser discharges [21,25,78,82, 85,96], the mechanism behind the onset and development of filaments in the discharges in $F_2$-based gas mixtures are not well studied [65, 89]. Furthermore, there are some discrepancies between the experimental observations and theoretical predictions for the development of discharge instabilities in $F_2$-based excimer laser gases [84]. To resolve these discrepancies and shed some more light on the instability mechanism, we have performed detailed experimental discharge studies with $F_2$-based excimer laser gas mixtures. The results are presented in the next chapters.

# Chapter 3

# Effect of the preionisation on the discharge homogeneity

In chapter 2, the issues such as streamer formation and instabilities, associated with the initiation and sustainment of high pressure discharges in $F_2$-based excimer laser gas mixtures were discussed. The first section of the present chapter is devoted to the description and characterisation of the compact discharge setup developed for the investigation of the onset and growth of discharge instabilities in $F_2$-based excimer laser gas mixtures under precisely controlled conditions. In the second section of this chapter, the effect of the preionisation electron density and the preionisation timing on the initiation of homogeneous high-pressure discharges in $F_2$ laser gas mixtures is investigated. From these experiments, the optimum starting conditions required for the initiation of a streamer-free, homogeneous glow discharge in such gas mixtures are determined.

## 3.1 Experimental setup

A schematic layout of the experimental setup is shown in Fig. 3.1. To provide accurately controlled conditions for monitoring the onset and growth of instabilities, a small-volume discharge cell is used. A special pulse-forming line (PFL) generates fast-rising near square-shaped pump current pulses of about 220 ns duration. The gas is preionised by a short pulse, high intensity x-ray source. The spatial and temporal

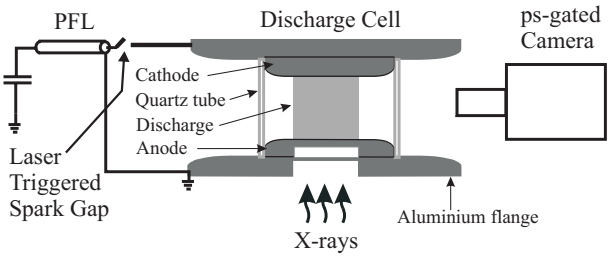


*Figure 3.1: Schematic layout of the experimental setup.*

development of the discharge is recorded via its fluorescence with a fast, intensified CCD camera (ICCD) which has a minimum gating time of 300 ps. The details of the experimental setup are described below.

### 3.1.1 Discharge cell

The cross section of the discharge cell is shown in Fig. 3.1. The discharge cell is formed by a quartz cylinder mounted between two Aluminium flanges. Onto these flanges the discharge electrodes are mounted. The quartz cylinder allows optical monitoring of the bulk of the discharge and of the phenomena occurring close to the electrodes such as the formation and development of a cathode sheath and hot spots. The design of the discharge cell was such that an easy exchange of the electrodes was possible, which is required for studies on different electrode materials and its surface roughness (see Chapter 4). The electrode gap can be varied from 5 to 20 mm by inserting Aluminium discs in between the electrode and the Aluminium flange. The electrodes have a diameter of 87 mm and possess a flat profile. In the central area between the electrodes, the electric field (E) distribution is nearly uniform with a calculated $\Delta E/E < 0.2$ % for all electrode gaps used. The x-rays, which provide the preionisation of the gas, are sent into the discharge volume through a 1 mm thick, 20 x 20 $mm^2$ window in the lower Aluminium flange and a similar window in the electrode (anode). The discharge cell can stand gas pressures of up to 6 bar which allows to investigate the high-pressure $F_2$ discharges typically found in corresponding excimer lasers. A gas purifier (Oxford Lasers), connected to the discharge chamber via the top electrode (cathode), filters out any impurities and helps to mix the gases.

### 3.1.2 Preionisation source

As mentioned in Chapter 2 (Sec. 2.2), the operation of high-pressure gas discharges in the self-sustained regime demands sufficient preionisation to obtain a uniform glow discharge. In principle, any source of ionising radiation can be used as a preionisation source. The most common methods are preionisation by direct electron beam interaction [101, 102], by UV photons (generated by sparks [103–105], corona [106], rare gas halide laser [107]) or by x-ray [108–111] irradiation of the laser gas mixture. Experiments are reported also with radioactive materials such as $\alpha$-particles [112] and neutrons [113].

Each of these methods has its own advantages and disadvantages. With direct electron beam ionisation, the strength of the foil window separating the vacuum diode of the e-beam generator from the high pressure discharge chamber limits its use. Since the window must be transparent for the electrons, a thin foil should be used. The strength requirements in combination with the heat transfer properties for this thin foil are not compatible with high transmission. The main drawback of UV photo-preionisation is the short penetration depth of this radiation in high pressure discharge gas mixtures, as well as the non-uniform distribution of preionised electrons due to the localised sources like spark plugs. A non-uniform distribution of the preionisation electrons will inhibit the streamer-free initiation of a homogeneous glow discharge. Moreover, in general, these preionisation sources are to be incorporated inside the discharge chamber which can cause a contamination of the discharge gas. Among the preionisation methods used, x-ray irradiation is most favorable for preionising large-volume high-pressure gas mixtures. The advantages of the x-ray preionisation are as follows:

- The penetration depth of x-rays is much larger than that of an electron beam or UV radiation. Therefore, large-volume, high-pressure gas mixtures can be preionised homogeneously.

- The x-ray source can be placed outside the discharge chamber such that it does not contaminate the gas mixture.

- The x-rays can be collimated easily by windows, which makes it possible to predefine the preionisation area and thereby the discharge area. Electrodes with complex profiles are therefore not needed, instead flat electrodes can be used which help to achieve a uniform electric field distribution [90–92, 114].

For the named reasons we chose x-ray irradiation for the preionisation of $F_2$-doped excimer laser gas mixtures. For this, we developed a compact short-pulse high-intensity x-ray source based on a corona plasma cathode [115, 116]. The construction and the operational principles of the x-ray source along with its characterisation are discussed below.

### The x-ray preionisation source

The x-ray source comprises a high voltage cathode from which electrons are accelerated towards a target constructed from a high-Z material, viz. the anode. In the target, the fast electrons are decelerated, producing x-rays. The emitted x-ray spectrum consists of characteristic frequencies of the target material superimposed on a Bremsstrahlung continuum.

Figure 3.2 shows the cross section of the x-ray source that we developed. The production and acceleration of electrons occurs in a cylindrical stainless steel chamber (diameter of 153 mm and height of 145 mm), which is pumped to high vacuum ($> 10^{-6}$ mbar) using a turbo-molecular pump. A six-stage mini-Marx generator, triggered by a thyratron unit, supplies a fast-rising negative high-voltage pulse of up to 180 kV to a corona plasma cathode which is placed on a metal holder that rests on an insulator support. The high voltage from the mini-Marx generator is connected via a coaxial cable and a HV-vacuum ceramic feed-through to the x-ray source.

Figure 3.3 shows the corona plasma cathode that comprises a Pyrex glass tube with a length of 80 mm and an outer diameter of 10 mm. The inner diameter of the tube amounts to 8.5 mm. A 50 $\mu m$ thick Brass foil is wrapped tightly around the tube. The foil is ended with 3 mm thick corona rings to avoid any undesired electric field enhancement on the edges of the foil. A thin tungsten wire is wound around the tube and the Brass foil. A window of about 20 x 10 $mm^2$ is cut into the Brass foil so that the wire is in contact with the surface of the Pyrex tube. A Copper rod inside the glass tubes acts as a trigger electrode for the initiation of the corona plasma. The rod is pushed against the top of the glass tube by placing a thin strip of Mylar underneath it. The trigger electrode is connected to earth via a capacitance ($C_e$ in Fig. 3.4). This capacitor, placed in series with the parasitic capacitance ($C_{tube}$ in Fig. 3.4) between the trigger electrode and the metal foil, is installed as a voltage divider to reduce the electrical stress on the glass.

During the rise of the voltage, electrons are liberated from the thin wires by field emission. The electrons are accelerated towards the inner rod electrode and collide with the surface of the Pyrex tube. This results in a plasma on the surface of the tube.

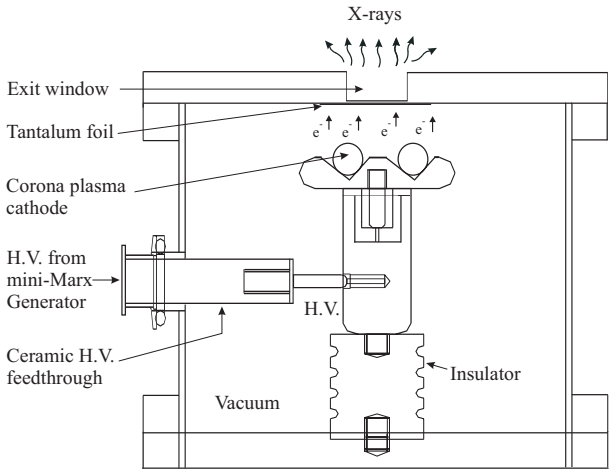


*Figure 3.2: Schematic lay out of the* x*-ray source.*

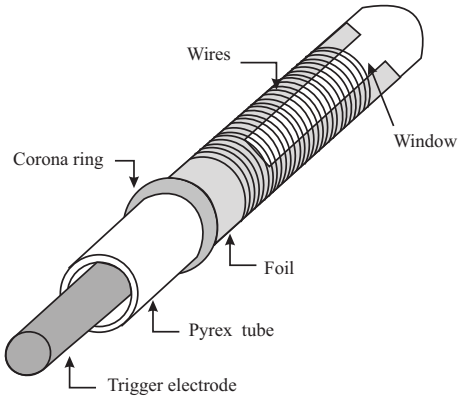


*Figure 3.3: An overview of the corona-plasma cathode.*

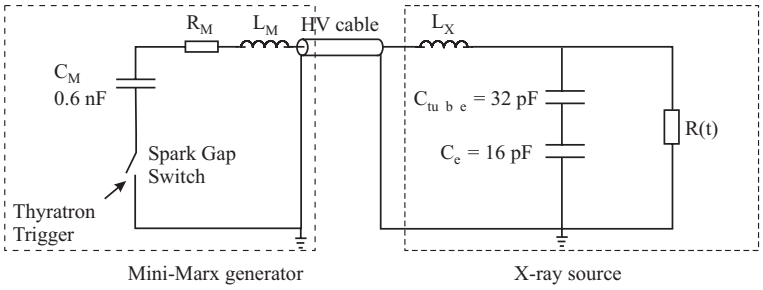


*Figure 3.4: Electrical scheme of the mini-Marx generator and the* x*-ray source*

The power dissipation in the plasma during the rise of the trigger voltage scales with the displacement current, which depends on the voltage rise time and the capacitance formed by the trigger electrode, the dielectric and the expanding plasma. Electrons are extracted from the surface plasma and accelerated towards the anode as depicted in Fig. 3.2. The anode is a 10 $\mu$m, thick Tantalum foil attached to the Aluminium vacuum lid of the x-ray source, which is on earth potential. The electrons produce x-rays while they are decelerated in the Tantalum foil. The x-rays leave the source through a 1 mm thick, 20 x 20 mm$^2$ window in the Aluminium vacuum lid.

Figure 3.4 shows the equivalent electrical scheme of the x-ray source and the driving circuit. $C_M$ is the storage capacitance in the mini-Marx generator and $L_M$ is its self inductance. $L_X$ is the self inductance of the x-ray chamber and R represents the time and voltage dependent resistance of the x-ray vacuum diode (the system of cathode and anode). The impedance of the system R(t) is time dependent because the corona plasma expands from the cathode towards the anode and thereby reduces the electrode gap d, while the effective emission area $A_d$ increases. The current in the vacuum diode $I_d(t)$, is space charge limited according to the Child-Langmuir law [117, 118].

$$I_d(t) \;=\; \frac{4}{9}\,\epsilon_0\,\sqrt{\frac{2e}{m}}\,\frac{V^{3/2}}{d^2}\,A_d \tag{3.1}$$

where V is the accelerating voltage, d is the time dependent anode-cathode gap spacing, $A_d$ is the time dependent area of the emitting surface, $\epsilon_0$ is the permittivity of free space and e and m are the charge and the mass of an electron, respectively. The

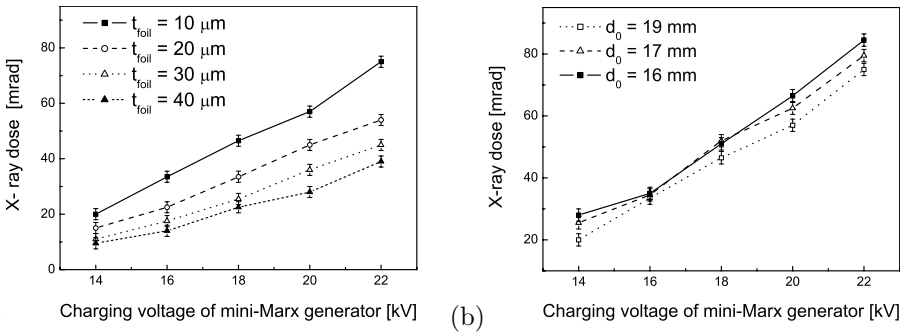


*Figure 3.5: (a) X-ray dose, measured in atmospheric air directly behind the exit window versus charging voltage for various thicknesses of the Tantalum foil ($t_{foil}$). The anode-cathode distance (distance between the corona plasma cathode and the Tantalum foil), $d_0$ was kept constant at 19 mm. (b) Dose versus charging voltage for different anode-cathode distance, $d_0$ in the* x-ray *diode. For all of the experiments described below, a thickness of 10 $\mu$m was used.*

total inductance in the circuit (sum of $L_M$, the self inductance of the cables and connectors, and $L_X$) is derived to be about 1 $\mu$H from the measured current oscillation frequency when the diode is short circuited.

### Characterisation of the source

To optimise its performance, i.e. to generate a high preionisation electron density in the gas discharge cell, the x-ray source is characterised in the following experiments. In a first step we measured the overall x-ray dose, while measurements with temporal and spatial distribution of x-rays are given further below.

The x-ray dose, which is proportional to the preionisation electron density [119], is monitored by means of pendosimeters (Physiotechnie SEQ6) for various charging voltage of the mini-Marx generator. For these measurements, the pendosimeter was placed in atmospheric air just above the exit window (20 x 20 $mm^2$) of the x-ray source. The x-ray dose was measured for various thicknesses of the target material ($t_{foil}$) and anode cathode distances $d_0$. The anode cathode distance $d_0$ is the distance between the corona plasma cathode and the Tantalum foil.

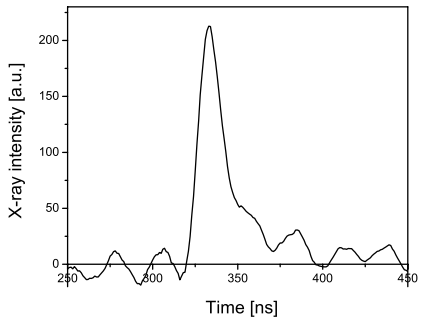


*Figure 3.6: Temporal evolution of* x*-ray signal at 24 kV charging voltage for mini-Marx generator.*

Figure 3.5(a) shows the measured dose versus the charging voltage of the mini-Marx generator for various thicknesses of the Tantalum foil. The anode-cathode distance was set at 19 mm. It can be seen that the dose increases with the charging voltage and with decreasing thickness of the target foil. Figure 3.5(b) shows the dose versus charging voltage for various anode-cathode distance while the thickness of Tantalum foil (10 $\mu$m) is kept constant. It can be seen that the dose increases slightly for shorter electrode gaps and that the dose, again, increases with the charging voltage of the mini-Marx generator. Since the measured dose is the highest when the thickness of the Tantalum foil is 10 $\mu$m at an anode-cathode distance of 16 mm, further experiments described in this thesis were done for this arrangement of the x-ray source.

The temporal shape of the x-ray pulse is obtained with a plastic scintillator (a 10 mm thick cylindrical block, type NE102A), placed about 2 mm away from the x-ray exit window. The fluorescence light from the scintillator is guided to a photo multiplier (Hamamatsu R763) with an optical fiber. Figure 3.6 (b) shows the measured temporal shape of the x-ray signal. It can be seen that the x-ray pulse has a fast rise time of about 17 ns and a short pulse duration (FWHM) of about 20 ns which is favorable for the initiation of a streamer-free glow discharge as described in Sec. 2.2.2 of Chapter 2.

### Preionised area and spatial distribution of x-rays

By defining the preionised area (the x-ray irradiated area) in the discharge chamber, a particular spatial shape and size can be given to the discharge. By doing this, the

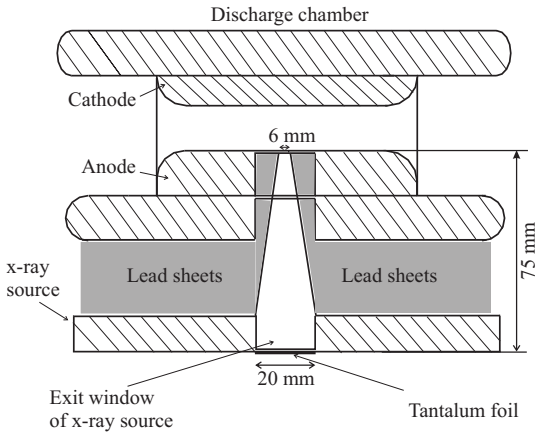


*Figure 3.7: The preionisation area and thereby the discharge area is defined by collimation of the* x*-rays. Lead sheets are used to define the solid angle for* x*-ray irradiation of discharge chamber.*

current density in the discharge also can be varied. We chose a rectangular shape for the discharge cross section since, then, an optimal contrast can be obtained between filaments which locally emit with an elevated intensity, and the bulk of the discharge which emits at a lower intensity but over a larger volume. The spatial distribution of x-rays in the discharge chamber is defined by placing Lead sheets with rectangular apertures in the path of x-rays.

Figure 3.7 shows a cross-sectional view of the setup including the Lead sheets (shaded gray) used for collimating the x-rays to a narrow beam for the preionisation of a well-defined volume in the discharge chamber. Several layers of Lead sheets (3 mm thick) were used with rectangular openings. At the exit window of x-ray source, the opening in the Lead is 20 x 20 $mm^2$ and the openings narrow down to an smaller area (e.g. 6 x 2 $mm^2$ or 8 x 2 $mm^2$) towards the discharge chamber, beneath the anode. We note, however, that the preionised area may be larger than the x-ray irradiated area due to the high energetic secondary electrons produced in the gas which depends also on the gas mixture used.

For investigating the apodizing of the x-ray distribution by the Lead sheets, the intensity distribution is recorded on a film (Kodak TMG/RA) at two locations. Figure 3.8 (a) shows an image of the intensity distribution of the x-rays when the film was

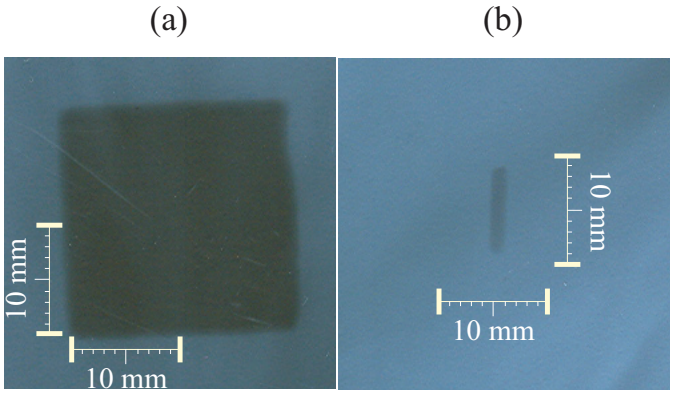


*Figure 3.8: Photographic images of* x-*ray distribution (a) on top of the exit window of* x-*ray source (window size is 20 × 20 mm$^2$), (b) on top of the discharge anode after collimation of the x-rays by Lead sheets (window size of 8 × 2 mm$^2$). The images were recorded on* x-*ray film.*

placed at the exit window of the x-ray source and irradiated with 50 exposures from x-ray pulses (charging voltage of 22 kV). It can be seen that the x-ray source produces a homogeneous intensity distribution over an area of about 22 x 22 mm$^2$. The next measurement of the intensity distribution of x-rays is done after collimating the x-rays with a Lead window of 2 x 8 mm $^2$. The distance between the Tantalum foil and the top of the discharge anode was about 120 mm. The charging voltage of the x-ray source was 22 kV. In order to obtain a visible x-ray image, the film placed on the top of the anode had to be exposed by 500 shots of the x-ray pulse. The image obtained is shown in Fig. 3.8 (b). It can be seen in Fig. 3.8 (b) that the spatial distribution of x-rays is restricted to a rectangular area with a dimension of about 2 x 8 mm$^2$. It can be observed that the film is less darkened although now ten times more exposures were used than the previous case. One reason for the reduction in the x-ray intensity could be that the x-rays are attenuated while it passes through two 1 mm thick Aluminium windows before reaching the discharge chamber. Another reason might be that the irradiation intensity of the x-ray source decreases with distance (depends roughly on $1/distance$, see Fig. 3.9).

As shown in Fig. 3.1, the discharge chamber was mounted on the top of the x-ray source. In order to find out what experimental arrangement (distance between

the source and the discharge cell, Lead windows) does provide a homogeneous x-ray illumination with a maximum intensity, the following experiments were done. The highest and homogeneous x-ray intensity is needed to ensure that the minimum preionisation electron density required for the initiation of a homogeneous discharge is obtained (see Sec. 2.2.2 in Chapter 2). The measurements on the preionisation electron density will be given in Sec. 3.2.2.

The variation of x-ray dose with distance from the x-ray source is measured for three collimation configurations. In all cases, the charging voltage of mini-Marx generator was 24 kV. First, the dose was measured for a configuration where the x-rays were collimated by a 20 x 20 $mm^2$ window cut into two 3 mm thick Lead sheets placed on the top lid of the x-ray source. The distance from the Tantalum foil of the x-ray source was varied by moving the pendosimeter away from the x-ray source. The measured variation of x-ray dose with distance to the Tantalum foil is shown in Fig. 3.9 (a). It can be seen in Fig. 3.9 (a) that the dose decays with distance and on closer inspection, the data follows roughly a 1/distance dependence.

In the second configuration, the support flange and the anode of the discharge chamber were placed directly on the top of the x-ray source. The pendosimeter is placed on the top of the discharge anode. The measurement of the dose versus distance was carried out by moving the flange, anode and pendosimeter as a whole away from the source. In this case, the x-rays pass through two 1 mm thick, $20 \times 20$ $mm^2$ Aluminium window in the flange and anode of the discharge chamber and the variation of measured dose with distance is shown in Fig. 3.9 (b). It can be seen in Fig. 3.9 (b) that the x-ray dose drops with distance in this case also. It can also be seen that at a distance of 55 mm, the x-ray dose dropped to half of the value in Fig. 3.9 (a). This drop in the x-ray intensity can be due to the attenuation of x-rays by the two 1 mm thick Aluminium windows on the support flange and the anode of the discharge chamber.

Fig. 3.9 (c) plots the x-ray dose measured at various distances with the same procedure as in Fig. 3.9 (b), but with a Lead window of smaller area inserted (about 2 x 8 $mm^2$) in the discharge anode instead of the larger area (20 x 20 $mm^2$). It can be seen that the x-ray dose is about 12 times less than that in Fig. 3.9 (b). The ratio of the sensitive area of the pendosimeter (1x2 $cm^2$) and the small lead window is approximately equal to the reduction factor of the dose and therefore it can be concluded that the reduction in the x-ray dose is due to reduction in the x-ray irradiated area.

Since the dose scales approximately in proportion with the area of the window, it can be concluded that the x-ray intensity is spatially homogeneous, independent of how close the source was placed. Further experiments are done with the discharge

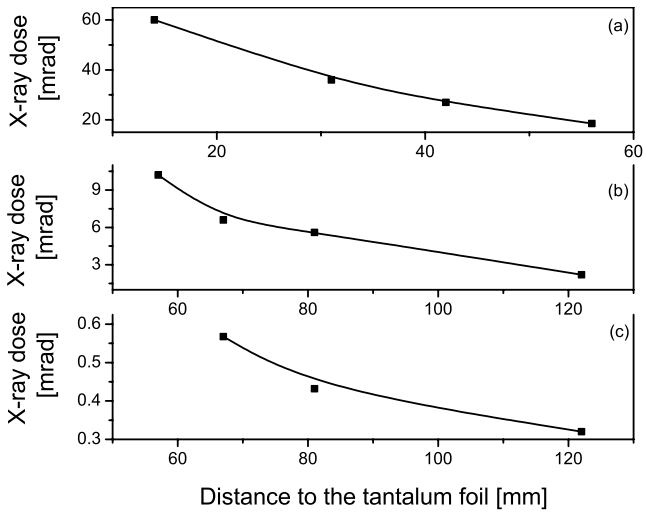


*Figure 3.9:* X-*ray dose versus distance with and without the flange and anode of the discharge chamber for a charging voltage of 24 kV at the mini-Marx generator. (a) shows the decrease of the dose with distance when the pendosimeter is placed directly on the top of the* x-*ray source (without flange and anode of the discharge chamber). The distance from the Tantalum foil of the* x-*ray source was varied by moving the pendosimeter away from the* x-*ray source, (b) shows the variation of the* x-*ray dose with distance when the pendosimeter is placed on the top of the discharge anode. The distance from the Tantalum foil was varied by moving together the pendosimeter, the flange and anode of the discharge chamber away from the source. In this case, the* x-*rays pass through two 1 mm thick, 20 × 20 mm*$^2$ *Aluminium windows in the flange and anode of the discharge chamber, (c) shows the variation of the* x-*ray dose with distance when the pendosimeter is placed on the top of the discharge anode, but with a Lead window of about 2 × 8 mm*$^2$ *inserted (see Fig. 3.7) in the anode. In this case again, the distance from the Tantalum foil was varied by moving the flange, anode and pendosimeter as a whole away from the* x-*ray source.*

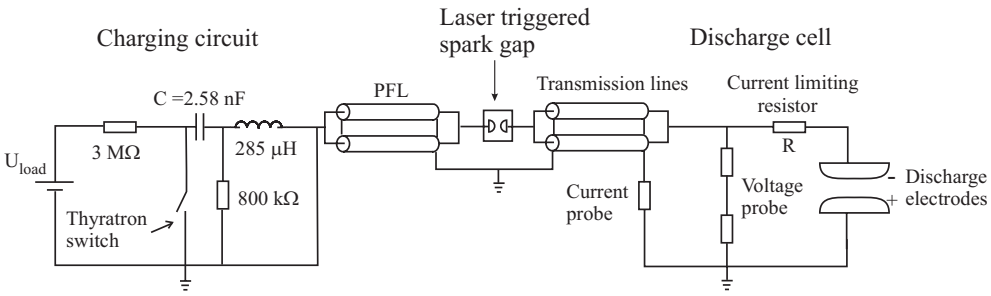


*Figure 3.10: Electrical scheme of discharge excitation circuit.*

chamber placed at a distance of 75 mm where a homogeneous distribution of x-rays is found with a high intensity. The distances shorter than 75 mm were not convenient for the discharge experiments due to the technical limitation of the design of the experimental setup.

### 3.1.3 Electrical excitation circuit for the discharge cell

Figure 3.10 shows the scheme of the electrical circuit used for the excitation of the discharge. The circuit uses a Pulse Forming Line (PFL) to produce a fast-rising high voltage pulse across the electrodes for the initiation of the gas discharge. To provide a square-shaped current pulse to sustain the discharge for a predetermined duration, two parallel coaxial cables (Heinzinger HVC30, 50 Ω, 20 m long) serve as the pulse forming line (PFL). The cables are pulse charged to a voltage $U_{load}$, by capacitor C via a thyratron switch (CX 1725) and discharged to the electrodes by a laser triggered spark gap via a transmission line. In our experiments, depending on the gas mixtures and pressures used, $U_{load}$ was varied from 15 to 35 kV. The transmission line is comprised of two parallel coaxial cables of the same type as of the PFL, but each with a length of 25 m which is longer than that of PFL. The current density can be varied by varying the current limiting resistor, R (0 -500 Ω), connected in series with the discharge.

The capacitance of C and the capacitance of PFL are made equal to prevent reflection losses during the charging and subsequent discharging of the PFL. This PFL produces voltage pulses with a short rise time of about 25 ns and it can sustain the gas discharge for a duration of 220 ns (FWHM). Small parts of the voltage pulses from the PFL

reflects at the discharge electrodes due to the mismatch of the impedance between the cable and the discharge cell. These voltage pulses again reflect at the inductance of the spark gap and reappear at the discharge which causes reverse current pulses. The longer cables of the transmission line delay the reverse current pulses for about 250 ns and thereby prevent the disruption of the discharge during the main current pulse.

As it was mentioned in Sec. 2.1.2, during the steady state phase of the discharge, the voltage $U_s$ across the electrodes is independent of the current $I_d$ flowing through the discharge [36]. The discharge current, $I_d$, can then be described with:

$$I_d\,(t) \;=\; (U_{load} \;-\; U_s\,(t)) \,/\, (Z \;+\; R) \tag{3.2}$$

where Z is the characteristic impedance of the pulse forming line. Since $U_{load}$ and Z are fixed, when $U_s$ increases or decreases with time (due to the inherent nature of the discharge), $I_d$ will automatically decrease or increase respectively.

### 3.1.4 Laser triggered spark gap

It is suggested [78] that the onset and development of filamentation in $F_2$-doped discharges will grow much faster than in Cl-based discharges. On the basis of gas kinetics, it is expected that the processes that play a role in filamentation take place on a time scale shorter than a few nanoseconds. Therefore, for a precise monitoring of the temporal development of the discharge (with the setup of Fig. 3.1), it is essential to keep the timing jitter between the start of the discharge and the gating of the ICCD camera below a few nanoseconds. The jitter in the gating of the ICCD camera is less than 20 ps and is negligible. However, when we measured the jitter in the switching of spark gaps, it amounts to more than several tens of nanoseconds when no special measures are taken. One of such measures is an electrical triggering of the spark gap, but this is not an option here, since the trigger voltage may start a pre-discharge in the discharge cell. Another measure to be considered is a triggering of the spark gap by a short pulse with an additional voltage (overvoltage). However also this leads to an unacceptably high jitter (> 100ns). An interesting alternative scheme offering low jitter in switching the spark gap employs a laser for triggering. Fig. 3.11 shows a schematic of the setup used in our experiments. The laser beam from a Q-switched Nd:YAG laser (Quantel, Type: YG 585-10) is focused to the surface of the anode of the spark gap through a small hole in the cathode using a lens of 20 mm focal length. The energy in the laser beam was in the order of 70 mJ and the pulse duration was about 25 ns.

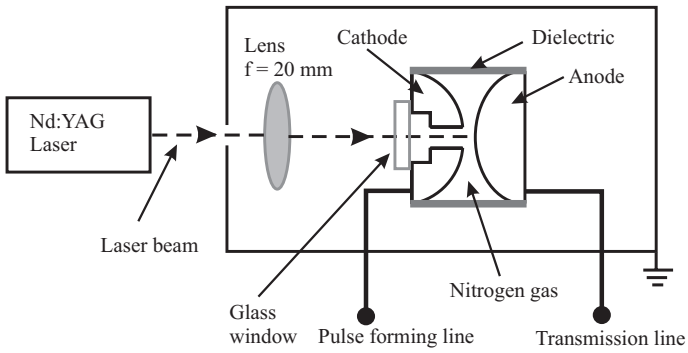


*Figure 3.11: Schematic of the laser triggered spark gap.*

For charging voltages in the range of 10 to 30 kV, the jitter in the switching of the spark gap is found to be small and amounts to only 1 ns. In this way the jitter in the onset of the discharge current with respect to the triggering of the ICCD camera is held below 1 ns and the spatio-temporal development of the discharge can be monitored in steps of 1 ns.

### 3.1.5 ICCD camera

To investigate the spatio-temporal development and instabilities of the discharge, specifically, the geometry and dynamics of filamentation, it is necessary to monitor the discharge evolution as a function of the time after its initiation and with a sufficiently high spatial and temporal resolution. The development of the discharge is recorded via its fluorescence with a fast, intensified CCD camera (ICCD, 4 Picos, Stanford Computer Optics) which has a minimum gating time of 300 ps. The line of observation of the ICCD camera is chosen parallel to the thinner dimension of the discharge volume. For our measurements, a 120 mm focal length (APO-Rodagon-D) lens was used for imaging the florescent plane onto the camera chip. In order to obtain a maximum spatial resolution for a field of view of about 30 x 20 $mm^2$, the lens and camera is used to demagnify the discharge image such that it was slightly smaller than the full area of the CCD chip in the camera. The resolution of the discharge images is tested using a standard resolution target (Newport, USAF-1951). The spatial resolution of the recorded images was measured to be about 125 micrometers.

### 3.1.6 Measurement of the discharge voltage and current

The discharge voltage is measured at the cathode of the discharge cell (see Fig. 3.10) with a Tektronix high voltage probe (P6015A), which has a rise time of 4 ns. The current is monitored in the return loop to the transmission line using a home made low-Ohmic probe. This probe is build in a coaxial geometry with ten low inductance resistors of 1 Ω electrically connected in parallel around a 50 Ω output resistor. The synchronization of the discharge voltage pulse with the x-ray preionisation is carried out by adjusting the delay between the x-ray scintillator signal and the laser trigger for the spark gap on a multi-channel delay generator (Stanford Research Systems, DG 535). This delay generator also provides the synchronization for the charging circuit of the PFL and the ICCD camera.

## 3.2 Effect of preionisation on the discharge uniformity

In order to produce a homogeneous discharge, the preionizing x-ray radiation has to be sufficiently strong and homogeneous (see Sec. 3.1.2) but it also has to be of proper timing with respect to the application of the discharge voltage. Otherwise the free electrons that are initially created by ionization attach too rapidly to the Fluorine in the laser gas mixture [78]. In order to come to quantitative statements about the effect of the preionisation on the discharge quality, we first measured the preionisation electron density created in various buffer gases (Helium or Neon). Such measurements when done with the various gases and mixtures would allow to identify physical mechanisms that enable a homogenization and stabilization of discharges by adding small amounts of certain noble gases (see Sec. 6.2.2). Next, we investigated the influence of the preionisation electron density and its timing on the discharge homogeneity in $F_2$ gas mixtures.

### 3.2.1 Preionisation electron density measurements

For these measurements, the discharge cell is employed as an ionisation chamber [115,116] as shown in Fig. 3.12(a). The DC voltage on the anode is chosen such that the applied electric field is high enough to collect all free charge, but stays below the threshold of avalanche multiplication of the electrons. Actually, the x-ray irradiation of the gas volume will produce two types of free charge, electrons and ions, which

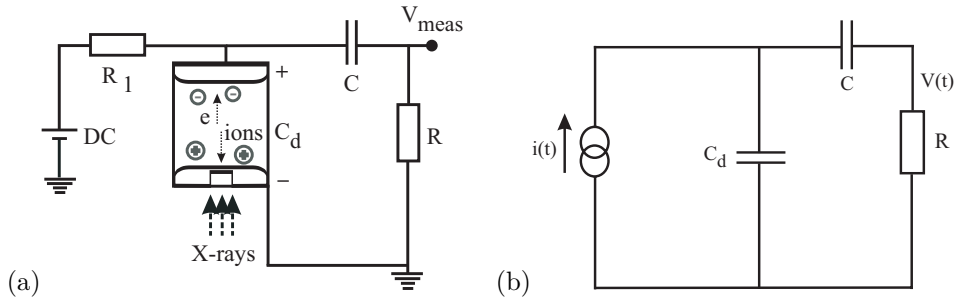


*Figure 3.12: (a) Schematic of the setup for the measurement of the preionisation electron density in gases, (b) Equivalent electric circuit.*

will be attracted towards the anode and cathode, respectively, under the influence of the applied electric field. As a result, a small electron and ion current starts to flow which discharges the inherent capacitance ($C_d$) of the discharge chamber, leading to a drop of the voltage across the electrodes. One way to determine the total number of electrons produced in the discharge volume is to measure the current through a measuring resistor R via the associated voltage drop. Integrating this current over time would yield the total charge produced in the gas volume [115]. An alternative way to measure the electron density is to form an $RC_d$ circuit which can integrate the current signal by itself and measure the change of voltage $\Delta V$ across $C_d$. This change of voltage is proportional to the produced charge $Q_0$ in the gas volume according to $Q_0 = C_d\ \Delta V$. To measure the total charge produced in a small x-ray preionised volume [about 1 cm (electrode gap in the discharge cell) x 2 cm (length of x-ray window) x 2 cm (breadth of x-ray window) = 4 $cm^3$ as in our case], the second method is advantageous since the measurement of $\Delta V$ is sufficient to obtain $Q_0$. A simple analysis of the electric circuit and required conditions for the measurement of the preionisation electron density with the respective methods are given below.

The measuring circuit for the preionisation electron density can be considered as a current source with an internal impedance that equals the inherent capacitance $C_d$ of the electrode configuration. The circuit is shown in Fig. 3.12(b) where $R_1$ is the charging resistor, C is the storage capacitance, R is the measuring resistor and V(t) is the voltage measured across this resistor. If q is the charge stored in $C_d$ and Q the charge stored in C, then the relation between the current i(t) and the voltage V(t)

across the measuring resistor can be written as,

$$i(t) \;=\; \frac{V(t)}{R}\,[1+\frac{C_d}{C}] + \;C_d\,\frac{dV}{dt} \tag{3.3}$$

If C $\gg C_d$, then:

$$i(t) \;=\; C_d[\frac{V(t)}{R\,C_d} \;+\frac{dV}{dt}] \tag{3.4}$$

Regarding Eq. 3.4, two cases can be considered that relate the time constant of the circuit to the time the electrons need to drift through the chamber. First, when $RC_d \ll d/v_d$ (fast circuit), and secondly, when $RC_d \gg d/v_d$ (slow circuit), where $RC_d$ is the RC time of the measuring part of the circuit and $d/v_d$ is the drift time of the electrons or ions across the electrode gap, and where $v_d$ is the drift velocity of electrons or ions.

With a fast circuit, $RC_d \ll d/v_d$, i.e.,

$$\frac{V(t)}{R\,C_d} \gg \frac{dV}{dt} \tag{3.5}$$

In this case, it follows from Eq. 3.4 and 3.5 that the current i(t) scales proportional to the voltage V measured across the resistor R according to:

$$i(t) \;\approx\; \frac{V(t)}{R} \tag{3.6}$$

The charge Q that is collected can then be calculated from:

$$Q_0 \;=\; \frac{1}{R}\int_0^{d/v_d} V(t)dt \tag{3.7}$$

This gives the total charge collected due to the drift of electrons and ions produced during the preionisation and thus it is twice the value of integral of the electron current. However, one should note that a measurement of the current in the fast circuit requires a measuring resistor with a low resistance (a few hundreds of ohms) which again reduces the measured voltage, V(t) in a small preionised volume (a few cubic centimeter). In that case, V(t) is strongly influenced by the electromagnetic noise produced during the triggering of mini-Marx generator of the x-ray source. The

experimental results of the measurement of the preionisation electron density using a fast circuit are shown in Sec. 3.2.1.

For a slow circuit, $RC_d \gg d/v_d$, with a large value of measuring resistor which is beneficial for the measurement of the charge produced in a small x-ray preionised volume (a few $cm^3$) in a noisy atmosphere,

$$\frac{dV}{dt} \gg \frac{V(t)}{R\,C_d} \tag{3.8}$$

In this case, it follows from Eq. 3.4 and 3.8 that the current i(t) scales proportional to the derivative of the voltage measured across resistor R according to:

$$i(t) \approx C_d \frac{dV}{dt} \tag{3.9}$$

i.e., for a slow circuit, to obtain any information about the current and thereby the charge produced, it is important to measure dV/dt. From Fig. 3.12(b), it can be seen that V(t) equals the difference in voltages across $C_d$ and C, ie., $V(t) = q/C_d - Q/C$. When C$\gg C_d$ which is easy to realize, V(t) shows how much the capacitance of the discharge chamber is discharged. The time constant $\tau$ with which $C_d$ is discharged is proportional to the drift time of free charges. If during the period $\tau$, charge $Q_0$ is collected, then the voltage drop $\Delta V$ across $C_d$ equals: $\Delta V = Q_0/C_d$.

i.e.,

$$Q_0 = C_d\,\Delta V \tag{3.10}$$

from which the charge density can be determined. In this procedure a large resistance (in the order of $10^6$ Ohms) can be used as a measuring resistor R which is advantageous in two ways: it gives a larger voltage drop from a small preionised volume compared to the fast circuit; and the signal to noise ratio is high compared to that of the fast circuit due to a higher voltage drop across R.

In summary, we have described two procedures to determine the preionisation electron density. We have shown that by choosing a specific value for $RC_d$, either the current due to the produced charges or directly the charge can be measured. For the measurement of the preionisation electron density in various gases both procedures have been used, as will be discussed below. The electron density after the irradiation of the x-rays is measured first in Helium (99.996 % purity) and Neon (99.999 % purity) as they are the commonly used buffer gases in $F_2$-based excimer laser discharges.

**Measurement of preionisation electron density using a fast circuit**

The preionisation electron density in the x-ray irradiated gas mixture is inferred from the current flowing through the current limiting resistor R with a short circuit-time constant (about 540 ns) compared to the carrier drift time $d/v_d$, i.e., $RC_d \ll d/v_d$. The measurement scheme used is shown in Fig. 3.13. A high-Ohmic resistor (40 MΩ) decouples the power supply from the rest of the circuit during the measurement. The distance between the electrodes is 1 cm and the x-rays reach the gas volume after penetrating two 1 mm thick aluminum windows. The preionised area is about 2.2 x 2.2 $cm^2$. Since the preionised volume is quite small (5.3 $cm^3$), the total amount of charge produced will be small. To obtain a detectable voltage signal across the measuring resistor, a value of R = 2.7 kΩ was chosen while the oscilloscope is terminated with 1 MΩ. The storage capacitor C separates the oscilloscope from the

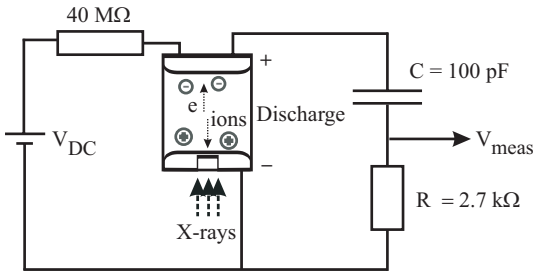


*Figure 3.13: Electrical scheme used for measuring the preionisation electron density under the condition that, $RC_d \ll d/v_d$. For this case, the integral of the current through the viewing resistor represents the total charge produced in the gas volume.*

DC voltage applied to the electrodes. In order to make sure that the charge of the collected preionised electrons does not significantly change the voltage, the storage capacitance C was chosen as high enough according to the following estimate. For an expected electron density of $10^8$ $cm^{-3}$ in a volume of about 5 $cm^3$, and a voltage difference of 10 V between $V_C$ and $V_{Cd}$, it is calculated that a capacitance of well above 8 pF is needed. We thus decided to use a capacitance of 100 pF in the setup. The parasitic capacitance $C_d$ of the discharge chamber was measured to be about 95 pF. The calculated $RC_d$-time of the measuring circuit is then about 540 ns, which is, indeed, much shorter than the drift time of electrons which is expected to be several microseconds [32, 120] for E/p < 1 kV $cm^{-1}$ $bar^{-1}$. In this way the conditions for Eq. 3.6 are fulfilled and the charge can be calculated from Eq. 3.7.

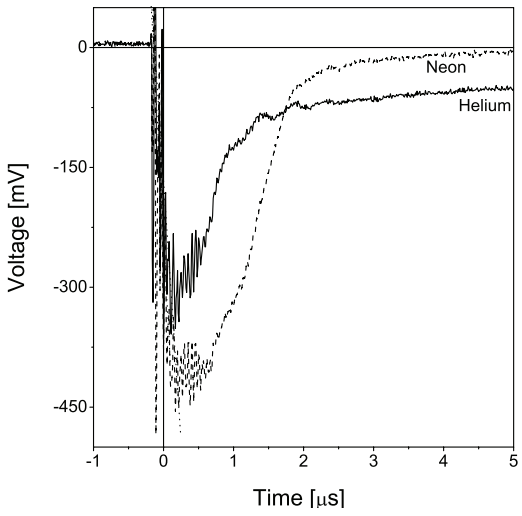


*Figure 3.14: Waveforms of the voltage across the measuring resistor R recorded with a short RC time constant (540 ns) compared to the carrier drift time $d/v_d$, i.e., $RC_d \ll d/v_d$.*

The dc charging voltage applied for Neon and Helium was 0.6 kV and 2.4 kV respectively, for a filling pressure of 5 bar. The voltage is kept below the threshold for avalanching but is high enough to collect all the produced charge. The charging voltage of the mini-Marx generator was 18 kV. The waveforms of the voltage measured across the current monitoring resistor R of the charge collecting circuit are shown in Fig. 3.14. The fast rising dip in the voltage signal corresponds to the electron current. Superimposed on the electron signal, is a longer pulse with a lower amplitude, generated by the current which is carried by the slow moving ions. Both voltage pulses have the same area, since the number of charge carriers produced must be equal. The electron density, $n_e$ is calculated from the area under the faster-decaying component in the measured signal [52, 115], according to:

$$n_e = \frac{1}{eAd\,R} \int_0^{d/v_d} V\,dt \tag{3.11}$$

where e is the electronic charge, A is the preionised area, d is the discharge gap,

R is the measuring resistor and $d/v_d$ is the time which an electron takes to drift through d with its velocity $v_d$. The preionisation electron densities determined from the recorded waveforms in Fig. 3.14 via Eq. 3.11, are shown in Table. 3.1. It can be seen that the charge density produced in different gases is quite different which is due to their different ionization cross sections for x-rays.

| Gas | Preionisation electron density $n_e$ [$10^7$ $cm^{-3}$ $bar^{-1}$ ] |
|---|---|
| Neon | 2.3 |
| Helium | 1.2 |

*Table 3.1: Measured preionisation electron densities for Helium and Neon. The charging voltage of the mini-Marx generator was 18 kV.*

**Measurement of preionisation electron density using a slow circuit**

In a second approach, using a circuit with long time constant (about 1 ms), as compared to the carrier drift times ($RC_d \gg d/v_d$), according to Eq. 3.10, the preionisation electron density can be determined from the voltage change ($\Delta V$) across the discharge cell caused by the x-ray irradiation.

The electric circuit used is shown in Fig. 3.15. The high-Ohmic 40 $M\Omega$ resistor decouples the voltage supply from the rest of the circuit during the collection of electrons. The voltage is measured across the 1 $M\Omega$ input impedance of an oscilloscope using a high voltage probe (Hameg HZ 36). The inherent capacitance $C_d$ of the discharge chamber is measured and amounts to about 90 pF. A capacitance of 1 nF is used for C, to decouple the power supply from the oscilloscope. This capacitance is chosen large enough so that the voltage drop across C would not affect the measured voltage signal ($V_{measured} \approx V_C - V_{C_d}$). The function of the 100 $k\Omega$ resistor and the diode is to protect the oscilloscope in case that the applied voltage would ignite an avalanche discharge.

The electron number density is measured for 5 bar Helium, and Neon with the electrode distance set to 1.5 cm. The cross-section of the preionised area is 1.3 x 0.7 $cm^2$. A dc voltage of 1.6 kV for He and 0.4 kV for Ne is applied at the discharge electrodes through the current limiting resistor (40 $M\Omega$). The x-ray irradiation produces a small electron and ion current in the discharge cell, which discharges the parasitic capacitance $C_d$ of the discharge chamber. With the chosen circuit parameters, the $RC$ time

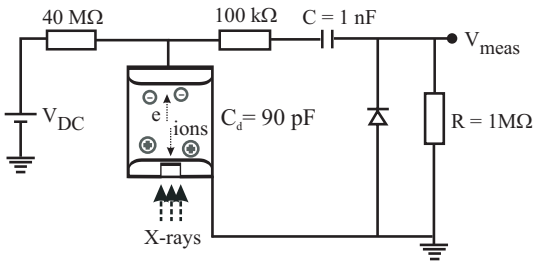


*Figure 3.15: Electrical scheme for measuring the preionisation electron density, with its parameters chosen such that the circuit time constant is long compared to the carrier drift time, i.e., $RC_d \gg d/v_d$.*

of the measuring circuit ($\sim$ 1 ms) is much larger than the drift time $d/v_d$ of the electrons ($\sim$ a few $\mu$s) across the electrode gap such that the condition $R\,C_d >> d/v_d$ is fulfilled. In this case, according to Eq. 3.10 the electronic charge generated by ionization, $Q_0 = C_d\,\Delta V$, should be given by the voltage change, $\Delta V$ measured across $R$.

Typical voltage signals measured across the 1 $M\Omega$ resistor of the oscilloscope for 5 bar He and Ne are shown in Fig. 3.16(a). The peak values $\Delta$V in the figure is the voltage change in Eq. 3.10, which is proportional to the total electronic charge produced in the gas volume (since the drift time of ions is in the order of ms, the contribution of ionic charge to the peak of the voltage is negligible, about 100 times smaller and longer than the electronic part). Figure 3.16(b) shows a graph of the preionisation electron density, as determined from the traces as in Fig. 3.16(a) via Eq. 3.10, versus the charging voltage of the mini-Marx generator. It can be seen that the electron density (in $\mathrm{cm}^{-3}\ \mathrm{bar}^{-1}$) in pure Helium and Neon is in the order of $10^7$, which is well consistent with the results obtained with the fast circuit. Since the second scheme has a high signal to noise ratio for the measurement of the charge generated in a small-volume x-ray preionised gas, we adopt the values obtained with the second scheme as a reference for the preionisation electron densities.

The described measurements with x-ray ionisation of Helium are an important reference because most excimer laser gas mixtures to be investigated from here on, consists mostly of Helium (as a buffer gas) with only a smaller amount of additional types of gas ($F_2$, Kr, Ar). For example, it can therefore be expected that the electron density generated in those excimer mixtures is basically the same as when pure Helium is

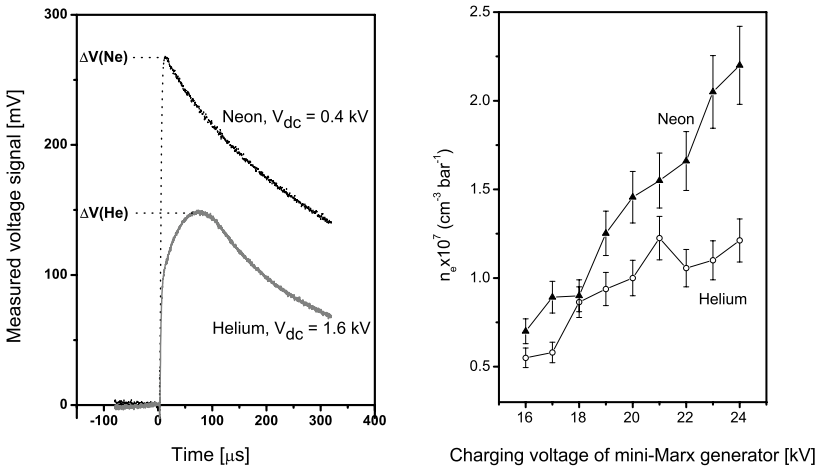


(a) (b)

*Figure 3.16: (a) The typical voltage signals measured for Helium and Neon from which the preionisation electron density is derived. The charging voltage of the mini Marx generator was 24 kV and the gas pressure used was 5 bar. (b) The preionisation electron density $n_e$ as a function of the charging voltage of the mini-Marx generator for Helium and Neon at a pressure of 5 bar.*

used, as here. It is known that excimer lasers require a sufficiently high preionisation (about $10^6$) for a homogeneous discharge [75]. Indeed, when inspecting the above given results one finds that these densities are generated. For instance, it can be seen that for a charging voltage of 24 kV, the preionisation electron density in pure Helium is 1.2x$10^7$ cm$^{-3}$ bar$^{-1}$, which is sufficiently high for a streamer-free and homogeneous initiation of a glow discharge.

In order to make our investigations directly relevant for $F_2$-based excimer lasers, we performed our experiments with the pressures and gas mixtures that are typically found in these lasers. All of the remaining investigations described in this chapter are conducted in gas mixtures of Helium and a small amount of Fluorine, which are typical for $F_2$ molecular gas lasers. The total pressure was set to 2 bar and held constant, while the relative $F_2$ concentrations were varied in the range of 0.0125 % - 0.15 %. For an estimation of the preionisation electron density in such He/$F_2$ mixtures, due

to the minute $F_2$ concentration, it is safe to assume that the preionisation density is approximately the same as in pure He, as experimentally determined above. On the other hand, the above named electron densities were measured at a different (higher) He pressure (5 bar) than used here in excimer lasers (2 bar), such that the electron density for 2 bar is not known directly. However, since the absorption of x-rays scales proportionally with pressure (see the preionisation density measurements in Sec. 6.2.2), the preionisation electron density for 2 bar mixtures can be scaled accordingly. For 24 kV charging voltage of the mini-Marx generator, the x-ray pulse produced an electron number density of $\approx$ 1.2 x $10^7$ $cm^{-3}$ $bar^{-1}$ in He. Therefore, in a 2 bar He/0.25 mbar $F_2$ mixture, the preionisation electron density can be estimated as $\approx$ 2.4 x $10^7$ $cm^{-3}$.

### 3.2.2 Minimum preionisation electron density for the start up of homogeneous discharge

To maintain a spatial homogeneity of the avalanche process during the formative phase of the discharge, a minimum preionisation electron density of $10^6$ $cm^{-3}$ is required, as was predicted by Levatter and Lin [75]. In order to check, whether or not the preionisation density generated by our x-ray source, is sufficient to initiate a homogeneous discharge, the start up of the discharge is monitored with an ICCD camera for several preionisation electron densities. The degree of preionisation is varied by attenuating the x-rays. For this, thin Copper sheets of different thickness (0.5 mm, 1 mm and 2 mm) are inserted between the x-ray source and discharge chamber, and the electron density is measured with the above described method. However, it turns out that the strong attenuation of the x-rays by the Copper sheets prevents a direct measurement of the preionisation electron density for the thicknesses of 1 mm and 2 mm. The reason for this is that the densities are rather low, such that the signal from the electron ionization current becomes smaller than the noise, which is due to switching of the mini-Marx generator. The preionisation density that is obtained for these sheet thicknesses is derived from a calibration measurement with a sheet of 0.5 mm. This measurement is carried out using the measuring scheme with the slow circuit constant, $R\,C_d >> d/v^-$. Fig. 3.17 shows the voltage signals obtained with and without attenuation by the 0.5 mm Copper sheet. It can be seen that the Copper sheet reduces the preionisation electron density from 1.2 x $10^7$ $cm^{-3}$ $bar^{-1}$ to 0.5 x $10^7$ $cm^{-3}$ $bar^{-1}$. Assuming that the preionisation electron density is directly proportional to the x-ray intensity, this implies that about 58 % of the x-rays are absorbed by the Copper sheet.

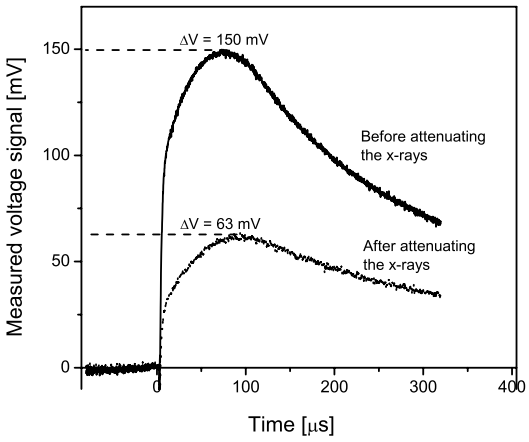


*Figure 3.17: Reduction of the preionisation electron density when a* x*-ray attenuating Copper sheet is inserted between the* x*-ray source and the discharge cell. Shown are the ionisation-induced voltage signals measured without and with a Copper sheet of 0.5 mm thickness. The measurements were done in 5 bar Helium with a DC collecting voltage of 1.6 kV.*

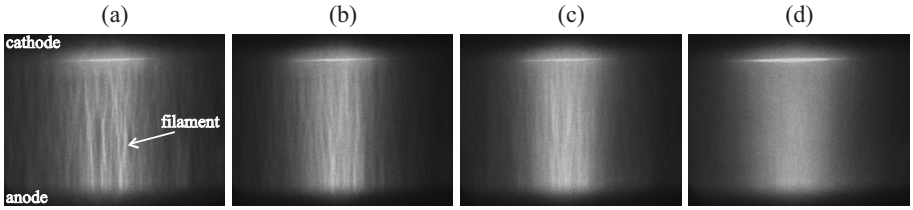


*Figure 3.18: Effect of increasing the preionisation electron density on the homogeneity of the discharge. These pictures are taken 25 ns after the initiation of the discharge in a gas mixture of 2 bar He/0.25 mbar* $F_2$*. The images show the quality of the discharge for a preionisation electron density of: (a)* $n_e \approx 0.7 \times 10^6\ cm^{-3}$ *(attenuation of the* x*-rays with a Copper sheet of 2 mm thickness), (b)* $n_e \approx 0.6 \times 10^7\ cm^{-3}$ *(attenuation of the* x*-rays with a Copper sheet of 1 mm thickness), (c)* $n_e \approx 10^7\ cm^{-3}$ *(attenuation of the* x*-rays with a Copper sheet of 0.5 mm thickness), (d) discharge initiated without any attenuation of the* x*-ray preionisation (*$n_e \approx 2.4 \times 10^7\ cm^{-3}$*). The gating time of the ICCD camera was 1 ns and the distance between the electrodes is 17 mm.*

In order to calculate the preionisation electron density obtained for the sheet thickness of 1 mm and 2 mm, the well-known mass attenuation equation for the absorption of x-rays is used:

$$I \;=\; I_0 \; exp\,[-(\mu/\rho)\,x] \tag{3.12}$$

In this expression, $I_0$ is the intensity of x-rays incident to the Copper sheets from the source, I is the emerging intensity transmitted through the Copper, $\mu/\rho$ is the mass attenuation coefficient for Copper and $x$ is the mass thickness. With the assumption that the K-alpha line [121] of Tantalum at $\approx$ 56 keV is the dominant in the x-ray spectrum, the attenuation for the 0.5 mm thick Copper sheet is calculated from Eq. 3.12 and is in the order of 50 %, which is close to the measured value. This justifies the above assumption that the preionisation is mainly produced by the K-alpha line and that the preionisation electron density scales proportional with the x-ray intensity. Accordingly, the preionisation electron density obtained for the sheet thickness of 1 and 2 mm can then be calculated from Eq. 3.12 as well. For a sheet thickness of 1 and 2 mm, we find a preionisation density of 0.6 x $10^7$ $cm^{-3}$ and 0.7 x $10^6$ $cm^{-3}$ respectively.

With these numbers on the electron densities for various degrees of x-ray attenuation, the improvement in the homogeneity of the discharge as recorded with the ICCD camera can be related to absolute electron number densities. The images are taken at 25 ns after the initiation of the discharge in gas mixtures of 2 bar He/0.25 mbar $F_2$. The gating time of the camera was set to 1 ns and kept constant for all measurements. The imaging of the fluorescence in the discharge was done as described in Sec. 3.1. Figure 3.18 (a) shows the fluorescence during the start up phase of the discharge, with a preionisation electron density $n_e$ of 0.7 x $10^6$ $cm^{-3}$. It can be clearly seen that the discharge is not initiated homogeneously as many streamers can be seen in the bulk of the discharge. However, when the preionisation electron density is increased to $n_e \approx$ 0.6 x $10^7$ $cm^{-3}$ and then to $n_e \approx$ 1 x $10^7$ $cm^{-3}$, the discharge homogeneity improves as shown in Fig. 3.18 (b) and 3.18 (c). Finally, with a preionisation electron density of about $n_e \approx$ 2.4 x $10^7$ $cm^{-3}$, the discharge is initiated without any streamers as shown in Fig. 3.18 (d). In the transition range towards the sufficiently high preionisation electron density, the discharge inhomogeneity disappears only gradually and for a quantitative analysis, some measure for the degree of inhomogeneity would be required. The development of such a measure for the degree of discharge inhomogeneity is presented in Sec. 4.2.1.

From these experiments, it can be concluded that a preionisation electron density of about 2.4 x $10^7$ $cm^{-3}$ is sufficient enough to initiate a streamer-free homogeneous

glow discharge. Further experiments described in this thesis are conducted with this preionisation electron density.

### 3.2.3 Effect of the preionisation delay time on the discharge homogeneity

In addition to the preionisation electron density, also the time delay, $\Delta t$, between the application of the preionisation pulse and the high voltage across the discharge electrodes (see Fig. 3.19) can be expected to be an important parameter that determines the homogeneity of a discharge. The minimum preionisation electron density that is sufficient for the generation of a homogeneous discharge was determined in Sec. 3.2.2. However, when this degree of preionisation is applied too early (compared to the application of the discharge voltage), this may allow a significant fraction of these electrons to attach to the Fluorine in the gas mixture before the electron avalanche begins to generate additional electrons. Similarly, when the preionisation is applied too late, this would not render enough electrons available for the avalanche multiplication process to lead to a spatially homogeneous excitation of the gas. From these arguments it is expected that there is an optimum time delay at which the nominally sufficient ionisation density initiates the start of a streamer-free glow discharge.

To determine this optimum time delay for preionisation, the following experiments were conducted. The start up and the development of the discharge voltage and discharge homogeneity are monitored at various delay times, for identical pumping conditions, in gas mixtures of 2 bar He and 1 mbar $F_2$. The delay time $\Delta t$ is varied from - 200 ns to + 55 ns while the pump current density ($\approx$ 40 A cm$^{-2}$ ) is kept constant. A negative delay corresponds to the application of the preionisation before the onset of the voltage pulse that is applied to the discharge electrodes.

Figure 3.20 shows the images of the discharges recorded with the ICCD camera at 25 ns after the discharge initiation, for various delay times. It can be seen that, as $\Delta t$ is increased from - 95 ns to - 50 ns, the homogeneity of the discharge improves considerably while for $\Delta t$ ranging from - 50 ns to + 55 ns, the discharge uniformity remains almost the same. The discharge homogeneity deteriorates for delay times larger than + 55 ns (not shown here).

The waveforms of the discharge voltage measured at the various delay times are shown in Fig. 3.21. These waveforms are corrected for $L\,di/dt$ from the inherent inductance of the set-up which was measured as 70 nH. From Fig. 3.21, it can be seen that the formative time, i.e., the time taken from the start up of the voltage to the onset of the

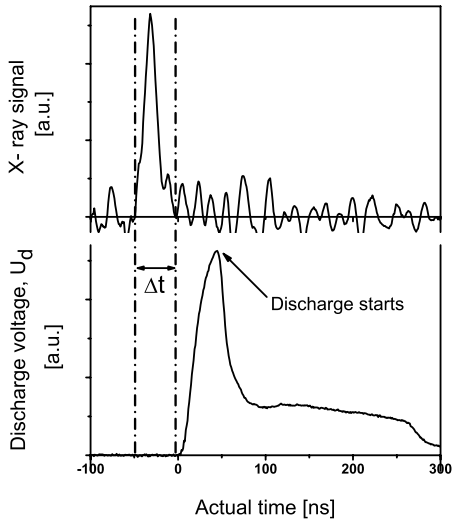


*Figure 3.19: The delay time $\Delta t$ is defined as the time between the application of the* x*-ray preionisation pulse and the high voltage across the discharge electrodes.*

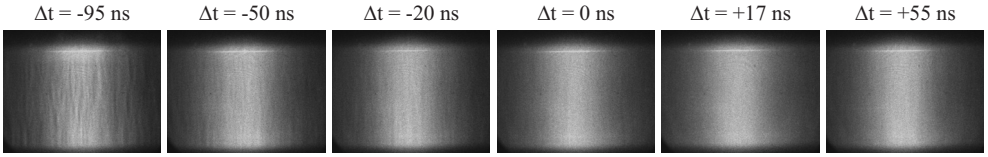


*Figure 3.20: Images of the discharges for various preionisation delay times ($\Delta t$). The pictures are taken at 25 ns after the initiation of the discharge. The gating time of the ICCD camera was 2 ns. The distance between the electrodes is 17 mm. The gas mixture used was 2 bar He/1 mbar $F_2$ and the current density ($\sim$ 40 A $cm^{-2}$) was kept constant in all measurements.*

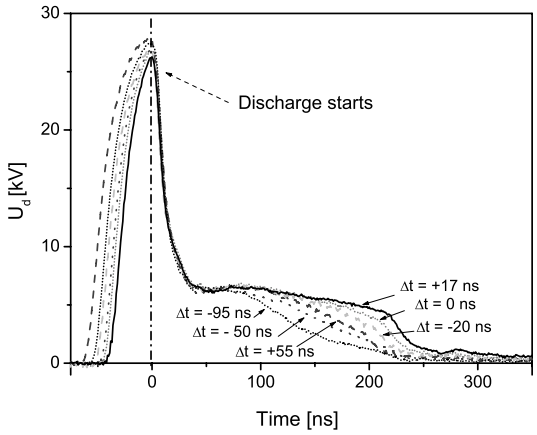


*Figure 3.21: The voltage waveforms with various preionisation delay times $\Delta t$. The gas mixture used was 2 bar He/1 mbar $F_2$ and the current density ($\sim$ 40 A $cm^{-2}$) was kept constant in all measurements.*

avalanche breakdown at which the voltage starts to drop to a steady-state voltage, differs for the various delay times. It is the shortest (44 ns) when $\Delta$t = +17 ns and the longest (66 ns) when $\Delta$t = -95 ns. Figure 3.21 also shows that the voltage needed for the breakdown of the gas varies with the delay time. It is the lowest (26 kV) when $\Delta$t = +17 ns and the highest (28 kV) when $\Delta$t = -95 ns. Another important feature to be noted in Fig. 3.21 is the variation in the rate of decrease of the steady-state voltage with various delay times. It can be seen that when $\Delta$t = + 17 ns, the steady-state voltage remains constant at $\approx$ 6.5 kV for about 100 ns and then slowly drops to zero in the next 120 ns. However, when the time delay is increased further to + 55 ns or decreased to less than - 95 ns, the steady-state voltage decreases much faster. In all cases, the steady-state current remains almost constant (within 10 % of the initial value) for the entire duration of the pump pulse. The onset of a fast drop in the steady-state voltage versus time probably indicates the onset of a low discharge impedance. A reason for the onset of a low discharge impedance would be the appearance of current filaments that arise due to the instabilities within the discharge volume. Therefore, the decrease rate of the steady-state voltage might be related to the appearance of current filaments in the discharge volume. The faster the rate of decrease of the steady state voltage, the earlier the filaments develop in

the discharge. Such correlation of the rate of decrease of the steady state voltage with the appearance of filaments is indeed found in the images of the discharge taken towards the end of the pump pulse (not shown here) and will be discussed in the coming chapters.

The observed dependence of the discharge homogeneity on the delay time can be explained by calculating the effective preionisation electron density, $n_e$, and life time, $\tau_a$, of electrons in a $F_2$-based gas mixture. The effective preionisation density is the number of preionisation electrons available for the avalanche multiplication at the start of the voltage pulse across the discharge electrodes and in a $F_2$-based gas mixture it is determined by the attachment of electrons to the Fluorine:

$$F_2 + e \rightarrow F^- + F \tag{3.13}$$

When no voltage is applied on the electrodes, the preionisation electron density, $n_e$ is reduced with time as:

$$\frac{dn_e}{d(\Delta t)} = -k_a \, n_e \, n_{F_2} \tag{3.14}$$

Here, $k_a$ denotes the electron attachment rate to Fluorine and $n_{F_2}$ is the initial Fluorine concentration in the gas mixture after the preionisation pulse. The effective preionisation electron density in $He/F_2$ gas mixtures at a time, $\Delta t$ can be written as

$$n_e\,(\Delta t) \;=\; n_e\,(0)\,exp^{\,-k_a\,n_{F_2}\,\Delta t} \tag{3.15}$$

where $n_e\,(0)$ is the initial preonisation electron density. With Eq. 3.15, the life time $\tau_a$, of electrons in an attaching gas, can be defined as:

$$\tau_a \;=\; 1/k_a\,n_{F_2} \tag{3.16}$$

The attachment rate constant $k_a$ is in the order of 2 x $10^{-9}$ $cm^3$ $s^{-1}$ [122]. In the gas mixtures with 0.05 % of $F_2$, the absolute Fluorine density $n_{F_2}$ is 2.5 x $10^{16}$ $cm^{-3}$. The lifetime of the electrons $\tau_a$ calculated from Eq. 3.16 is about 20 ns. From Eq. 3.15, it can be concluded that for time delays $\Delta t$ shorter than $\tau_a$, the preionisation electron density is close to $n_e\,(0)$ and the loss of electrons by attachment to Fluorine is small. If the preionisation delay time is larger than 20 ns, the preionisation electron density will be reduced considerably due to attachment to $F_2$ and may be insufficient to initiate a homogeneous discharge.

The observed variation in the formative time and the breakdown voltage with the delay time, as shown in Fig. 3.21, can be interpreted as follows. When $\Delta t$ is varied from - 95 ns towards positive values, an increasing part of the preionisation pulse will

overlap with the voltage rise on the discharge electrodes. As shown in Fig. 2.2, with increasing field, the attachment coefficient decreases while the ionisation coefficient increases [53]. This results in a slower depletion of the preionisation electrons. For shorter preionisation delay times, a higher number of electrons produced by preionisation will be available for the avalanche process which results in a shorter formative time and a lower voltage for the breakdown. On the contrary, when the preionisation delay time chosen is too long ($\Delta t \geq +$ 55 ns, see Fig. 3.20, 3.21) then only a small amount of preionisation electrons will be available in the gas volume when the applied voltage causes an electrical breakdown. In this case, as described in Sec. 2.2, the discharge avalanche process starts from the electrons that are already present in the gas mixture (by natural ionisation source or generated by field emission from protrusions on the cathode). The electron density provided by such effects is, however, much less than the required minimum preionisation electron density. Thus long delay times should result in a longer formative time and higher voltage for the breakdown of the gas as was found in the measurements shown in Fig. 3.21.

From the observations and discussions reported in the present section, it is concluded that the optimum preionisation delay time is $\approx +$ 17 ns, because this delay provides a homogeneous glow discharge, the shortest formative time and the lowest voltage for the breakdown as well as the lowest decay-rate of the steady-state voltage.

### 3.2.4 Effect of total pressure on the discharge uniformity

Increasing the total pressure leads to a stronger absorption of x-rays in the gas volume and a corresponding increase in the preionisation electron density [120, 123]. In order to check whether this increase in the preionisation electron density has an effect on the homogeneity of the discharges, we varied the total pressure of the gas mixture. Experiments were carried out in $He/F_2$ gas mixtures with a total pressure of 1 bar, 2 bar and 3 bar to which a partial pressure of 1 mbar $F_2$ was added. For all the measurements, the current density was kept constant at 50 A $cm^{-2}$. The gating time of the ICCD camera was set to 2 ns. Figure 3.22 shows images of the discharges at 40 ns, 90 ns, 130 ns and 170 ns after the initiation of the discharge.

It can be seen in Fig. 3.22(a) that the discharges in a mixture of 1 bar He/1 mbar $F_2$ remain homogeneous for 170 ns duration. However, the images show also that the discharges constrict with time. Figure 3.22(b) and Fig. 3.22(c) show that for a total pressure of 2 and 3 bar, the discharges remain homogeneous for about 120 ns and at later times, intense filaments appear in combination with discharge constriction. The transition from homogeneous to a filamentary discharge at 120 ns is not shown

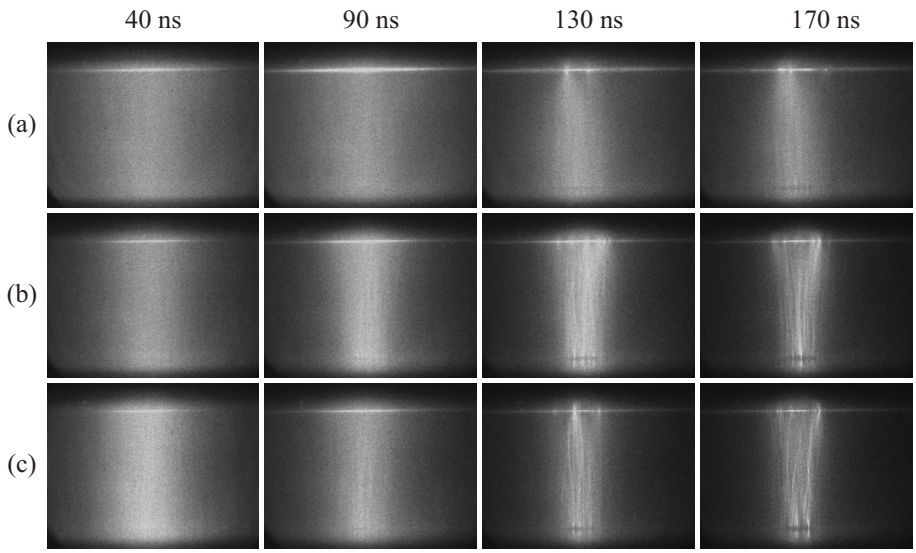


*Figure 3.22: Photographic images showing the effect of total pressure on the uniformity of discharges in gas mixtures of Helium and 1 mbar Fluorine. The images shown here are taken at 40 ns, 90 ns, 130 ns, and 170 ns after the initiation of the discharge at a total pressure of (a) 1 bar, (b) 2 bar, (c) 3 bar. The distance between the electrodes is 17 mm and the current density is about 50 A cm$^{-2}$. The gating time of the ICCD camera was 2 ns.*

in the figure, but it is inferred from the numerous images taken at every 5 ns of the discharge. Since it is not practical to display all the discharge images taken during this study and, moreover, as these images show only qualitatively the degradation of the discharge, we introduce a new measure in Chapter 4.2.1 to come to a more quantitative judgment of the discharge homogeneity.

Although the increased pressure causes a higher preionisation density, the discharge homogeneity deteriorates with pressure. One reason for the earlier appearance of discharge instabilities with pressure might be that the mechanisms, such as halogen depletion or stepwise ionisation which are responsible for the instabilities, evolve faster as the kinetic reactions proceed faster at higher pressures.

We were not able to go to higher pressures than 3 bar as the breakdown voltage was

exceeding the operating limit of the spark gap that switches the pulse forming line to the discharge. However, we found that the homogeneity of the discharge at 2 bar and 3 bar is not noticeably different. Based on this observation and due to technical reasons, we decided to carry out the further experiments at 2 bar total pressure.

## 3.3 Conclusions

In summary, we investigated the onset and development of filamentation in discharges in $F_2$-based excimer laser gas mixtures under well controlled conditions. For these investigations, we developed a compact experimental set-up which is well suited to initiate a homogeneous glow discharge in such gas mixtures and in which the discharge homogeneity can be monitored as a function of time. We found that a preionisation electron density of about 1 x $10^7$ $cm^{-3}$ $bar^{-1}$ is sufficient to initiate a streamer-free homogeneous glow discharge in $He/F_2$ gas mixtures. Our experiments show further that a homogeneous initiation of a glow discharge strongly depends on the time delay between the application of the preionisation pulse and the discharge voltage. The optimum time delay was found to be about 20 ns. Also in our experiments, it was found that the total pressure plays a role in the homogeneity of discharges. As the total pressure was increased, the discharges in gas mixtures of Helium and 1 mbar $F_2$ became more inhomogeneous. Although the inhomogeneity increased with increasing pressure, no significant change was observed in the discharge homogeneity when the pressure was varied from 2 bar to 3 bar.

# Chapter 4

# Influence of various electrode materials and their surface roughness on the discharge homogeneity

The electrodes in a discharge, especially the cathode, play an important role since it supplies the electrons for sustaining the current in the discharge. In Cl-based excimer discharges, it was shown that small protrusions on the cathode surface initiate hot spots and they develop in to discharge filaments which grow further into the discharge gap as time progresses [78, 82]. The choice of the electrode material and its surface roughness is therefore of prime importance in the development of a homogeneous discharge. In this chapter, our experiments are focused on finding the best candidate for electrode materials in $F_2$-based excimer discharges. For this purpose, we investigate the dependence of spatio-temporal development of discharge instabilities on the electrode materials and its surface roughness. The study includes Nickel, Chromium, and Gold coatings deposited via electroplating on Aluminium bulk electrodes, as well as electrodes made from Aluminium, Brass, Stainless Steel and Copper bulk material. The influence of the surface roughness was studied using polished as well as sand-blasted electrodes. Also, a new method is formulated to numerically analyse the discharge images so as to provide a quantitative measure for the discharge homogene-

ity in excimer laser gas mixtures. This method makes it possible for the first time to quantitatively distinguish between the homogeneous glow and any filaments that may be present in the discharge.

The study on the influence of the electrode materials and its surface roughness on the discharge uniformity requires repeated opening of the discharge chamber for an exchange of electrodes. Special care has been taken with regard to cleaning and passivating the discharge chamber with Fluorine to avoid any changes in the experimental conditions. For this purpose the procedures that are outlined below were strictly adhered to. After exchanging the electrodes, the discharge chamber is pumped down to approximately $2 \times 10^{-6}$ mbar and is purged with a flow of pure Helium. Then the cell is again evacuated to $2 \times 10^{-6}$ mbar and filled with a gas mixture of 2 bar He/1 mbar $F_2$. With this mixture about 200 discharges are ignited in the discharge chamber to clean the electrode surfaces. Thereafter, the discharge cell is filled with 3 bar He/3 mbar $F_2$ and left unused for approximately 10 hours for passivation. This procedure enabled to achieve a stable and reproducible steady state voltage in the measurements with the various electrodes.

The influence of various electrode materials and their surface roughness on the discharge stability was investigated in $F_2$-based excimer laser gas mixtures. In these studies, both electrodes, the cathode and the anode, were replaced each time. Nickel, Chromium and Gold electrodes were made by electrolytic coating of the respective metals on Aluminium electrodes. Copper, Brass and Steel electrodes are machined from solid blocks. Special care has been taken to minimise any imperfections on the surface profile of the electrodes by polishing first with a 4 grain and then with 6 grain which is the finest polishing paper available. In this way the surface roughness of each electrode material were kept the same to a great extent.

## 4.1 Measurement of the electrode surface roughness

The surface roughness of each electrode was measured using a profilometer (DekTak) which uses a diamond stylus tip to detect height variations in the surface when drawn across the electrode. The diameter of the stylus tip was 2.5 $\mu$m and the stylus force was 5 mg. The profilometer measures the vertical stylus displacement as a function of position over a specified length. The surface roughness is commonly specified as the average surface roughness Ra, which is defined as the integral of the absolute value of the vertical displacement Z of the stylus versus position x with regard to its average

displacement, measured over an evaluation length L:

$$Ra = \frac{1}{L} \int_0^L |Z(x)|\, dx \tag{4.1}$$

As an example of a roughness measurement, Fig. 4.1 shows the surface profile of a sandblasted Copper cathode over an evaluation length of 8 mm. The measured average surface roughness Ra amounts to $\sim 2\,\mu$m. The average surface roughness Ra was

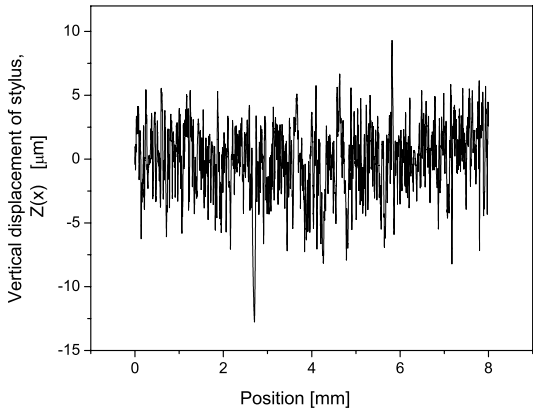


*Figure 4.1: Surface roughness profile of a sandblasted Copper cathode which shows the hills and valleys on the electrode surface as a function of position. The average surface roughness, Ra is* $\sim$ *2 $\mu$m. The evaluation length is 8 mm.*

measured for all electrodes used in this discharge study. For the Nickel, Chromium and Copper electrodes the roughness was approximately 0.2 $\mu$m and for Gold, Aluminium, Brass and Stainless Steel electrodes, it was 0.1 $\mu$m, 0.3 $\mu$m, 0.65 $\mu$m, and 0.7 $\mu$m respectively.

## 4.2 Influence of various electrode materials on the discharge homogeneity

The effect of various electrode materials is investigated in molecular $F_2$ as well as ArF laser gas mixtures. The respective gas mixtures were composed of 2 bar He/1 mbar $F_2$, and of 2 bar He/60 mbar Ar/1.5 mbar $F_2$. The distance between the electrodes was kept at 1.7 cm. The current density ($\sim$ 350 A cm$^{-2}$) and the power density ($\sim$ 1.2 MW cm$^{-3}$) were kept constant using current limiting resistors in series with the discharge. For all the measurements, the gating time of 2 ns was used for the ICCD camera. The intensity of the recorded images can, however, not be directly compared as the voltage applied to the micro channel plate of the ICCD camera is varied slightly to compensate for the variations in the light intensity of the discharges with the various electrodes. The spatial resolution of the images is about 125 $\mu$m.

### 4.2.1 Discharges in $F_2$ excimer laser gas mixtures

The typical time behaviour of the voltage, the current and the power deposition for discharges in a mixture of 2 bar He/1mbar $F_2$ is shown in Fig. 4.2 (a) together with the x-ray signal. It can be seen from Fig. 4.2 (a) that the x-ray pulse is applied about 17 ns after application of the discharge voltage. After the breakdown of the gas volume, indicated by the start of current flow, the voltage drops to a value of about $\sim$ 6.5 kV and the discharge current rises to a steady state value of about 600 A. The pump power density during steady state operation is about $\sim$ 1.2 MW cm$^{-3}$. The discharge cross section was about 1.4 $\times$ 1.3 cm$^2$ and the duration of the pump pulse was about 220 ns. In Fig. 4.2 (a), it can be seen that the steady state voltage decreases in time while the current increases slightly which means that the discharge impedance is decreasing. Figure 4.2 (b), compares the discharge voltages as a function of time for a Nickel-coated Aluminium electrode and a solid Copper bulk electrode, both measured in the same gas mixture of 2 bar He and 1 mbar $F_2$. It can be seen that the rate of decrease of the steady state voltage is higher for discharges with Copper electrodes than for discharges with Nickel electrodes. During the measurements with the different electrode materials, it is observed that the discharge voltage for Chromium and Gold-coated electrodes behave similarly to the voltage for the Nickel-coated electrodes. The discharge voltage for Aluminum, Brass and Stainless Steel electrodes, however, showed features similar to the voltage for the Copper electrodes.

Fig. 4.3 shows the images of the discharges in He/$F_2$ mixtures with various electrode

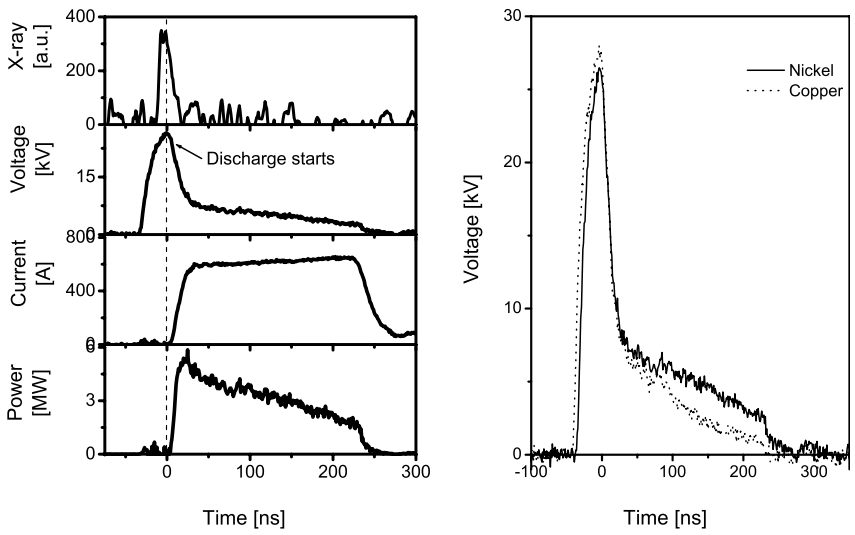


*Figure 4.2: (a) Temporal behavior of x-ray intensity, voltage, current and power deposition for a discharge with Nickel-coated Aluminium electrodes, (b) Temporal evolution of the voltage for discharges with Nickel-coated Aluminium electrodes as well as bulk Copper electrodes. The discharges were all generated in a gas mixture of 2 bar He/1 mbar $F_2$.*

materials. These images are taken in consecutive shots at 30 ns, 80 ns, 120 ns and 160 ns after the initiation of the discharge. The Ni, Cr and Au coated Aluminium electrodes and the bulk Cu and Al electrodes have a comparable average surface roughness (Ra) of about 0.1 to 0.3 $\mu$m, while the surface roughness for the Brass and steel electrodes is slightly higher and amounts to $\sim$ 0.7 $\mu$m. The discharges using electrode materials of Ni, Cr, Au, Cu and Al can be directly compared since they have similar surface roughness.

It can be observed in Fig. 4.3 (a) that in the discharges with Ni-coated electrodes, filaments become distinguishable from the homogeneous glow at 120 ns. At 160 ns, these filaments have become more intense and are clearly visible against the background of a weak glow discharge. The filamentation in discharges with Cr-coated

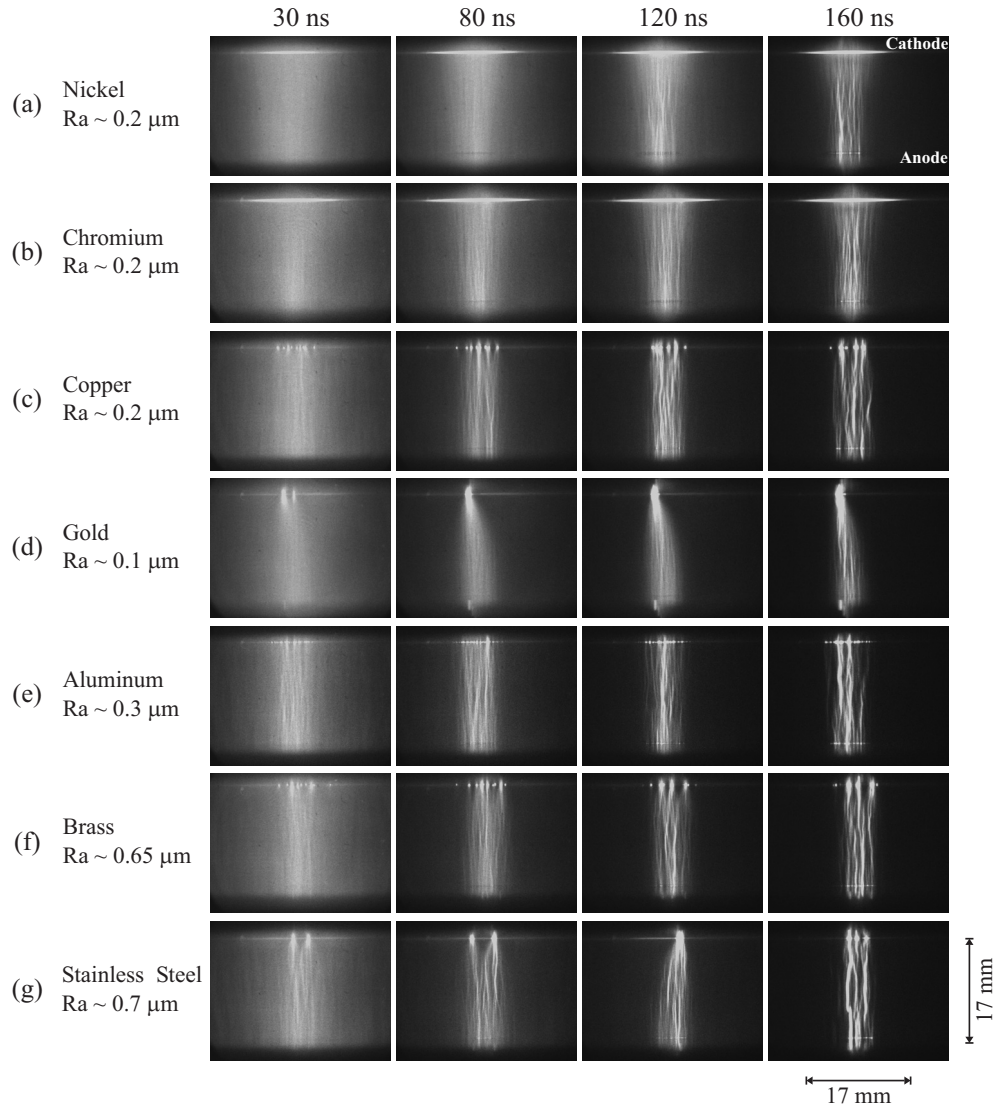


*Figure 4.3: Images of the temporal and spatial evolution of discharges generated with various electrode materials. The images displayed were taken in consecutive shots at 30 ns, 80 ns, 120 ns and 160 ns after the initiation of the discharge. The gating time of ICCD camera was 2 ns. The discharge cell is filled with a gas mixture of 2 bar He/1 mbar $F_2$. For all measurements, the current density was about $\sim$ 350 A $cm^{-2}$ and pump power density was about $\sim$ 1.2 MW $cm^{-3}$.*

electrodes proceeds similarly to the discharges with Ni-coated electrodes as shown in Fig. 4.3 (b), however, it becomes visible already at 80 ns. One distinctive feature for the discharges with Ni and Cr-coated electrodes is the presence of a well defined cathode sheath from the very beginning of the discharge.

Even though polished bulk Copper electrodes have the same surface roughness as Ni and Cr electrodes, it can be seen that discharges with these electrodes are not as homogeneous. Fig. 4.3 (c) shows that already in an early phase ($\leq$ 30 ns) hot spots are present at the cathode from which filaments extend into the bulk of the glow discharge. The number of hot spots and their position are not very reproducible. As time progresses, the hot spots become brighter and larger, while the discharge becomes more constricted. At 160 ns, the homogeneous glow has disappeared completely and only filaments are remaining. An interesting feature in the discharges with Copper electrodes is that filaments are originating from the cathode hot spots and later they connect the electrodes. This is entirely different from Ni and Cr-coated Aluminium electrodes where the filaments just appear in the bulk of the discharge.

Although discharges with Gold-coated electrodes appear as initiated homogeneously, a few cathode hot spots are already present in the early phase as shown in Fig. 4.3 (d). At 80 ns, only a single hot spot is visible which connects the discharge to the cathode. This hot spot must carry therefore the complete discharge current. It is also seen that by 80 ns the discharge is considerably constricted. Filamentation becomes visible at 120 ns and becomes more pronounced later on. We noted that the hot spot appeared always on the same position at the cathode indicating some protrusion on the surface. Since Gold is a soft metal, it might be that the thin layer of Gold ($\sim$ 2 $\mu$m) was removed under the high current density and power deposition during the discharge. This may result in a crater which enhances the field emission of electrons and formation of hot spots.

Discharges with bulk Aluminium, Brass and Stainless Steel electrodes, displayed in Fig. 4.3 (e), 4.3 (f), and 4.3 (g), respectively, show similar discharge features as with Copper electrodes. The discharges show some filamentation already at 80 ns and become increasingly inhomogeneous. At 160 ns the discharge is fully filamentary with Brass and Stainless Steel electrodes, the size of the hot spots are larger and the number of hot spots are less than in the discharges with Copper and Aluminium electrodes.

From Fig. 4.3, it can be concluded that the discharges with Ni and Cr-coated Aluminium electrodes are more homogeneous than the discharges with the other electrode materials.

So far, a central problem was to adequately characterize the spatio-temporal development of discharges although this is a basic requirement for a comparison with theoretical models. The reason is that, when discharge instabilities develop, these instabilities are highly specific for each single discharge event. Therefore individual images of discharges taken at consecutive shots, even when providing a high spatio-temporal resolution, are often not representative for the typical (average) development of instabilities. We present a novel method of characterising the spatio-temporal development of discharges, which is based on a numerical processing of spatio-temporally resolved images of the discharge fluorescence. It shows, in this chapter as well as in Chapters 5 and 6, that this approach enables for the first time to clearly identify and also quantify systematic dependencies of filamentation and changes in the size of the discharge as a function of the experimental parameters. The developed method is based on an image processing procedure similar to edge detection [124]. An overview on this method is given in Fig. 4.4.

In brief, the method can be described as follows. From the ICCD image, the intensity distribution of the discharge is determined, such as in Fig. 4.3, where filaments show up as as thinner lines or ranges of high fluorescence intensity whereas the bulk discharge shows only a slow variation of intensity with space. To separate the spatially rapid fluctuating intensity of any filaments from this slowly varying background we calculate the gradient profile of the recorded intensity distributions. As the measure of inhomogeneity we define the root-mean-square (RMS) deviation of the gradient profile along a straight line through the recorded image, a procedure similar to the quantification of surface roughness as described above in Eq. 4.1. More specifically, the degree of inhomogeneity of a discharge is the RMS or quadratic mean of the amplitudes of the peaks in the spatial gradient profile, dI(x)/dx, of the recorded intensity distribution I(x), along the x-direction (parallel to the plane of the electrodes):

$$\text{Degree of inhomogeneity} \;=\; \sqrt{\frac{1}{N}\sum_{i=1}^{N} {A_i}^2} \tag{4.2}$$

where $A_i$ is the amplitude of the $i^{th}$ peak and $N$ is the total number of peaks on $\partial I(x)/\partial x$.

Fig. 4.4 illustrates the procedure that is followed to determine the degree of inhomogeneity. Examples are given for a homogeneous discharge, a filamentary discharge and a discharge which is constricted into an arc in Fig. 4.4.1 to Fig. 4.4.3 respectively. In each discharge the center part (area within the dashed rectangle) is chosen for the image processing. Since the filaments are, to a good approximation vertical

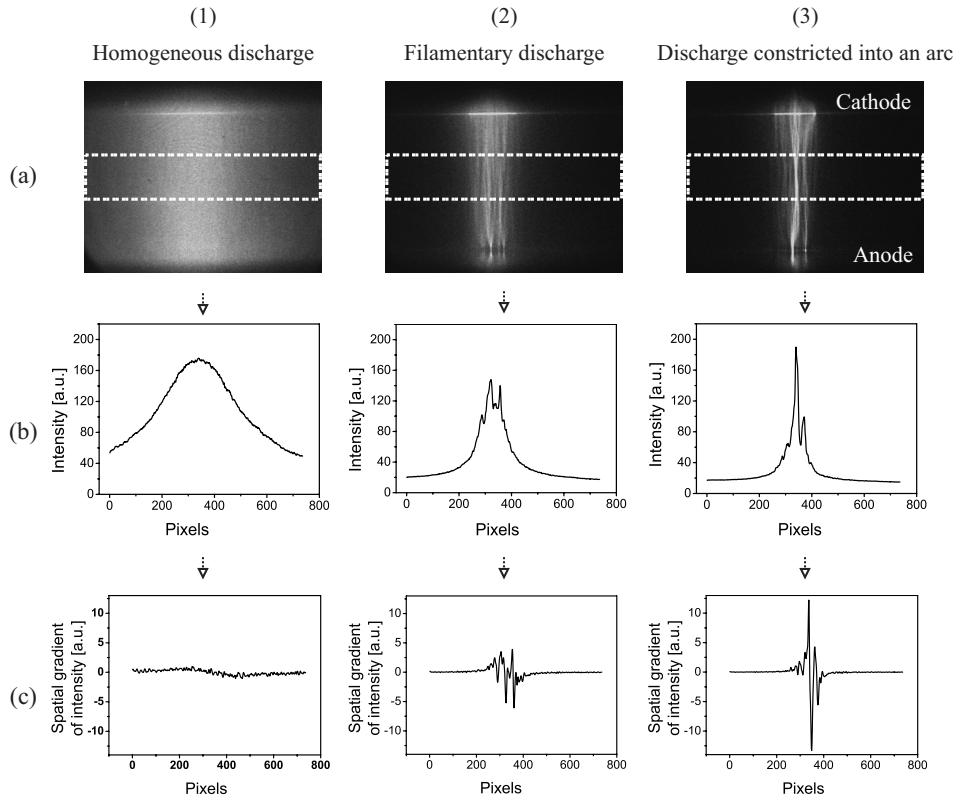


*Figure 4.4: Example showing the image processing sequence used for the calculation of the degree of discharge homogeneity. The selected part in the center of each discharge (area within the dashed rectangle) is used for image processing. The intensity values within the selected part of the discharge are averaged along the direction perpendicular to the plane of the electrodes. From the averaged intensity profile, the gradient profile and the degree of inhomogeneity are calculated. The graphs show the intensity and gradient profile plotted against the pixel number on the direction parallel to the plane of the electrodes. (1.a) Image of a homogeneous discharge, (1.b) its intensity profile and (1.c) the gradient of the intensity profile. (2.a) Image of a filamentary discharge, (2.b) its intensity profile and (2.c) the gradient of the intensity profile. (3.a) Image of a discharge that is constricted to an arc, (3.b) its intensity profile and (3.c) the gradient of the intensity profile. The quadratic mean obtained from (1.c), (2.c) and (3.c) using the Eq. 4.2 are 0.69, 2.49 and 5.14.*

in the selected rectangle in all images, the intensity values within the selected part are averaged along the direction perpendicular to the plane of the electrodes. This provides a better contrast of the filaments (if any) with respect to the diffuse part of the glow discharge and also excludes any influence from cathode sheath and hot spots which are usually much brighter than the homogeneous glow of the discharge.

The vertically averaged intensity profile of the center of the homogeneous discharge is shown in Fig. 4.4.1 (b). It can be seen that the intensity profile is a smooth profile which corresponds to the homogeneous glow of the discharge. The gradient of this intensity profile along the x-direction parallel to the plane of the electrodes is nearly zero as shown in Fig. 4.4.1 (c) indicating that there is no sharp transition in intensity in the x-direction of the selected part of the volume discharge. Figure 4.4.2 (b) shows the averaged intensity profile of the same selected part in the filamentary discharge. It consists of a smooth profile stemming from the diffuse glow discharge with several sharp peaks superimposed that correspond to the filaments in the discharge. The gradient of the intensity profile along the x-direction is shown in Fig. 4.4.2 (c). It represents only the peaks in the intensity profile that corresponds to filaments in the discharge while the constant background from the glow-part drops out. Figure 4.4.3 (b) and 4.4.3 (c) show the averaged intensity profile of the center part of the discharge which is constricted to an arc and its gradient along the direction parallel to the plane of the electrodes. It can be seen that the smooth part in the intensity profile has disappeared and the peaks are higher than in Fig. 4.4.2 (b). In the gradient profile of the intensity, the amplitude of the peaks has increased with respect to the gradient of the filamentary discharges shown in Fig. 4.4.2 (c) which indicates that the filament in this discharge is more intense than the one in the former. The quadratic mean or the RMS obtained from Fig. 4.4.1 (c), 4.4.2 (c) and 4.4.3 (c) using the Eq. 4.2 are 0.69, 2.49 and 5.14, respectively. These numbers provide a good measure for the discharge inhomogeneity since, due to their derivation, they represent the number as well as the brightness of filaments present in each discharge. The larger the quadratic mean, the larger the discharge inhomogeneity.

In a discharge, measuring the width as a function of time is of high importance, if one wants to physically relate a certain type of dynamics in the discharge (e.g. rate of growth of instabilities) with the measured current. Namely, without knowledge of the width, the measured current cannot be associated with a particular current density. However, the current density is a most central parameter that determines the dynamics. For example, if the width of the discharge during the development of the discharge is not recorded with the discharge current, temporal changes of the current density would get away unnoticed. Therefore, we define the decrease in width of the discharge (the full width half maximum of the discharge intensity profile) as a

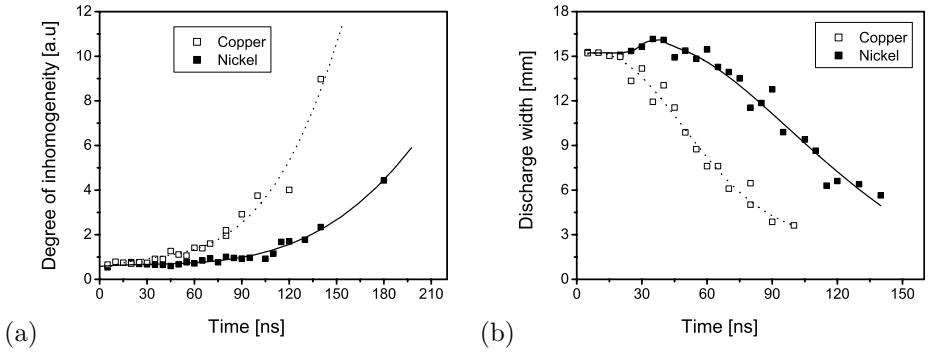


*Figure 4.5: (a) Temporal behavior of the degree of discharge inhomogeneity for discharges with Nickel and Copper electrodes in a gas mixture of 2 bar He/1 mbar $F_2$, (b) Temporal behavior of the discharge width in the same gas mixture with Nickel and Copper electrodes*

second measure for discharge inhomogeneity. These definitions of RMS and discharge width can provide a quantitative figure of the growth of discharge instabilities with time, as it is shown below.

Figure 4.5 (a) shows the temporal evolution of the degree of inhomogeneity as determined by Eq. 4.2, for discharges with Nickel and Copper-coated electrodes in a gas mixture of 2 bar He/1 mbar $F_2$. Some of the images of these discharges, used for the data in Fig. 4.5, were shown in Fig. 4.3 (a) and 4.3 (c) respectively. It can be seen from Fig. 4.5 (a) that discharges with Nickel-coated electrodes show lower values of the quadratic mean, i.e., stay homogeneous for about 100 ns before the inhomogeneity increases. In the case of discharges using Copper electrodes, the discharge is homogeneous only for about 50 ns and then the degree of inhomogeneity increases drastically. From Fig. 4.5 (a), it can be seen that the growth rate of the inhomogeneity is lower for discharges with Nickel-coated electrodes. This implies that discharges using Nickel electrodes are more homogeneous than the discharges using Copper electrodes. A common feature of all the discharges shown in Fig. 4.3 is the constriction of the discharge in time. The measured temporal evolution of the discharge width (FWHM), as defined above, is shown in Fig. 4.5 (b). It can be seen in Fig. 4.5 (b) that the rate of decrease of discharge width in discharges with Copper is higher than the discharges with Nickel. It is observed, both qualitatively and quantitatively, that amongst the electrode materials investigated Nickel coated Aluminium

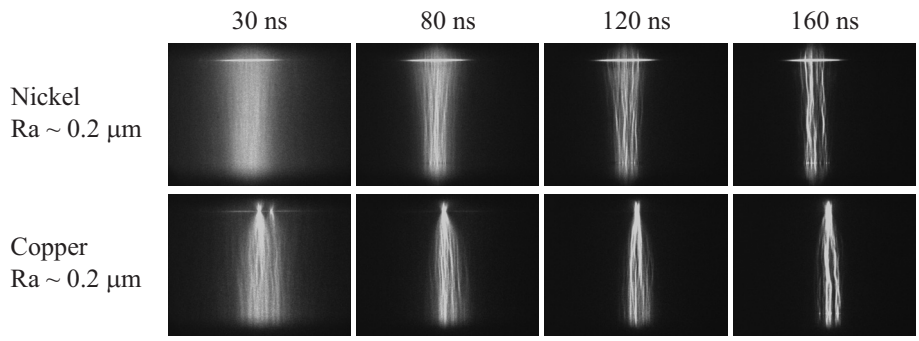


*Figure 4.6: Time evolution of the discharges in gas mixtures of 2 bar He/60 mbar Ar/1.5 mbar $F_2$ with different electrode materials that have the same surface roughness.*

electrodes are best candidates to make homogeneous discharges in $F_2$-based excimer laser gas mixtures.

### 4.2.2 Discharges in ArF excimer laser gas mixtures

In further experiments we found that the properties of discharges with various electrodes in gas mixtures of 2 bar He/1.5 mbar $F_2$/60 mbar Ar are very similar to those in He/$F_2$ discharges. This can be seen in the discharges in ArF laser gas mixtures with Nickel and Copper-coated electrodes which are shown in Fig. 4.6. The figure shows that discharges with Nickel electrodes are initiated very homogeneously at first but at 80 ns, current filaments appear in the discharge. As time progresses, filaments are transforming into arcs which connect the cathode to the anode. It can also be seen that the quality of ArF discharges with Copper electrodes is poor compared to the corresponding discharges in He/$F_2$ mixtures. Hot spots and discharge filaments are formed in the very early phase of the discharge. Already at 30 ns, the discharge can be considered inhomogeneous, moreover, this inhomogeneity grows strongly in time such that arcing is observed from 120 ns on. Another feature of this discharge is that, by 80 ns, the cathode sheath is completely replaced by a single hot spot, which appeared always at the same position. The reason for this could be that since copper is a soft material, maybe it is damaged such that a crater is formed and the discharge always starts there.

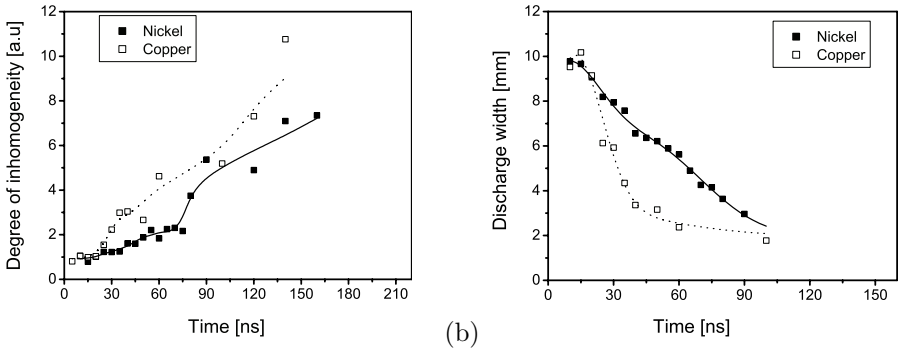


*Figure 4.7: Temporal behavior of (a) degree of inhomogeneity and (b) width, for discharges with Nickel and Copper-coated electrodes in gas mixtures of 2 bar He/60 mbar Ar/1.5 mbar $F_2$.*

The time behavior of the degree of inhomogeneity and discharge width is shown in Fig. 4.7(a) and 4.7(b), respectively. It can be seen that the discharges with Nickel electrodes have a lower degree of inhomogeneity (lower RMS values) than the discharges with Copper electrodes. In discharges with Copper electrodes, the discharge width constricts faster and earlier in time than in the discharges with the Nickel-coated electrodes. The constriction of the discharge width will lead to an increase in the current density and a faster growth of discharge inhomogeneities (will be shown in Sec. 5.1.2). Therefore, it can be concluded that the discharges in ArF laser gas mixtures are more homogeneous with Nickel-coated electrodes than with bulk Copper electrodes.

## 4.3 Influence of surface roughness on the discharge homogeneity in $He/F_2$ gas mixtures

Even though Nickel-coated electrodes provide homogeneous discharges in $F_2$-based excimer laser mixtures, bulk Copper electrodes were used to study the effect of surface roughness of electrodes on the discharge homogeneity. The main motivation for this study was that bulk Copper is easily available and machinable and thus is, technically, to be favoured above the more involved and costly fabrication of coated

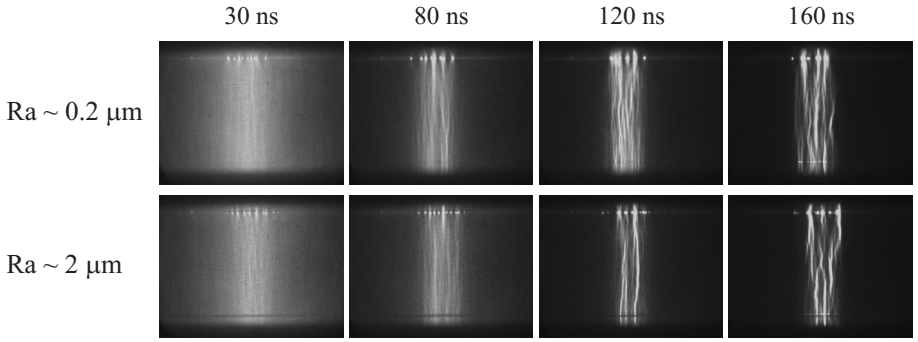


*Figure 4.8: Evolution of the discharges with Copper electrodes with surface roughnesses of* $\sim$ *0.2* $\mu m$ *and* $\sim$ *2* $\mu m$*. The discharges were generated in gas mixtures of 2 bar He/1 mbar* $F_2$*.*

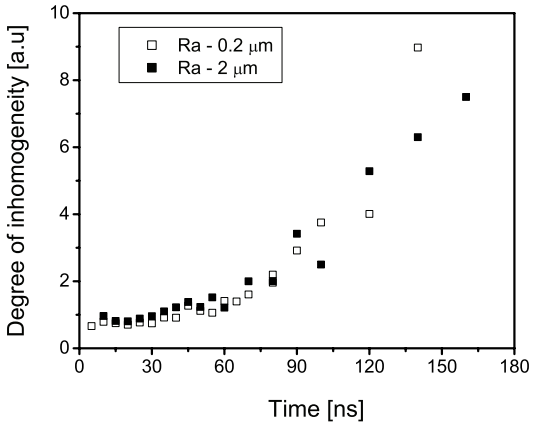


*Figure 4.9: (a) Temporal behavior of the degree of discharge inhomogeneity for discharges with Copper electrodes that have different surface roughness. The measurements were done in a gas mixture of 2 bar He/1 mbar* $F_2$*.*

electrodes. In the hope that a low surface roughness may render also these Copper electrodes as suitable for providing homogeneous discharges, in this study, polished and sandblasted Copper bulk electrodes are compared with each other having an average surface roughness of $\sim$ 0.2 $\mu$m and $\sim$ 2 $\mu$m, respectively as measured at the center of the electrode over an area of 20 x 20 $mm^2$. These electrodes were tested in $F_2$ as well as in ArF laser gas mixtures. Figure 4.8 and Figure 4.9 show qualitatively and quantitatively that the discharge inhomogeneity grows versus time and that, within the experimental error, this growth is the same for both electrode surface roughnesses investigated. Even though it is not shown here, similar results are obtained for polished and sandblasted electrodes in ArF laser gas mixtures. It can be concluded from these measurements that surface roughness of bulk copper electrodes is not an important factor for the discharge homogeneity in $F_2$ laser gas mixtures.

## 4.4 Conclusions

The influence of various electrode materials on the homogeneity of discharges in $F_2$-based excimer laser gas mixtures has been investigated. The study includes Nickel, Chromium, and Gold-coated electrodes as well as bulk Copper, Aluminium, Brass and Stainless Steel electrodes with different surface roughness. For the evaluation of the homogeneity, images of discharges are recorded with an ICCD camera for increasing time delays with respect to the start of the discharge.

A visual evaluation of the homogeneity based on the recorded images is supported by the quantitative characterization of discharge homogeneity (and width) versus time with an image processing method. Both procedures reveal that amongst the electrode materials studied, Nickel coated Aluminium electrodes provide the most homogeneous discharge. In the discharges with other electrodes, the inhomogeneity appeared earlier with respect to the initiation of the discharge. Therefore, Nickel-coated Aluminium electrodes were used for the experiments described in the coming chapters. Moreover, the effect of surface roughness on the discharge uniformity is investigated using bulk Copper electrodes. However, our experimental results show that the surface roughness of the electrodes does not have a significant influence on the homogeneity of discharges in $F_2$-doped excimer laser gas discharges.

# Chapter 5

# Influence of the $F_2$ partial pressure and the pump current density on the discharge homogeneity

In earlier experimental and theoretical studies [24, 84, 88], it has been reported that discharges in gas mixtures of He and $F_2$ remain homogeneous for as long as 150 ns even at $F_2$ concentration of up to 2 %. From these observations it was concluded that the discharge instabilities occuring in KrF lasers should be associated with the presence of Kr, only in whose presence the addition of more $F_2$ accelerates the growth of instabilities. In this chapter, a detailed experimental characterization of discharge instabilities in $F_2$-based excimer laser gas mixtures ($F_2$, KrF, ArF) is presented. We have found that, in spite of the optimum preionisation and the choice of proper electrodes, an initially homogeneous glow discharge transforms into a filamentary discharge after some time and then subsequently into an arc. In contradiction with earlier theories and observations, we found that the discharges in He/$F_2$ mixtures are homogeneous only at very low concentrations of $F_2$ with low current densities. Experimental results are presented which prove that in rare gas $F_2$-based excimer laser gas mixtures, the appearance of discharge filaments is coupled with the presence of $F_2$ rather than heavy rare gas (Kr, Ar) as had been claimed before. By comparing

our experimental results with the theoretical model of Coutts et al. [85], we conclude that the physical mechanism leading to instabilities is local halogen depletion, rather than by multi-step ionisation.

## 5.1 Discharges in $F_2$ laser gas mixtures

The discharge homogeneity in molecular Fluorine laser gas mixtures of Helium and Fluorine and its dependence on various key parameters such as the partial pressure of $F_2$ and the current density is investigated. For this, the temporal development of the discharge fluorescence is monitored with an ICCD camera for a series of consecutive discharges. The goal of these investigations is to identify experimental options for extending the homogeneity of such discharges over extended time intervals and, possibly, also demonstrate such improvements.

### 5.1.1 Effect of $F_2$ partial pressure on the discharge homogeneity

We have investigated the effect of the Fluorine partial pressure on the discharge homogeneity in gas mixtures of He and $F_2$ with a total pressure of 2 bar. In these investigations the partial pressure of Fluorine was varied from 1 mbar to 3 mbar in steps of 0.5 mbar. The steady-state current density for each discharge was kept constant at 35 A $cm^{-2}$ using current limiting resistors in series with the discharge. This steady-state current density current density is measured at 30 ns after the initiation of the discharge, when the discharge area is about 14 x 13 $mm^2$.

The typical temporal shape of the x-ray preionisation signal, the voltage, current and power deposition for a discharge in gas mixtures of 2 bar He and 1 mbar $F_2$ is shown in Fig. 5.1(a). The x-ray pulse is applied about 17 ns after the discharge voltage is applied. It can be seen that, following the breakdown of the gas volume, the voltage reduces to a steady-state voltage of about 6.5 kV while the discharge current rises to a steady-state value of about 60 A. The power deposition during the steady state is about 430 kW. It can be seen that the steady-state voltage of the discharges remains constant for almost 85 ns and then slowly decreases to zero in the next 125 ns. Figure 5.1(b), shows, again, the discharge voltages as a function of time, however, now for various different partial pressures of Fluorine. It can be seen that the higher the Fluorine concentration in the gas mixture, the higher the breakdown voltage and also the steady-state voltage. It can also be seen from Fig.

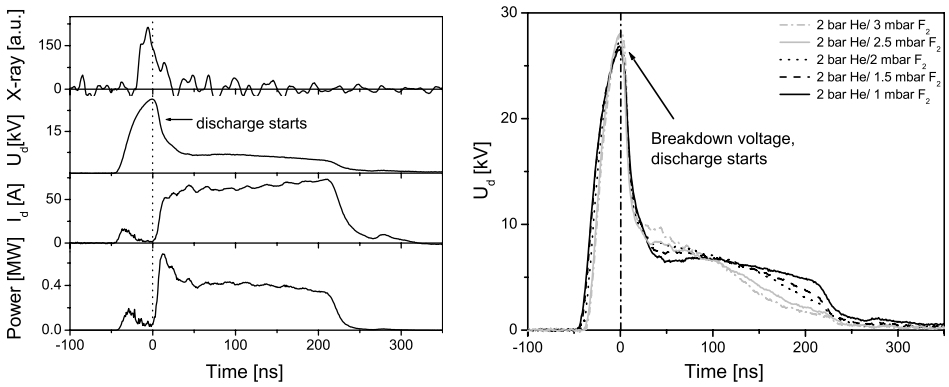


(a) (b)

*Figure 5.1: (a) Temporal behavior of* x*-ray signal, voltage, current and power deposition for a discharge in 2 bar He/1 mbar $F_2$ (b) Temporal behavior of the discharge voltages in gas mixtures of He and $F_2$ with different partial pressures of $F_2$. The total pressure was 2 bar and the current density in all measurements was about 35 A $cm^{-2}$. The distance between the electrodes was 1.7 cm.*

5.1(b) that, as the concentration of Fluorine is increased, the rate of decrease of the steady state voltage becomes larger. The current pulse, however, hardly changes when the Fluorine pressure is raised and is therefore not shown separately. The decrease in the steady-state voltage without any significant change in the current is caused by a decrease in the total discharge impedance, as was explained in Sec. 3.2.3. And the temporally decreasing impedance may imply that, at the time when the discharge impedance starts to decrease, filaments of enhanced electron density appear in the bulk of the discharge and render the discharge inhomogeneous.

This suspected correlation between the onset of the decrease of the steady-state voltage and the moment at which filaments appear was indeed found in the experiments, by comparison with images of the time evolution of the discharges in $He/F_2$ mixtures for different Fluorine concentrations. The images, shown in Fig. 5.2, are taken in consecutive shots at 40 ns, 80 ns, 120 ns and 160 ns after the initiation of the discharge. The spatial resolution of the images was about $\sim 125$ $\mu$m. The gating time of the ICCD camera was 2 ns and the voltage applied to the micro channel plate was the same for all measurements except for those shown in Fig. 5.2 (e). Nevertheless, we

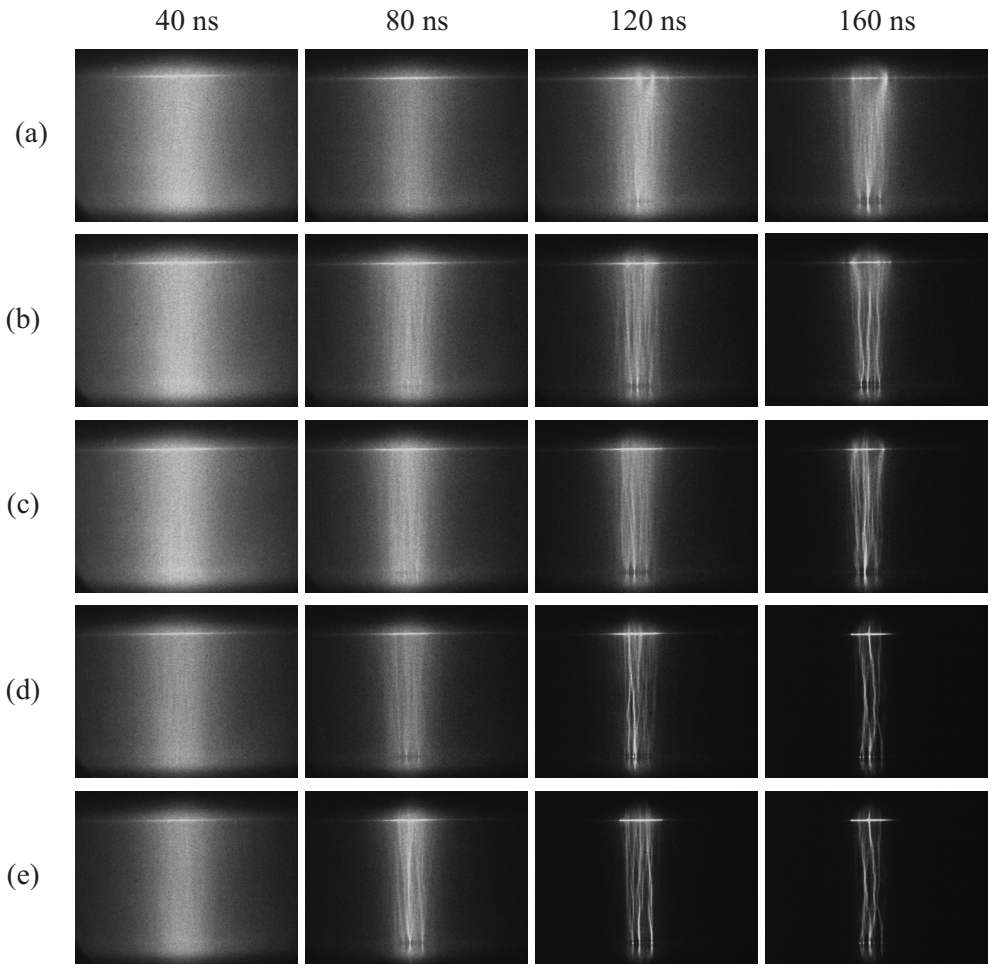


*Figure 5.2: Photographs showing the spatial and temporal development of discharges in gas mixtures of 2 bar He with (a) 1 mbar $F_2$, (b) 1.5 mbar $F_2$, (c) 2 mbar $F_2$, (d) 2.5 mbar $F_2$ and (e) 3 mbar $F_2$. The electrodes were kept at 1.7 cm apart. The gating time of the ICCD camera was 2 ns. The images displayed are taken in consecutive shots at 40 ns, 80 ns, 120 ns and 160 ns after the initiation of the discharge.*

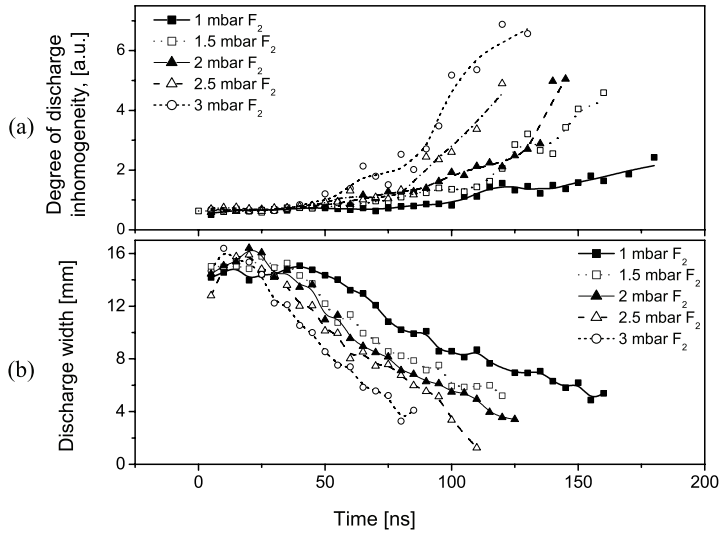


*Figure 5.3: Temporal evolution of (a) the degree of discharge inhomogeneity and (b) the discharge width in gas mixtures of Helium and Fluorine with different Fluorine concentrations. The data points were obtained from Fig. 5.2 using the image processing method described in Fig. 4.4*

note that the absolute intensity of the images cannot be directly compared because, we adjusted the diaphragm of the camera in order to compensate for the low fluorescence intensity towards the end of the pump pulse. The images in Fig. 5.2(a) to 5.2(e) show the discharges in gas mixtures of 2 bar He while the Fluorine pressure is raised from 1 mbar to 3 mbar in steps of 0.5 mbar. The discharges in all gas mixtures appear quite homogeneous up to 40 ns. But as the $F_2$ content increases, the discharge homogeneity decreases and filaments appear earlier in time. For example, when comparing the images at 80 ns for each gas mixture, it can be seen that the discharge in the 2 bar He/1 mbar $F_2$ gas mixture appears quite homogeneous (without any current filaments), but becomes noticeably inhomogeneous for discharges in gas mixtures with higher $F_2$ partial pressure. At 120 ns and at 160 ns, the discharges in all gas mixtures are filamentary. In particular, the intensity and the number of filaments in the discharge volume increases for increasing Fluorine pressure. For 2.5 mbar and 3 mbar $F_2$, the initial homogeneity of the discharge is completely destroyed as no homogeneous discharge background is left, but only filaments are visible. A common

feature of all discharges is that the transverse width of the discharge constricts in time. The images show that the discharge width reduces more rapidly with increasing $F_2$ partial pressure.

In order to investigate the systematics in these discharges on the basis of quantitative measures for the discharge inhomogeneity and width, we used the image processing method described in Sec. 4.2.1, to investigate a larger number of discharges. The time evolution of the degree of discharge inhomogeneity and the discharge width for images such as shown in Fig. 5.2 are calculated and displayed in Fig. 5.3. It can be seen from Fig. 5.3 (a) that the degree of inhomogeneity stays low for about 40 ns after the initiation of the discharge and, afterwards, grows accordingly faster for higher $F_2$ pressures, as was suggested qualitatively by the images in Fig. 5.2. It can also be seen from Fig. 5.3 (b) that, indeed there is a systematic constriction of the discharge with time and with $F_2$ partial pressure. The shrinking of the discharge in time, and thus also the associated increase of the current density during a discharge pulse has, so far not been accounted for correctly, due to the lack of systematic recordings of the discharge width as a function of time. This can lead to an overestimation of the speed with which filaments build up, because an increasing current density is expected to cause a higher speed of filamentation, as will be shown in the next section. As a quantitative measure, we define the discharge stability time $\tau$, as the time at which the the degree of discharge inhomogeneity attains twice its initial value. It is clear from Fig. 5.3 that $\tau$ decreases with increasing amount of $F_2$. The quantitative dependence of $\tau$ on the $F_2$ partial pressure and current density is presented in Sec. 5.4.

The introduction of the discharge inhomogeneity and discharge width measures enables to trace inhomogeneity and discharge width systematically with the $F_2$ pressure. This would thereby allow for a better comparison with a possible theoretical analysis in Sec. 5.4 - an advantage which is difficult to achieve on the basis of individual images due to their high individual complexity.

### 5.1.2 Effect of current density and power deposition on the discharge homogeneity

Besides the $F_2$ partial pressure, important parameters that affect the discharge homogeneity in excimer laser gas mixtures are the current density and the power deposition. This is qualitatively known from previous work of others [96, 100], however, there, a systematic quantification which might be suitable for comparison with theoretical models has been lacking. To present a first systematic characterization of the influence of these parameters on the discharge uniformity, the current density was

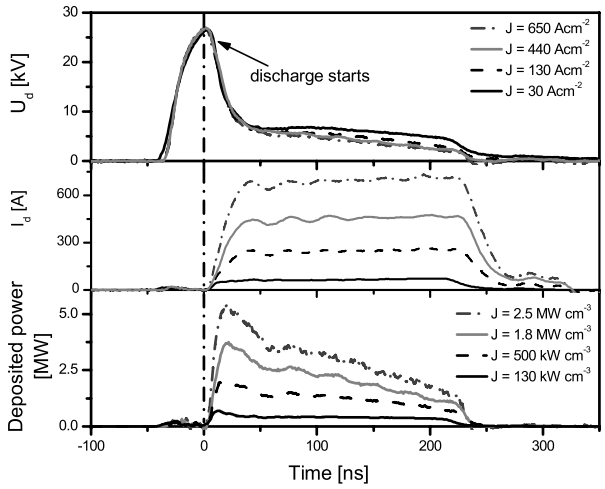


*Figure 5.4: Temporal evolution of the discharge voltage ($U_d$), discharge current ($I_d$) and power deposition in 2 bar He/1 mbar $F_2$ gas mixtures for current densities ranging from 30 A $cm^{-2}$ to 650 A $cm^{-2}$ and power depositions ranging from 130 kW $cm^{-3}$ to 2.5 MW $cm^{-3}$.*

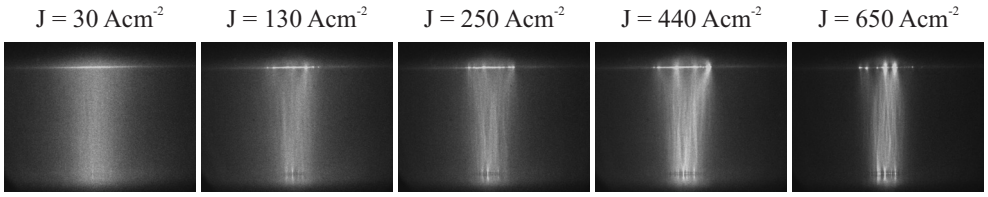


*Figure 5.5: Images of the discharges in a gas mixture of 2 bar He and 1 mbar $F_2$ at various current densities. These images are taken at 80 ns after the initiation of the discharge with the gating time of the ICCD camera set to 2 ns. The experimental conditions are the same as for Fig. 5.4.*

varied for discharges in 2 bar He/1 mbar $F_2$. The current density was set to a value in the range of 30 A cm$^{-2}$ to 650 A cm$^{-2}$, by varying the current limiting resistor (0 to 350 Ω) that is connected in series with the discharge. The corresponding specific power deposition ranges from 130 kW cm$^{-3}$ to 2.5 MW cm$^{-3}$. The x-ray preionisation is applied about 20 ns after the application of the discharge voltage.

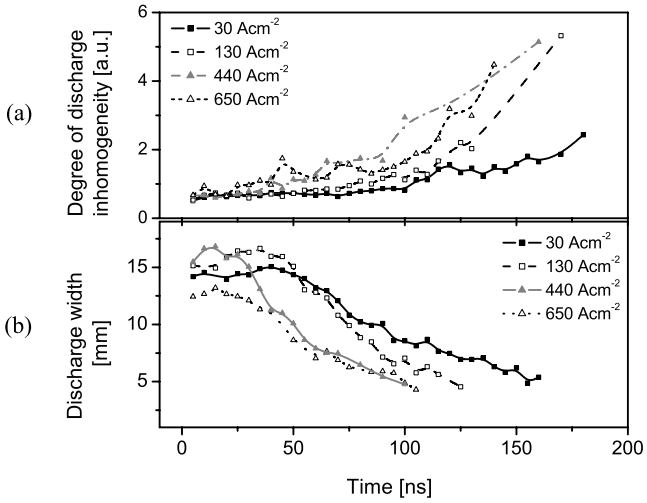


*Figure 5.6: (a) Evolution of the degree of discharge inhomogeneity for various current densities in a gas mixture of 2 bar He/1mbar $F_2$ and (b) corresponding evolution of the discharge width. The data are extracted from the images shown in Fig. 5.5.*

The discharge voltage, current and power deposition at the various current densities are shown in Fig. 5.4. The figure shows that, when the current density (or the specific power deposition) increases, the rate at which the steady-state voltage drops increases. In each case, the current does not vary significantly in time and so the power deposition behaves similar to the voltage. Our comparison of the drop in the steady state voltage, as already discussed in Sec. 5.1.1, as a function of Fluorine partial pressure with correspondingly recorded images shows that the voltage drop, can be addressed to the appearance of discharge filaments. Examples of these recorded images are shown in Figure 5.5, when the current density is raised from 30 to 650 A cm$^{-2}$. The shown images are taken at 80 ns after the initiation of the discharge. From such images, the time evolution of the degree of discharge inhomogeneity and

discharge width are extracted and displayed in Fig. 5.6(a) and (b) as a function of the current density. Both figures show that the discharge inhomogeneity increases and the discharge width constricts with increasing current density. Another feature to be noted in Fig. 5.5, but which is not contained in the data of Fig. 5.6, is that cathode hot spots appear, of which the size and number increases with increasing current density. Our experiments prove clearly that, when the current density and the power deposition increases, the instabilities appear earlier and grow faster. This means that the discharge stability time $\tau$, decreases with increasing current density and power deposition. From Fig. 5.2 and 5.5, it is obvious that discharges in $He/F_2$ gas mixture are not always stable, contradictory to what was predicted in Refs. [24, 84, 88] (see Sec. 2.3.1).

To this end, we compare our observations to previous predictions by others [24,84,88]. There it was claimed that the $He/F_2$ gas mixtures are highly stable against small perturbations in the discharge. However, in contradiction to these predictions, we find that such discharges behave differently, namely these discharges can be unstable and the stability time decreases with increasing $F_2$ partial pressure. We also note that our observations are not based on individual or only a few experimental recordings and their qualitative inspection. Our observation of growing discharge instability with increasing $F_2$ pressure and current density comprise a large number of discharge events inspected with image processing. This approach integrates over the specific filament structure of the individual discharge event and thereby also allows to well quantify our observations.

## 5.2 KrF laser gas mixtures

The specific effect of $F_2$ and Kr on the homogeneity of discharges in KrF laser gas mixtures is investigated by varying their partial pressure in the mixtures. The mixtures are composed of $He/Kr/F_2$ at a total pressure of 2 bar. The distance between the nickel-coated aluminium electrodes was set to 10 mm. The current density in all measurements was kept constant and amounted to about 60 A $cm^{-2}$.

The effect of raising the Kr and $F_2$ partial pressures on the discharge homogeneity is shown in Fig. 5.7. We have observed that the discharges in Fluorine-free mixtures of He/Kr are stable for all Kr partial pressures in the range from 10 to 120 mbar. This can be seen in the examples of Fig. 5.7(a), which shows one earlier and one later stage of the discharge in a 2 bar He/120 mbar Kr gas mixture with no Fluorine present. Figure 5.7(b) shows that discharges in 2 bar He/10 mbar Kr/0.5 mbar $F_2$ remains

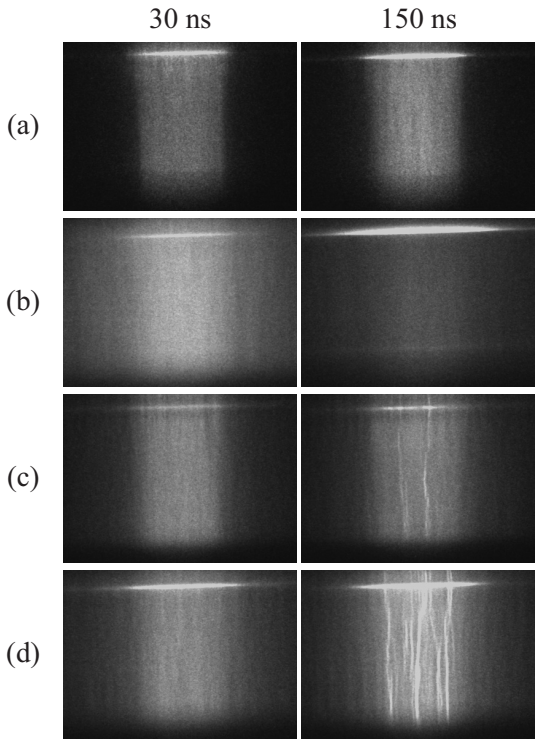


*Figure 5.7: Images of the discharges in KrF laser gas mixtures recorded at 30 ns and 150 ns after the initiation of the discharge: (a) 2 bar He/0 mbar $F_2$/120 mbar Kr, (b) 2 bar He/0.5 mbar $F_2$/10 mbar Kr, (c) 2 bar He/0.5 mbar $F_2$/80 mbar Kr (d) 2 bar He/1 mbar $F_2$/10 mbar Kr. The distance between the electrodes was 10 mm. The current density was kept constant at about 60 A $cm^{-2}$ for all the measurements. The gating time of the camera was kept at 7 ns and the spatial resolution of the images was about 140 $\mu m$.*

homogeneous as well, for the entire duration of the pump pulses of 220 ns. We note that, in this gas mixture, the fluorescence intensity of the discharge drastically reduces towards the end of the pump pulse (at 150 ns). We were not able to compensate this with a larger diaphragm of the camera. However, corresponding images recorded with a larger gain of the micro-channel plate of the ICCD camera (not shown here) reveals that the discharge homogeneity was preserved for even longer durations of the pump pulse (up to 220 ns). The effect of $F_2$ and Kr on the discharge is investigated by adding $F_2$ and Kr separately to the above gas mixture (2 bar He/10 mbar Kr/0.5 mbar $F_2$). The subsequent addition of Kr (30 - 110 mbar) to this mixture does not alter the uniformity of the discharge significantly (see Fig. 5.7(c)), whereas the addition of even a small amount of $F_2$ (by 0.5 mbar to 1 mbar) introduces strong discharge inhomogeneities in the later stage as seen in Fig. 5.7(d).

At this point the important question can be answered whether the physical origin of the observed instabilities in He/$F_2$/Kr mixtures is to be attributed to the presence of Fluorine or to the presence of Krypton. Actually, previous work has claimed that Kr is responsible for the instability, based on a theoretical model [84]. For an answer based on experimental data, we refer to Fig. 5.2, 5.5 (where Kr is absent and the $F_2$ pressure is varied) and Fig. 5.7, where the Kr pressure is varied. It can be clearly seen that the discharge filaments appear in a He/Kr/$F_2$ mixture at the same time as in a Kr free He/$F_2$ mixture with the same concentration of $F_2$. From this we conclude that it is not the Kr but the $F_2$, which makes He/Kr/$F_2$ discharges filamentary, which is in contradiction with the reports of Borisov [84].

## 5.3 ArF laser gas mixtures

The specific effect of Ar and $F_2$ on the homogeneity of discharges in ArF excimer laser gas mixtures is studied by varying their partial pressures in these mixtures. The mixtures are composed of He/Ar/$F_2$ and have a total pressure of 2 bar. The distance between the nickel-coated aluminium electrodes was 1.7 cm. For all the measurements, the current density at 30 ns after the initiation of the discharge was adjusted to a relatively high 300 A $cm^{-2}$ typical for the operation of current ArF excimer lasers, which are operated with rather strong and short current pulses. The corresponding power deposition amounted to 1 MW $cm^{-3}$ as measured in the steady-state part of the discharge. The gating time of the ICCD camera was 2 ns and the spatial resolution of the images was about $\sim 125$ $\mu$m.

The effect of the addition of Ar and $F_2$ on an initially homogeneous glow discharge

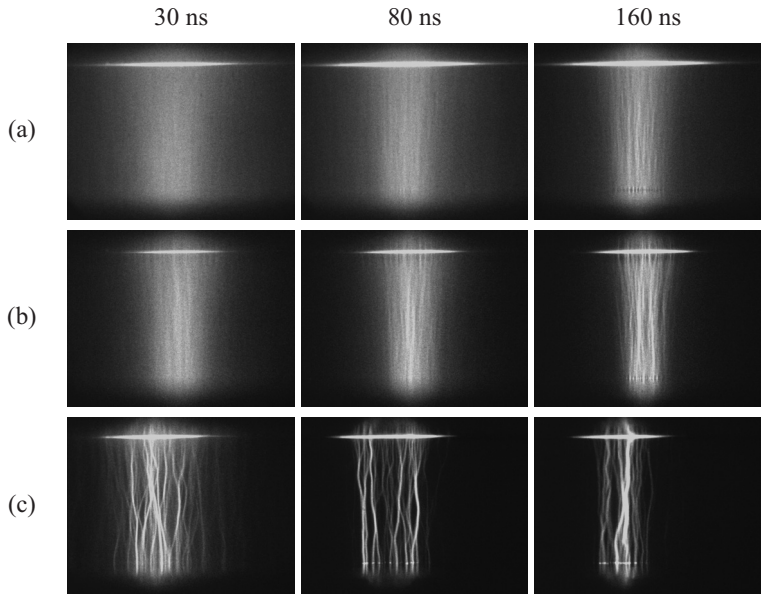


*Figure 5.8: Images of discharges in ArF laser gas mixtures with different compositions at 30 ns, 80 ns and 160 ns after the initiation: (a) 2 bar He/10 mbar Ar/0.5 mbar $F_2$, (b) 2 bar He/100 mbar Ar/0.5 mbar $F_2$, (c) 2 bar He/10 mbar Ar/3 mbar $F_2$. The distance between the electrodes was 1.7 cm. The current density and power deposition in these discharges were 300 A $cm^{-2}$ and 1 MW $cm^{-3}$ respectively. The gating time of the camera was 2 ns and the spatial resolution of the images was $\sim$ 125 $\mu$m.*

in a He/Ar/$F_2$ gas mixture is shown in Fig. 5.8. Figure 5.8(a) shows the discharges in gas mixtures of 2 bar He/0.5 mbar $F_2$/10 mbar Ar (i.e., 0.025% of $F_2$). It can be qualitatively seen that with this mixture the discharge remains homogeneous for about 80 ns and that at 160 ns, weak filaments appear in the bulk of the discharge with the intensity of the filaments increasing towards the end of the pump pulse. From this, once again one can see that, even with such very low $F_2$ concentration as 0.025 %, the discharge becomes inhomogeneous when the current density is high. To investigate the influence of Ar on the discharge homogeneity, the partial pressure of Ar in the initial gas mixture was increased to ten-fold up to 100 mbar while keeping the $F_2$ concentration constant. It can be observed qualitatively in Fig. 5.8(b) that

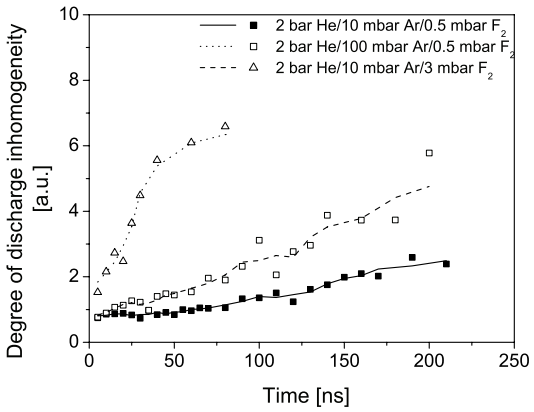


*Figure 5.9: Evolution of the degree of discharge inhomogeneity for various Ar and $F_2$ concentrations in 2 bar He/Ar/$F_2$ gas mixtures. The data are extracted from the images shown in Fig. 5.8*

the discharge inhomogeneity grows only slightly faster by the addition of Ar. On the contrary, when the partial pressure of $F_2$ in the initial gas mixture was increased from 0.5 mbar to 3 mbar, the discharge homogeneity degrades very rapidly as shown in Fig. 5.8(c). From the latter images, it can be seen that the discharges in gas mixtures of 2 bar He/3 mbar $F_2$/10 mbar Ar are not stable. It can be observed that this discharge is already strongly inhomogeneous at 30 ns after the start of the discharge. Current filaments are apparent which, later in time, transform into arcs that connect the electrodes.

In order to translate these qualitative statements (based on images of specific filaments at specific times in individual discharge events) into quantitative statements on the typical development of the discharges, we processed a larger number of images as the ones in Fig. 5.8. Fig. 5.9 shows the evolution of degree of discharge inhomogeneity extracted from these images. From Fig. 5.9, it can be seen that the degree of discharge inhomogeneity in 2 bar He/0.5 mbar $F_2$/10 mbar Ar increases only slightly with time. Also one can see how quickly, in comparison, the discharge inhomogeneity grows with the addition of 3 mbar $F_2$. We note that the findings on Fig. 5.9 are much similar to what have been observed with excimer laser gas mixtures containing Kr. In both cases the addition of heavy rare gas does not significantly increase the inhomogeneity of discharges while, in both cases, an increasing pressure of $F_2$ causes a quick increase

of the inhomogeneity.

Our experimental results thus show that in $F_2$–based laser gas mixtures, the appearance of discharge filaments is caused by the presence of $F_2$ and physical effects associated with $F_2$. In contrast, the presence of heavy rare gases like Kr or Ar, such as physical processes leading to instabilities via heavy noble gases, can be ruled out, other than proposed before [84].

These findings, apart from being important for an improved modeling of discharges in such gas mixtures with high technological importance, seem to offer additional options. In particular, it may be considered to add (besides Ar and Kr) other types of heavy rare gases as well, such as Xe in order to quantify its influence on the discharge homogeneity for long durations of the pump current pulse. For example, it can be suspected that the low ionization energy of Xe might lead to an improved stabilization of the discharge, when the formerly presumed destabilizing effect [84] is small. Corresponding experimental investigations will be presented in Chapter 6 and, indeed, it shows that the addition of Xe stabilizes Fluorine-based discharges driven by long current pulses.

## 5.4 Experimental evidence for the validity of halogen depletion instability theory

With the parametric measurements of discharge homogeneity as presented in sec. 5.1.1 and 5.1.2, it is possible for the first time, to directly examine whether the so-called mechanism of halogen depletion, i.e., a local consumption of the ($F_2$) halogen donors is the cause of discharge instabilities in the corresponding lasers. A detailed description of this mechanism has been given by Coutts and Webb [85] Their description of the halogen depletion instability is summarized in theoretical predictions on how the time for a discharge to become unstable should depend on the density of the donor and the density of electrons initially present in the discharge. Here, we recall the essential parts from this theory in order to test its validity for $F_2$–based excimer lasers based on the comparison with our experimental results.

The most specific prediction of the model is that, if halogen depletion were responsible for the observed growth of inhomogeneity of the discharges, one would, similar to Eq. 2.21, expect that the discharge stability time $\tau$ (defined as in Sec. 5.1.1) follow a specific dependence. Specifically, one would expect that the inverse square of the stability time, decreases in proportion with the initial electron density, $n_{e0}$, and in

proportion with the initial fluorine density, $[F_2]_0$, i.e.,

$$1/\tau^2 \sim \frac{1}{2} {k_a}^2 n_{e0} [F_2]_0 \tag{5.1}$$

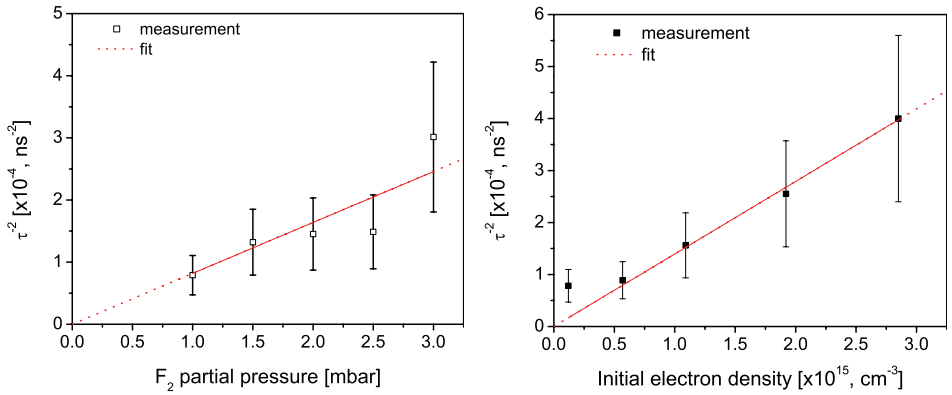


(a) (b)

*Figure 5.10: (a) Inverse square of the measured discharge stability time ($1/\tau^2$) in gas mixtures of 2 bar He and $F_2$ as a function of initial $F_2$ partial pressure. The current density was kept constant at 35 A cm$^{-2}$ in all measurements (b) Inverse square of measured discharge stability time ($1/\tau^2$) as a function of initial electron density. The gas mixture was composed of 2 bar He and 1 mbar $F_2$.*

Figure 5.10 (a) and 5.10 (b) shows the inverse square of the measured discharge stability time ($1/\tau^2$) as a function of the partial pressure of $F_2$ and the initial electron number density at the start of the glow phase of the discharge. The initial electron density $n_{e0}$ is determined from

$$n_{e0} = J_0/q\nu_d \tag{5.2}$$

where $J_0$ is the measured initial current density, $q$ is the electronic charge and $\nu_d$ is the electron drift velocity for the measured value of E/N ($\approx$ 7.6 x 10$^{-17}$ V cm$^2$, which is the ratio of the electric field to buffer gas density) [125]. For determining the current density, we take the measured current at 30 ns after the start-up of the

discharge when the current reaches its steady-state value. It can be seen in Fig. 5.10 (a) and 5.10 (b) that, indeed, to rather good approximation, the inverse square of the stability time increases proportionally with increasing $n_{e0}$ and $[F_2]_0$ as predicted by Eq. 5.1. We conclude from this agreement that the depletion of halogen is responsible for the growth of instabilities in $F_2$-based excimer lasers. More specifically, Fig. 5.10 also suggests how to extend the stability time for such excimer lasers, namely by choosing a lower current density and lower partial pressure of $F_2$.

Figure 5.10 confirms now also quantitatively and in line with our experimental results for He/Kr/$F_2$ and He/Ar/$F_2$ mixtures, the appearance of discharge filaments is coupled with the presence of $F_2$ rather than heavy rare gases like Kr and Ar. Most importantly, Fig. 5.10 proves that halogen depletion, rather than the stepwise ionisation is the main instability growth mechanism in Fluorine based excimer laser gas discharges.

## 5.5 Conclusions

In summary, experimental evidences are presented showing that discharges in He/$F_2$ gas mixtures are not stable, which is in contradiction with previous observations and models. Instead, images of the discharge fluorescence taken with high spatial and temporal resolution at various times after the initiation of the discharges show that, even under the optimised start-up conditions, a homogeneous glow discharge eventually turns into an inhomogeneous discharge containing numerous filaments where the intensity and number of these filaments increases with time. To enable a novel and quantitative measure of spatio-temporal developments for a parametric characterization, a numerical processing of the recorded images (as developed in Chapter 4) was applied. This tool allows, for the first time, a quantitative comparison with theory and from this, we come to the following findings. The filament formation in He/Kr/$F_2$ and He/Ar/$F_2$ excimer laser gas mixtures is associated mainly with the presence of $F_2$ and not with the Kr or Ar concentration. As an example we show that in gas mixtures of He/$F_2$ the time interval over which the discharge stays uniform decreases inversely with the square root of the initial partial pressure of $F_2$ and inversely with the square root of the initial electron density (or with the square root of the current or specific power deposition). The measured dependence of the discharge stability time on the $F_2$ partial pressure and the electron density is compared with the halogen depletion instability theory proposed by Coutts and Webb and a good agreement is found. The results presented in this chapter thus provide strong experimental evidence that local depletion of the halogen donor molecules is responsible for the formation of discharge

instabilities in $F_2$-based excimer lasers. These instabilities are the main reason for a premature termination of the output radiation in such lasers, when pumping them with current pulses of long duration for the purpose of increasing the beam quality. Our observations thereby indicate that such lasers can be designed for a higher beam quality by optimising the electron density and the Fluorine density.

# Chapter 6

# Stabilisation and temporal extension of stable glow discharges in $F_2$ and ArF excimer laser gas mixtures

This chapter reports on the effect of the buffer gas, either He or Ne, and small amounts of heavy rare gases (Kr and Xe) on the discharge uniformity in $F_2$ and ArF excimer laser gas mixtures. Our experiments show that discharges in $Ne/F_2$ gas mixtures are stable for a longer period of time ($\sim$ 200 ns) than discharges in $He/F_2$ gas mixtures ($\sim$ 80 ns). Furthermore, it is observed that the addition of small amounts of Xe, up to partial pressures of 0.53 mbar, improves significantly the discharge uniformity and extends the stable phase of discharges in $He/F_2$ as well as in $He/Ar/F_2$ and $Ne/Ar/F_2$ excimer laser gas mixtures from 80 ns to about 200 ns. A concern with this may be that addition of Xe will lead to the formation of XeF excimers which can hinder the formation of ArF excimers during discharges in He(or Ne)/$Ar/F_2$ gas mixtures, and thereby reduce the ArF laser inversion and gain. However, monitoring the spontaneous emission from ArF excimers (at 193 nm) reveals that adding up to 1.3 mbar Xe does not affect the formation of ArF excimer molecules.

## 6.1 Effect of the buffer gas on discharges in $F_2$ laser gas mixtures

The gas mixture plays a critical role in the generation of stable glow discharges in excimer laser gas mixtures. In Chapter 5, we discussed the influence of $F_2$ and the heavy rare gas, from which the excimer molecule is formed, on the homogeneity of the discharge. Here we investigate the influence of the buffer gas on the quality of the discharge. In discharge pumped excimer lasers, either He or Ne is used as buffer gas. It is reported that the use of Neon, rather than Helium, increases the pulse length of the most commonly used excimer lasers, i.e. the XeCl, KrF and ArF lasers, resulting in an improved energy extraction [20, 52, 126]. Here we investigate the effect of both He and Ne on the discharge uniformity in $F_2$ excimer laser gas mixtures. For this we monitor the temporal and spatial development of discharge instabilities in the gas mixtures.

The measurements were conducted in $F_2$ laser gas mixtures with a gas composition of 2 bar He or Ne and 1 mbar $F_2$. Figure 6.1 shows the measured time evolution of the voltage, current and power deposition for discharges in both mixtures. It can be seen in Fig. 6.1(a) that for Helium-buffered mixtures, the breakdown of the gas occurs at about 27 kV. After 35 ns, the discharge reaches steady state in which the voltage drops to about 6.7 kV. The current through the discharge reaches then a value of about 435 A. From this, the current density and pump power deposition at this time were determined to be about 440 A $cm^{-2}$ and 1.8 MW $cm^{-3}$, respectively. Fig. 6.1(a) also shows that the steady state voltage across the discharge decreases towards the end of the pump pulse, while the current slightly increases. The lower steady state voltage at which filaments operate [34] leads to the observed increase of the discharge current.

Fig. 6.1(b) shows that the breakdown of $Ne/F_2$ mixtures occurs at 24 kV which is somewhat a lower voltage than measured for He-buffered discharges. The steady state voltage amounts to 2.3 kV, which is nearly a factor of three smaller than the steady state voltage measured for He-buffered mixtures. This difference between He and Ne can be understood as follows. The steady state voltage needed to operate a self sustained discharge in He is much higher because the higher voltage has to compensate for the high energy losses in the elastic collisions between electrons and He atoms (more energy is lost when the ratio between electron mass and atom mass is smaller).

The discharge current reaches its steady state value of 500 A in about 30 ns. The current density and pump power density were about 400 A $cm^{-2}$ and 400 kW $cm^{-3}$,

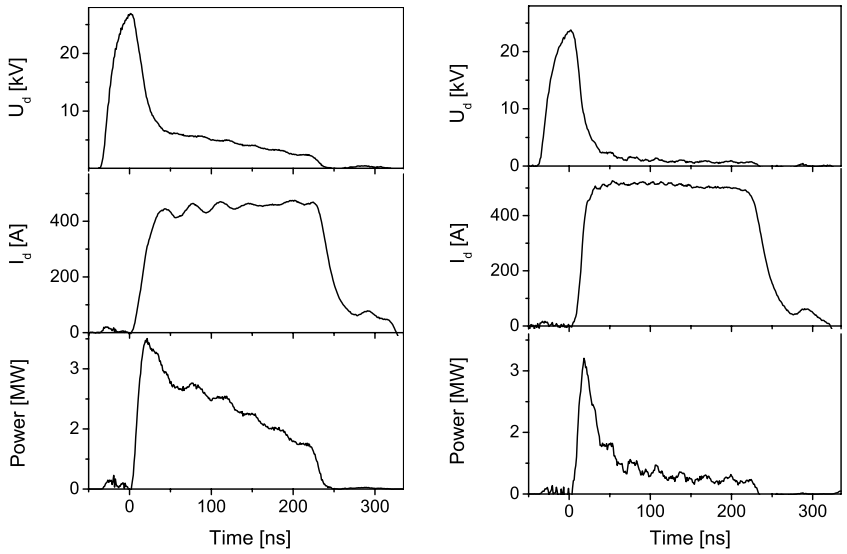


*Figure 6.1: Temporal behavior of discharge voltage ($U_d$), discharge current ($I_d$) and power deposition in gas mixtures of (a) $He/F_2$, (b) $Ne/F_2$. The current density and pump power density in $He/F_2$ mixtures were about 440 A $cm^{-2}$ and 1.8 MW $cm^{-3}$ and in $Ne/F_2$ mixtures about 400 A $cm^{-2}$ and 400 kW $cm^{-3}$ respectively.*

respectively. It can be seen that the steady state voltage decreases only slightly with time. As will be seen in Fig. 6.2, the filamentation of the discharge proceeds much slower compared to discharges in the He-buffered mixture and has therefore a much smaller influence on the development of the steady state voltage. This is also reflected in the discharge current which remains nearly constant during the pump pulse duration. The power deposition in the Ne buffered mixture is much smaller than in the He buffered gas mixture. This results from the lower steady state voltage at which the discharge in the Ne buffered mixture operates.

Figure 6.2 shows images of the spatio-temporal development of discharges in $He/F_2$ and $Ne/F_2$ gas mixtures. The images were taken in consecutive shots at 30 ns, 80 ns and 160 ns after the initiation of the discharge. The gating time of the camera was set to 2 ns and was kept constant for all measurements. The spatial resolution of

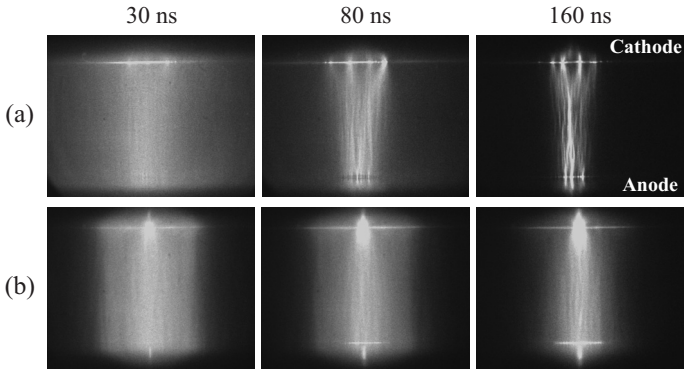


*Figure 6.2: Photographs showing the effect of buffer gas on the discharge uniformity. (a) 2 bar He/1 mbar $F_2$, (b) 2 bar Ne/1 mbar $F_2$. These images were recorded at 30 ns, 80 ns and at 160 ns after the initiation of the discharge with a camera gating time of 2 ns. The distance between the electrodes was 17 mm. The current density and pump power density in (a) were about 440 A $cm^{-2}$ and 1.8 MW $cm^{-3}$ and in (b) were about 400 A $cm^{-2}$ and 400 kW $cm^{-3}$ respectively.*

the images was 125 $\mu$m. Figure 6.2(a) shows that in Helium buffered gas mixtures, small hot spots appear at the cathode by 30 ns, but the bulk of the discharge appears homogeneous. Later in time, filaments become visible in the bulk of the discharge which connect to the hot spots. By 80 ns the homogeneity is already much deteriorated and at 160 ns, the homogeneous glow has completely disappeared and the discharge constricts into an arc. We found that the number and position of hot spots are not reproducible in these discharges.

In Neon buffered discharges the development is rather different. A single large hot spot appears at the cathode in the initial stage of the discharge (30 ns) as can be seen from Fig. 6.2(b). It remains in the same position on the cathode up to the end of pump pulse. At 80 ns, weak filaments originating from the hot spot become visible against the background of the homogeneous glow. Although by 160 ns, these filaments have grown more intense, the discharge homogeneity is preserved to a great extent. The constriction of the discharge in $Ne/F_2$ gas mixtures is rather low compared to that in $He/F_2$.

For a quantitative characterisation, the time evolution of the degree of discharge inhomogeneity for the He and Ne buffered mixtures determined from Fig. 6.2 is shown

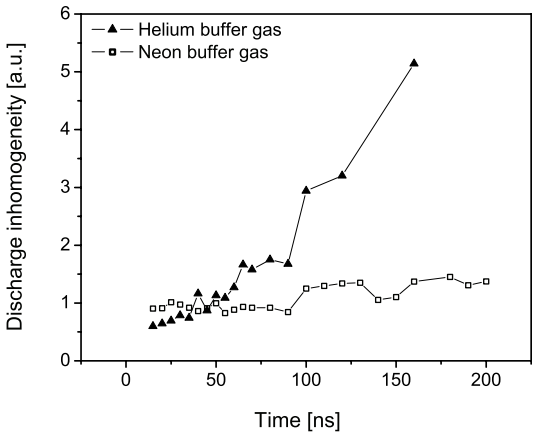


*Figure 6.3: Time evolution of discharge inhomogeneity in gas mixtures with 2 bar He/1 mbar $F_2$ and 2 bar Ne/1 mbar $F_2$. The current density and pump power density in He-buffered mixtures were about 440 A $cm^{-2}$ and 1.8 MW $cm^{-3}$ and in Ne-buffered mixtures were about 400 A $cm^{-2}$ and 400 kW $cm^{-3}$ respectively.*

in Fig. 6.3. It can be seen that the degree of inhomogeneity for discharges in $He/F_2$ mixtures increases rapidly with time, while it increases only slowly for discharges in $Ne/F_2$.

A reason for the higher degree of homogeneity in Ne based discharges may be the lower attachment rate for electrons to $F_2$ in this mixtures. Sze and Ohwa et al. have shown that in $Ne/F_2$ mixtures a smaller density of low energy electrons is available in the electron energy distribution as compared to $He/F_2$ mixtures [7, 20, 127]. This reduces the attachment rate of electrons to $F_2$ [53] in $Ne/F_2$ mixtures compared to attachment in $He/F_2$ mixtures such that halogen depletion and the growth of instabilities proceeds slower in $Ne/F_2$ mixtures.

From our observations, it can be concluded that discharges in Ne buffered gas mixtures are much more stable than He buffered discharges, making possible the longer optical pulse durations obtained in KrF and ArF lasers with Ne based gas mixtures [52, 126].

## 6.2 Stabilising effect of Xe on discharges in $F_2$-based excimer laser gas mixtures

So far $F_2$-based excimer lasers exclusively work with relatively short (< 30ns) pulses. However, maintaining a stable discharge over several hundreds of nanoseconds is the key requirement to obtain a high beam quality from $F_2$-based excimer lasers, which involves the elimination or suppression of discharge instabilities. With the goal to increase the output power (efficiency) of short pulse excimer lasers, adding various types of gases is an obvious experimental approach. In the case of $F_2$-based lasers Kataoka et.al. [128] have indeed shown that the addition of a very small amount of Xenon (at ppm level) increased the output energy, of an ArF laser. This increase was addressed to an improved quality of the discharge. But those investigations remained limited to short pump pulses (< 30ns) where the growth of instabilities is much less critical compared to discharges where instabilities are to be suppressed for hundreds of nanoseconds.

Here, in contrast, we investigate the homogeneity of long-pulse discharges when heavy rare gases (Kr or Xe) are added to $F_2$ as well as ArF laser gas mixtures. The effects of the addition of noble gases on the discharge uniformity are monitored with the ICCD camera.

### 6.2.1 Improvement of discharge uniformity by adding Xe to $F_2$ laser gas mixtures

In order to obtain results that are relevant for the majority of current $F_2$-based excimer lasers, the evolution of the discharge homogeneity is studied in a typical $F_2$ laser gas mixture of 2 bar He/1 mbar $F_2$ to which up to 1.3 mbar Xe was added in steps. A He buffered gas mixture was chosen for its higher small signal gain compared to Ne/$F_2$ mixtures [30]. During our initial investigations on the discharge evolution it was observed that the discharge area changes with the Xe partial pressure in the gas mixture, which affects the current density in the discharge and would therefore render results that are difficult to compare for the various Xe admixtures. However, by varying the resistance placed in series with the discharge, the current (at 30 ns) was adjusted to such a value that the current density in the discharge remains at about 140 A $cm^{-2}$, independent of the chosen Xe pressure. The corresponding specific power deposition at the onset of the steady-state discharge at 30 ns amounts to about 500 kW $cm^{-3}$.

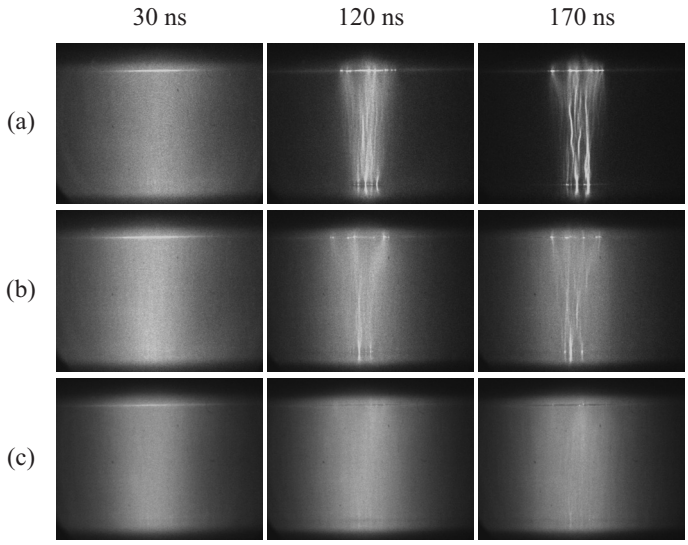


*Figure 6.4: Images showing qualitatively the time evolution of discharges in mixtures of 2 bar He and 1 mbar $F_2$, with and without Xenon addition: (a) without Xe, (b) with 0.013 mbar (10 mTorr) Xe added, (c) with 0.08 mbar (60 mTorr) Xe added. The images are recorded at 30 ns, 120 ns and 170 ns after the initiation of the discharge. The gating time of the ICCD camera was set to 2 ns. The current density in these discharges was about 140 A $cm^{-2}$ and the pump power density was about 500 kW $cm^{-3}$.*

The effect of the addition of Xe on the homogeneity of the discharge is shown in the images displayed in Fig. 6.4. These images are recorded in consecutive shots at 30 ns, 120 ns and 170 ns after the initiation of the discharge. Figure 6.4(a) shows the case with a 2 bar He/1 mbar $F_2$ gas mixtures without any Xenon. From the image taken at 30 ns, it can be seen that the discharge starts very homogeneously. However, by 120 ns filaments appear in the bulk of the discharge volume and the discharge uniformity is strongly deteriorated. Later, at 170 ns, the discharge constricts into a few intense filaments. Figure 6.4(b) shows the images of the discharge after adding 0.013 mbar of Xe to the base mixture of 2 bar He/1 mbar $F_2$. It can be seen that the discharge homogeneity is improved significantly with the addition of Xe. However, weak filaments still can be observed in the bulk of the discharge at 120 ns and more

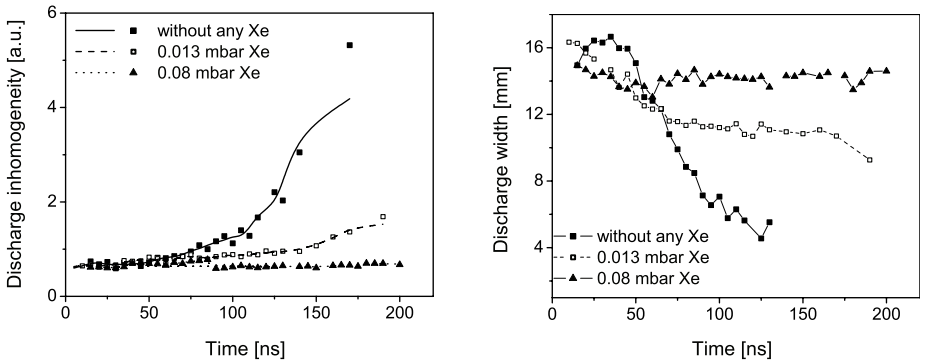


(a) (b)

*Figure 6.5: Temporal behavior of (a) the degree of discharge inhomogeneity and (b) discharge width in a gas mixture of 2 bar He/1 mbar $F_2$ with and without addition of Xe. The current density was about 140 A $cm^{-2}$ and the power density was about 500 kW $cm^{-3}$.*

filaments appear towards the end of the pump pulse (170 ns). Figure 6.4(c) shows the images of the discharge after adding 0.08 mbar (60 mTorr) of Xe to the $He/F_2$ gas mixture. It can be seen that Xenon homogenises the discharge for a duration of up to 170 ns. Although not shown in Fig. 6.4 (see Fig. 6.5), images taken later in time show that the discharge stays uniform even up to the end of the pump pulse at 220 ns. Another feature to be noted is that with the addition of 0.08 mbar Xe to the base mixture of $He/F_2$, the discharge width remains almost constant from the initiation up to the end of the discharge. With adding more Xe, up to partial pressures of 1 mbar, we found that that this does not further improve the discharge homogeneity.

Figure 6.5 shows the time evolution of the degree of discharge inhomogeneity and discharge width in 2 bar He/1 mbar $F_2$ mixtures with and without Xenon, as extracted from images in Fig. 6.4. Figure 6.5(a) shows that the rate of increase of discharge inhomogeneity drops dramatically with the addition of Xe. Moreover, it can be seen that by adding 0.08 mbar Xe, the discharge inhomogeneity remains small up to the end of the pump pulse at 220 ns. The rate at which the discharge constricts also drops with the addition of Xe as shown in Figure 6.5(b). It can be seen that when 0.08 mbar Xe is added, the discharge width remains nearly constant for the entire pump pulse duration. From these experiments, it can be concluded that the addition

of a small amount of Xe (0.08 mbar) improves strongly the uniformity of discharges in $He/F_2$ laser gas mixtures. In addition, the extra Xe extends the stable phase of the discharge up to durations of 220 ns. These results show that there might be a significant potential for long-pulse, high beam quality $F_2$ excimer lasers based on a low concentration Xe admixture.

The effect of addition of small amount of Ne on the uniformity of discharges in 2 bar He/1 mbar $F_2$ gas mixtures was also investigated. It was found that the discharge uniformity does not improve significantly even when up to 200 mbar of Ne was added.

### 6.2.2 Improvement of discharge uniformity by adding Xe to ArF laser gas mixtures

Motivated by the clear improvement of homogeneity in long-pulse discharges in $F_2$/He, we investigated also the evolution of the discharge homogeneity in ArF laser gas mixtures to which Xe is added. The measurements were performed using a base gas mixture composed of He or Ne as buffer gas, 60 mbar Ar and 1.5 mbar $F_2$ at a total pressure of 2 bar, which is typical for ArF excimer lasers. To this mixture, Xe was added in steps, up to a partial pressure of 1.3 mbar. From the ICCD images of the discharge it could again be seen that the discharge area changed with the Xe partial pressure, which influences the current density in the discharge. By varying the resistance (from 0 to 110 Ω) placed in series with the discharge, however, the current is adjusted to such a value that the current density in the discharge amounts to 340 A $cm^{-2}$ and 390 A $cm^{-2}$ for the He and Ne buffered mixture, respectively (at about 30 ns after the initiation of the discharge).

Figure 6.6(a) shows the temporal evolution of the discharge voltage, current and pump power for He buffered base gas mixtures, without and with addition of 0.53 mbar and 1.3 mbar Xe. It can be seen that the presence of Xe lowers the breakdown voltage slightly from 17.5 kV to 17.2 kV. The steady state voltage (5.9 kV), on the other hand, is not affected and remains the same for the gas mixtures without and with 0.53 mbar Xe during the entire pump pulse duration. However, it is slightly less (5.7 kV) for mixtures with 1000 mTorr Xe. During the pump pulse the steady state voltage is seen to decrease from about 6 kV, immediately after breakdown, to 2 kV at the end of the pulse. To keep the current density in the mixture with and without Xe at the same value of 340 A $cm^{-2}$, the current in the mixture with Xe was raised from 150 A to about 530 A. This resulted in a corresponding increase of the power deposition. The pump power density at 30 ns after the start of the discharge amounted to about 1.3 MW $cm^{-3}$.

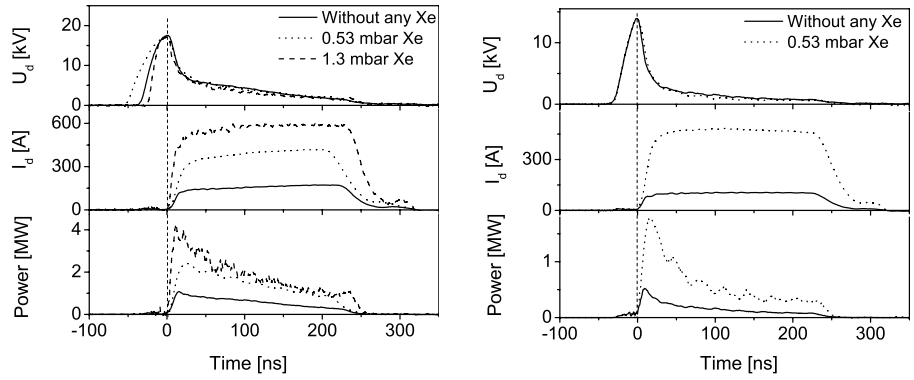


*Figure 6.6: Temporal behaviour of the discharge voltage, current and power deposition in (a) 2 bar He/1 mbar $F_2$/60 mbar Ar without Xe, with 0.53 mbar Xe and with 1.3 mbar Xe, (b) 2 bar Ne/1 mbar $F_2$/60 mbar Ar without Xe and with 0.53 mbar Xe. The pump power density and the current density for (a) was about 1.3 MW cm$^{-3}$ and 340 A cm$^{-2}$ and for (b), the corresponding values were about 410 kW cm$^{-3}$ and 390 A cm$^{-2}$.*

Figure 6.6(b) shows the typical waveforms of the voltage, current and power deposition for discharges in a Ne buffered gas mixture to which 0.53 mbar Xe is added, and in a mixture without any Xe. The breakdown voltage is found to be equal for both mixtures, while the steady state voltage for the discharge in the mixture with Xe is slightly less. To keep the current density at 390 A cm$^{-2}$ for the mixture with and without Xe (at about 30 ns after the initiation of the discharge), the resistance (113 Ω) connected in series with the discharge was removed. This leads to the observed increase of the current from 100 A to 450 A. Correspondingly, the pump power rose by more than a factor of four.

Figure 6.7 shows the dramatic improvement of the discharge uniformity when 0.53 mbar Xe is added to He and Ne buffered gas mixtures. The images are taken in consecutive shots at 30 ns, 80 ns and 160 ns after the initiation of the discharges. Figure 6.7(a) shows the discharges in a He-buffered gas mixture without any Xe. It can be seen that weak filaments are formed already as early as 30 ns after the initiation of the discharge and that these filaments get more intense with time. At about 80 ns the discharge becomes rather non-uniform, and by 160 ns, current filaments take over the

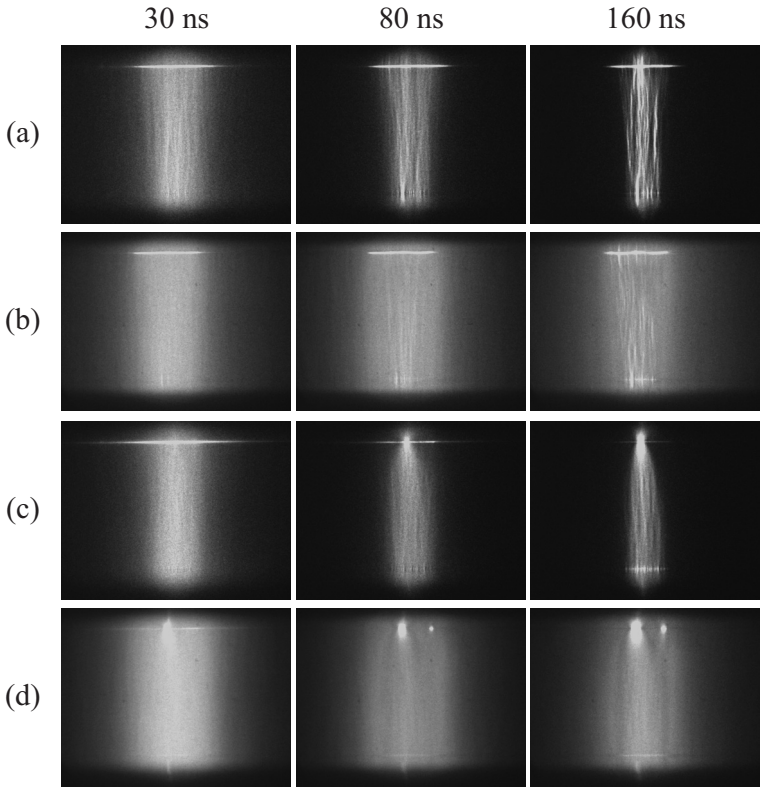


*Figure 6.7: Images showing the time evolution of discharges in ArF excimer laser gas mixtures, with and without Xenon addition. The images are taken at 30 ns, 120 ns and 160 ns after the initiation of the discharge in (a) a mixture of 2 bar He/60 mbar Ar/1.5 mbar $F_2$, (b) the same mixture as in (a), but with 0.53 mbar (400 mTorr) Xe added, (c) a mixture of 2 bar Ne/1.5 mbar $F_2$/60 mbar Ar and (d) the same mixture as in (c), but with 0.53 mbar (400 mTorr) Xe added. The pump power density and the current density in (a) and (b) are about 1.3 MW $cm^{-3}$ and 340 A $cm^{-2}$ respectively. In (c) and (d), they are about 410 kW $cm^{-3}$ and 390 A $cm^{-2}$ respectively. The gating time of the camera was set to 2 ns.*

homogeneous discharge glow and the homogeneity deteriorates completely. Another feature to be noted is that the discharge width constricts considerably towards the end of the pump pulse. To the He base gas mixture, varying amounts of Xe (0.027 mbar to 1.3 mbar) were added in steps. For Xe additions up to partial pressures of 0.053 mbar, no notable effects on the discharge uniformity was observed (images not shown here). However, when the amount of Xe is raised further to 0.13 mbar (100 mTorr), the discharge homogeneity increases noticeably and only after a discharge duration of about 100 ns thin current filaments appear (images not shown here). A further increase of the Xe partial pressure to 0.53 mbar results in a further improvement of the discharge homogeneity which is preserved for a longer time (160 ns) as shown in Fig. 6.7(b). From the image taken at 30 ns it can be seen that the discharge starts very homogeneously, although by 80 ns weak filaments appear in the discharge. Up to 160 ns, the filamentation of the discharge increases only slightly, after which, at 200 ns (image not shown in Fig. 6.7(b)), the homogeneity of the discharge has seriously degraded. The addition of more Xe up to partial pressures of 1.53 mbar does not improve the discharge homogeneity much more.

Similar investigations were carried out with Ne buffered ArF laser gas mixtures. The base gas mixture was composed of 2 bar Ne, 60 mbar Ar and 1.5 mbar $F_2$, to which an increasing amount of Xe is added. The discharge was operated at a current density of about 390 A $cm^{-2}$ and a pump power density of about 410 kW $cm^{-3}$. The power density in Ne buffered gas mixtures is lower than that in He buffered mixtures due to the lower steady state voltage of these discharges. Figure 6.7(c) shows images of the discharges without Xe addition. It can be seen that this discharge is homogeneous up to about 120 ns. Thereafter, filaments appear in the bulk of the discharge and by 160 ns the discharge becomes rather non-uniform. Another feature observed is that by 80 ns the discharge stems from a single hot spot at the cathode and is confined to a reducingly small area towards the end of the pump pulse. Comparing Fig. 6.7(a) and 6.7(c) it can be seen that the discharges in Ne buffered gas mixtures are slightly less filamentary than the discharges in He buffered gas mixtures. Figure 6.7(d) is recorded with the addition of 0.53 mbar (400 mTorr) Xe to the Ne mixture, which homogenises the discharge substantially and preserves its homogeneity for about 200 ns.

The quantitative evolution of the discharge inhomogeneity, and of the discharge width in ArF laser gas mixtures is extracted from a large number of discharge images recorded versus an increasing delay time with respect to the initiation of the discharge. The temporal evolution of both measures is shown for various amounts of Xe in Fig. 6.8(a) and 6.8(b) respectively.

From Fig. 6.8(a) it can be seen that the rate of increase of the discharge inhomogeneity

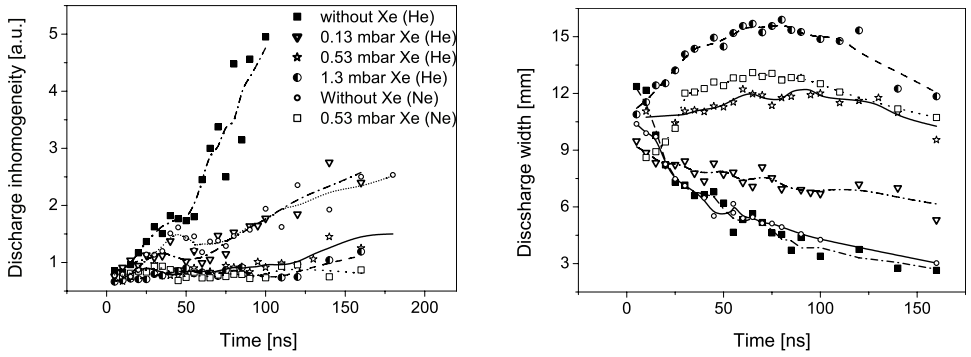


(a) (b)

*Figure 6.8: Temporal behavior of (a) discharge inhomogeneity and (b) discharge width in base gas mixtures of 2 bar He (or Ne)/60 mbar Ar/1.5 mbar $F_2$ and with increasing amount of Xe added to it. The symbols used to denote different gas mixtures in (b) are the same as in (a).*

for He buffered mixtures drops strongly when Xe is added up to a partial pressure of 1.3 mbar. A similar behaviour is observed when 0.53 mbar Xe is added to a Ne buffered mixture. From the images in Fig. 6.7(a) and 6.7(c), it was seen that the discharge in a gas mixture without Xe constricts strongly during the pump pulse. The homogeneous glow is rapidly replaced by filaments which conduct an increasing part of the discharge current through a smaller area. Figure 6.8(b) shows that the discharge width in a He (and Ne) buffered mixture without Xe decreases rapidly. With the addition of 0.13 mbar Xe, the constriction is observed to proceed slower because the filamentation of the discharge is reduced. Yet, the temporal behaviour of the discharge width is governed by filamentation like in a mixture without Xe. However, when the Xe pressure is raised further to 0.53 mbar, the discharge width increases only slightly during the pump pulse. Only from 125 ns onwards, the discharge width becomes smaller as a result of increased filamentation. With the addition of Xe, the filamentation is postponed such that the normal glow behaviour of the discharge becomes apparent. In the normal glow, the discharge tends to increase the discharge area when the discharge current increases, such that the current density remains constant [34]. In this way, the cathode can support a larger current through the discharge, via secondary emission.

In Fig. 6.8(b), the curve for the He buffered mixture with 1.3 mbar Xe shows this explicitly. The discharge starts with about the same width as the preionised area. Up to 30 ns the discharge width increases rapidly, just like the discharge current (shown in Fig. 6.6(a)), thereby keeping the current density approximately constant. Up to 120 ns, the discharge width increases slower due to the slower rise of the current. After that the discharge width decreases, as a result from growing filamentation, to roughly its initial value by 160 ns. The width of the discharge in the He buffered gas mixture with 1.3 mbar Xe is much larger than the width in a mixture with 0.53 mbar Xe due to the higher current at which this discharge is operated (about 400 A compared to 530 A).

Figure 6.8(b) shows also the temporal behaviour of the width of a discharge in a Ne buffered mixture. It can be seen that discharge constricts rapidly due to growing filamentation of the discharge during the pump pulse. The addition of Xe to the Ne buffered gas mixture postpones, similar to He buffered mixtures, the filamentation of the discharge. Up to 30 ns, we see here also that the discharge width grows rapidly with the rise of the current through the discharge, such that the current density at the cathode remains approximately constant. After 30 ns the discharge width increases much slower and starts decreasing at 80 ns. In how far the hot spot that shows up at the cathode influences the temporal behaviour of the discharge width after 30 ns is not yet clear.

It must be noted that addition of Xe to ArF laser gas mixtures will inevitably lead to the formation of XeF excimer molecules. The formation of XeF excimers in addition to ArF may be lead to a competition for the available $F_2$ molecules and thus a suppression of gain at ArF wavelength. Therefore, it is important to measure whether the optical gain from the ArF excimers would be reduced by the presence of XeF. In excimer laser gas mixtures, however, the population inversion causing the gain can be easily measured by observing the spontaneous emission from the upper laser level, because the lower laser level is essentially empty (no re-absorption of fluorescence) due to its ultrashort lifetime. In order to determine the possible depletion of ArF by generation of XeF excimers we decided to simultaneously monitor the spontaneous emission from both excimers, ArF at a wavelength of 193 nm and XeF at 351 nm, as described below. For this purpose, we used two photomultiplier tubes (Hamamatsu R331, Philips 56AVP) each equipped with the appropriate band pass filter to detect the spontaneous fluorescence from the ArF and XeF excimers that are formed during the discharge.

The spontaneous emission from ArF and XeF excimers was simultaneously monitored for increasing partial pressures of Xe in $He/Ar/F_2$ gas mixtures. Figure 6.9 shows

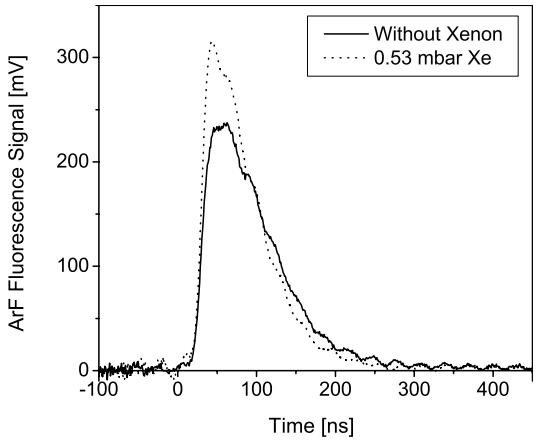


*Figure 6.9: Temporal behavior of ArF emission in 2 bar He/1.5 mbar $F_2$/60 mbar Ar without Xe and with 0.53 mbar Xe. The power density and the current density were about 1.3 MW $cm^{-3}$ and 340 A $cm^{-2}$.*

the temporally resolved spontaneous emission from ArF discharges in a base mixture, composed of 2 bar He, 60 mbar Ar and 1.5 mbar $F_2$, and in the same base mixture to which 0.53 mbar Xe is added. It can be seen that with the addition, the amplitude of the ArF signal increases by about 35 % while the pulse width (FWHM) reduces by about 20 % of the value of the discharges in Xe-free gas mixture.

It must be noted that the pulse energy of an excimer laser is proportional to the time integral of the inversion that is pumped by the discharge into the upper laser level. And this integral is proportional to the spontaneous emission integral. Therefore, it is interesting to measure the time integral of the spontaneous emission as it directly relates with the laser pulse energy that could be obtained form such discharges. Fig. 6.10 shows the integral of the fluorescence signals of ArF and XeF versus the partial pressure of Xe for the base gas mixtures of 2 bar He, 60 mbar Ar and 1.5 mbar $F_2$. It can be seen that the ArF spontaneous emission remains nearly constant while the spontaneous emission from XeF excimer increases with increasing Xe pressure. This finding is highly important. It means that adding Xe (for stabilizing the discharge and thereby extending its homogeneous duration significantly) does not come with any significant penalty, particularly, no reduction of the gain is expected when adding Xe in an in ArF laser. One might have expected that perhaps beyond a certain Xe

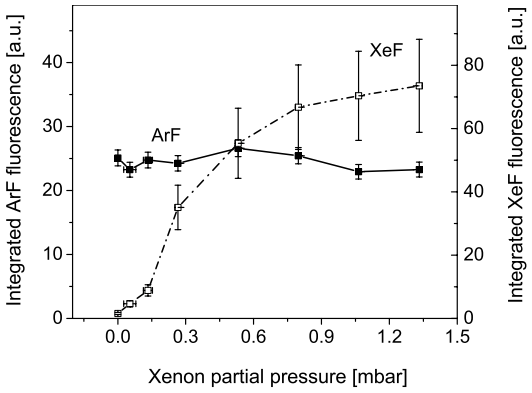


*Figure 6.10: Temporally integrated spontaneous emission signals of ArF and XeF excimers versus the Xe partial pressure that is added to the laser gas mixture. The base gas mixture is composed of 2 bar He, 60 mbar Ar and 1.5 mbar $F_2$. The pump power density and the current density amounts to 1.3 MW $cm^{-3}$ and 340 A $cm^{-2}$ respectively.*

partial pressure the formation of ArF would have become noticeably suppressed which should have shown as a decrease of the fluorescence. However, this limit was obviously not reached with the Xe pressures that we used.

To investigate if an improvement in discharge homogeneity can be achieved also with the addition of a different heavy rare gas, we added Kr to the gas mixture. We found that the addition of Kr, up to partial pressures of 1.3 mbar does not have a noticeable effect on the discharge uniformity in ArF excimer laser gas mixtures.

The important conclusion from these investigations on the discharge homogeneity is that Xenon addition is a powerful tool to produce stable long pulse glow discharges in ArF laser gas mixtures that works without perturbing or slowing the formation of ArF excimer molecules and thus promises to preserve the full pulse energy of the laser.

After having presented our observations that the addition of Xe has a strong stabilizing effect of $F_2$-based excimer gas discharges, the question arises on what is the underlying physical origin of this stabilization. For this, we refer to previous works of other researchers and test their conclusions directly with our own measurements.

The effect of the addition of Xe to ArF laser gas mixtures was previously investigated only in short pulse lasers, by Kataoka et al. [128] and Hofmann et al. [129]. Kataoka et al. [128] have shown that the addition of a very small amount of Xenon (at ppm level) to the laser gas mixture improves the discharge quality, and with that raises the output energy of an ArF laser excited with 30 ns long pump pulses. Tests performed by Hofmann et al. [129] have shown a substantial increase in the pulse to pulse stability of the output energy after the addition of about 6 - 10 ppm of Xe to the laser gas. Both, Kataoka as well as Hofman et al. suggest that the improvement in discharge quality, which leads to a better laser performance, results from an increase of the preionisation density due to the higher ionization cross section of Xe compared with the other gases present.

In contrast, we exclude this mechanism, as being much too weak in our experiments, with the following arguments and measurements of the preionisation density. As is described in detail in Sec. 3.2.1, we showed that the preionisation electron density produced by the x-ray source is well sufficient to initiate a streamer-free glow discharge in a $He/F_2$ mixtures, such that any additional preionisation can not contribute much to a further improvement of the uniformity of the discharge. Second, we expect that the rise of the preionisation electron density resulting from the addition of a small amount Xe is rather negligibly small and therefore cannot have any influence on the discharge quality. We come to this conclusion by measuring the relative contribution of each of the gas constituents of a He/Ar/Xe mixture to the preionisation electron density (the measurement method is described in Sec. 3.2.1).

In a first step, the preionisation electron density was measured in 2 bar He, and a mixture of 2 bar He and 60 mbar Ar. From the results summarized in Table 6.1 it can be seen that the addition of 60 mbar Ar raises the preionisation electron density from $2.4\text{x}10^7$ to $3.5\text{x}10^7$ $cm^{-3}$, which amounts to an increase of $1.1\text{x}10^7$ $cm^{-3}$. The same increase in electron density is found when 60 mbar Ar is added to Ne, as is shown in Table 6.1 as well. In the next step, the contribution of Xe to the preionisation electron density was measured by adding an increasing amount of Xe (1 mbar to 20 mbar) to 2 bar He and to a gas mixture of 2 bar He and 60 mbar Ar. Using the values for the contribution of He and the He/Ar mixture given in Table 6.1, the relative contribution for various partial pressures of Xe is calculated. From this, the gain in preionisation electron density obtained by addition of Xe is determined as shown in Fig. 6.11. It can be seen that, indeed, the preionisation electron density scales proportional to the Xe partial pressure, however, this amounts to only a rather small value of about $1.6\text{x}10^6$ $cm^{-3}$ $mbar^{-1}$. With this value, and taking the low Xe pressure that led to a strong improvement of discharge quality and duration in our experiments, 0.53 mbar Xe, we obtain in a relative contribution in the preionisation electron density of about

| Gas | Preionisation electron density $n_e$ [$10^7$ cm$^{-3}$ ] |
|---|---|
| 2 bar He | 2.4 |
| 2 bar He/60 mbar Ar | 3.5 |
| 2 bar Ne | 3.6 |
| 2 bar Ne/60 mbar Ar | 4.8 |

*Table 6.1: Measured preionisation electron densities for various gas mixtures.*

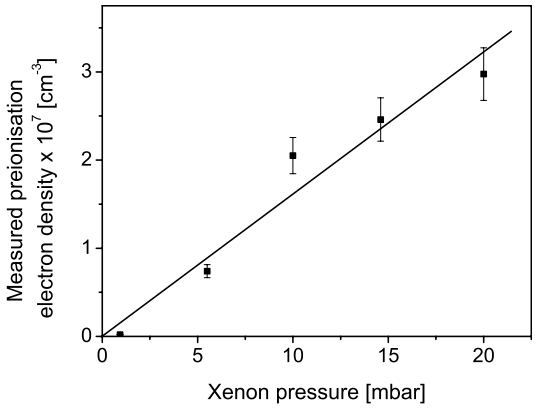


*Figure 6.11: Measured preionisation electron density versus Xenon partial pressure. The measurements were done using the electric scheme presented in Fig. 3.15*

3 % and 2 % for 2 bar He and for a mixture of 2 bar He/60 mbar Ar, respectively. This contribution is so small that it can be safely considered negligible. We can thus conclude that the Xe-induced homogenisation of the discharge is not linked to the increase in the preionisation electron density as was claimed in [128] and [129].

A possible reason for the improved homogeneity of the discharge with the addition of the Xe can be a kinetic effect which lowers the electron temperature occurring in the bulk of the discharge resulting in suppressing the filamentation. In order to clarify this, some spectroscopic investigations has to be carried out which specifically looks for the reaction channels of Xe in $F_2$ and ArF laser gas mixtures. Another possible experiment is to induce an electron density perturbations with the instantaneous ionisation of gas by a femtosecond laser in the bulk of the discharge and monitor how

this perturbation evolves in time. However, these investigations were out of the scope of this thesis.

## 6.3 Conclusions

The influence of the buffer gas on the discharge homogeneity of $F_2$-based excimer laser gas mixtures was studied. It was found and quantified that discharges in Neon buffered gas mixtures are more stable. More importantly, however, the influence of small amounts of rare gases on the discharge uniformity was investigated in long-pulse discharges for the first time. It was found that the addition of up to 1.3 mbar Xenon to $F_2$-based excimer laser gas mixtures significantly improves the uniformity of the long pulse discharge. Moreover, it was found that Xe-addition enables the extension of the stable phase of the discharge up to 200 ns. Simultaneous monitoring of the fluorescence of ArF (193 nm) and XeF (351 nm) excimers revealed that the addition of Xenon does not negatively affect the desired formation of ArF excimer molecules, and that the pulse energy of $F_2$-based excimer lasers would be as high as without the Xe-stabilization. The addition of Xe to $F_2$-based excimer laser gas mixtures therefore bears a large potential to realize a novel class of high-beam-quality excimer lasers based on long-pulse homogeneous and stable discharges in $F_2$ and ArF laser gas mixtures.

# Summary

Fluorine based excimer lasers such as KrF, ArF and $F_2$ are currently the most powerful sources available in the ultraviolet wavelength range, operating at 248 nm, at 193 nm and at 157 nm, respectively. They are thus of central importance for numerous applications in this range. At these short wavelengths, reaching the laser threshold for an efficient operation, $F_2$-based lasers require to be pumped, in a controlled manner, with very high power densities. This can practically be achieved only via pulsed, transversal glow discharges in high-pressure gas mixtures containing at least Fluorine, Krypton and Argon. However, such discharges are rather difficult to control because internal mechanisms, which are often not fully understood, let such discharges become instable with time. This manifests itself in a so-called filamentation of the discharge, i.e., the formation of thin channels of enhanced current. Eventually, an initially homogeneous discharge will turn into an arc that bridges the electrode gap. Such filamentation or arcing deteriorates the optical homogeneity of the gain medium, resulting in a termination of the laser pulse before the end of the current pump pulse, thereby limiting the maximum laser pulse duration to 20 - 30 ns. As a consequence, the resonator-internal light becomes amplified only through a smaller number of round trips rendering an output radiation consisting mostly of amplified spontaneous emission with a poor spatial coherence. This is a significant disadvantage because in many industrial applications of excimer lasers it is desired to have a diffraction-limited, high-quality laser beam. For instance, in material processing, a high beam quality allows structuring and drilling at high resolution. The desired high beam quality can be obtained only when the gain in the discharge is present and also remains spatially homogeneous for an extended time interval, such as several hundreds of nanoseconds, allowing the resonator-internal light to perform a sufficient number of round trips and thereby suppress amplified spontaneous emission. Realizing a stable, homogeneous discharge for up to hundreds of nanoseconds by elimination or suppression of discharge instabilities is therefore a key issue for providing high spatial quality

and powerful UV laser radiation.

The objective of this thesis is to identify the mechanisms that lead to discharge instabilities in $F_2$-based excimer laser gas discharges and, also, to eliminate or suppress the growth of discharge instabilities with suitable measures.

For reaching these goals the onset and development of filamentation in discharges in $F_2$-based excimer laser gas mixtures is investigated under well controlled conditions with regard to the excitation and observation of the discharges. To enable the latter we developed a compact experimental set-up which, via a pulsed, strong and properly timed x-ray preionisation, allows to initiate a homogeneous glow discharge in such gas mixtures. Further, to monitor the spatial and temporal evolution of the discharges with high temporal and spatial resolution, the discharge volume is given a particular flat shape and the fluorescence from the discharge is recorded with a fast, intensified CCD camera. In addition to this, we developed a novel method of characterising the spatio-temporal development of discharges, which is based on a numerical processing of the spatio-temporally resolved fluorescence images. This approach enables for the first time to clearly identify and also quantify systematic dependencies of filamentation and changes in the size of the discharge as a function of a number of experimental parameters. These are the preionisation density, the pressure, the electrode material and surface roughness.

Our experiments show that a preionisation electron density of about 1 x $10^7$ $cm^{-3}$ $bar^{-1}$ is sufficient to initiate a streamer-free homogeneous glow discharge in $He/F_2$ gas mixtures. We found that the homogeneous initiation of the glow discharges strongly depends on the time delay between the application of the preionisation pulse and the discharge voltage. The optimum time delay was found to be about 20 ns.

From our experiments, it was found that the total pressure plays a changing role in the homogeneity of discharges, depending on the pressure range. As the total pressure was increased, the discharges in gas mixtures of Helium and 1 mbar $F_2$ became more inhomogeneous. But no significant growth of the inhomogeneity was seen when the pressure was varied from 2 bar to 3 bar.

The influence of various electrode materials on the homogeneity of discharges in $F_2$-based excimer laser gas mixtures has been investigated. The study includes Nickel, Chromium, and Gold-coated electrodes as well as bulk Copper, Aluminium, Brass and Stainless Steel electrodes. The quantitative characterization of discharge homogeneity and width versus time based on image processing reveals that amongst the electrode materials studied, Nickel-coated Aluminium electrodes provide the most homogeneous discharges.

The effect of surface roughness of the electrodes on the discharge uniformity is investigated using bulk Copper electrodes. However, our experimental results show that the surface roughness does not have a significant influence on the homogeneity of discharges in $F_2$-doped excimer laser gas discharges.

The experimental evidences presented in this thesis show a rather unexpected effect, namely, that discharges in $He/F_2$ gas mixtures are not stable, which is in contradiction with both previous observations and models. Instead, the spatio-temporal images reveals that even under optimised start up conditions, such discharges become inhomogeneous and develop an increasing number of filaments with growing intensity. Based on the novel tool developed, which quantifies the speed and strength of instability growth in discharges, we present for the first time, a quantitative comparison with theory. From the comparison, we conclude that the filament formation in $He/Kr/F_2$ and $He/Ar/F_2$ excimer laser gas mixtures is associated mainly with the presence of $F_2$ and not with the Kr or Ar concentration, as was previously suggested. Instead, we find that the reason leading to instabilities in $F_2$-based discharges is a local depletion of the halogen concentration as was proposed by Coutts and Webb. These conclusions also indicate that corresponding lasers can be designed for a higher beam quality by optimising the electron density and the Fluorine density.

In an effort to find ways to extend the homogeneous part of the discharge, the influence of the buffer gas on the discharge homogeneity of $F_2$-based excimer laser gas mixtures was studied and it is found and quantified that discharges in Neon buffered gas mixtures are more stable. In addition, in search for a temporal extension of the discharge homogeneity, the influence of small amounts of rare gases on the discharge uniformity was investigated in long-pulse discharges for the first time. With these investigations, we prove a novel concept of stabilisation by observing that the addition of up to 1.3 mbar Xenon to $F_2$-based excimer laser gas mixtures significantly improves the uniformity of the long pulse discharge. In addition the Xenon admixture enabled the extension of the stable phase of the discharge up to 200 ns, so far only limited by the current driving circuit. Simultaneous monitoring of the fluorescence of ArF (193 nm) and XeF (351 nm) excimers revealed that this addition of Xenon does not reduce the desired formation of ArF excimer molecules, such that the pulse energy of $F_2$-based excimer lasers would be as high as without the Xe stabilization.

The latter method to temporally extend a homogeneous discharge in $F_2$-based excimer laser gas mixtures with relatively easy means bears a large potential for an immediate application, which is to realize a novel class of powerful and high-beam-quality ultraviolet excimer lasers via Xe-stabilized discharges in $F_2$ and ArF gas mixtures.

# Samenvatting

De krachtigste lichtbronnen die momenteel beschikbaar zijn in het ultraviolette gedeelte van het spectrum zijn excimeer lasers gebaseerd op met fluor gedoteerde laser gasmengsels. Met hun respectievelijke golflengtes van 248 nm, 193 nm en 157 nm zijn de KrF, ArF en $F_2$ laser voorbeelden van deze klasse lasers. Juist door de korte golflengtes zijn deze lichtbronnen van eminent belang voor talrijke toepassingen. Omdat deze lasers fotonen uitzenden met een hoge energie is het noodzakelijk om deze klasse lasers te pompen met zeer hoge vermogensdichtheden. In de praktijk kan dit pompen slechts in een gepulseerde vorm namelijk door middel van een transversale elektrische ontlading in hogedruk laser gasmengsels die tenminste fluor en een of meerdere edelgassen bevatten. Teneinde een homogene energie depositie te bewerkstelligen moet deze gasontlading ruimtelijk homogeen zijn. Homogeen gestarte ontladingen worden meestal echter na zeer korte tijd instabiel of filamenteus van aard, hetgeen zich manifesteert in de vorming van dunne kanalen of filamenten in de ontlading met daarin een verhoogde stroomdichtheid. Uiteindelijk zal een van oorsprong homogene ontlading overgaan in een vonk die de anode en kathode kortsluit. Het aanvankelijk gevormde homogene versterkingsmedium wordt hierdoor verstoord en dit leidt uiteindelijk tot beindiging van optische laserpuls na 20 - 30 nanoseconden, ver voordat de pomppuls is beindigd. Het gevolg is dat het geproduceerde laserlicht slechts een beperkt aantal rondgangen in de laser resonator kan maken en dat dus het uitkomende laserlicht lijkt op spontaan versterkte emissie met een matige ruimtelijke coherentie. In vele industrile toepassingen van dit type lasers vormt dit een groot probleem omdat vaak een door diffractie gelimiteerde laserbundelkwaliteit vereist is. Het bewerken van materialen kan bijvoorbeeld alleen met de verwachtte hoge resolutie uitgevoerd worden als de laserbundel diffractie gelimiteerd of met andere woorden van een hoge kwaliteit is. De gewenste hoge bundelkwaliteit kan slechts verkregen worden als de ontlading gedurende een langere tijd homogeen blijft. Vereist is tenminste een tijdsduur van enkele honderden nanoseconden waardoor het licht een voldoend aan-

tal rondgangen in de resonator kan maken zodat er alleen resonatormodi met weinig verliezen overblijven. Daarom is het maken van een stabiele homogene gasontlading van enkele honderden nanoseconden de belangrijkste voorwaarde voor het maken van krachtige (V)UV laserpulsen met een goede bundelkwaliteit.

Het in dit proefschrift beschreven onderzoek beschrijft hoe instabiliteiten of filamenten in op $F_2$ gebaseerde laser gasmengsels ontstaan in de ontlading en hoe deze voorkomen of onderdrukt kunnen worden. Daarvoor werd het opstarten en de verdere ontwikkeling in de tijd van dit soort ontladingen bestudeerd onder goed gecontroleerde omstandigheden. Er werd daartoe een compacte ontladingscel ontwikkeld waarin het mogelijk was om een homogene gepulseerde ontlading, na het aanbrengen van voldoende voorionisatie met behulp van een sterke Rntgen bron, op te starten en te laten voortduren. De ontwikkeling van de ontlading in ruimte en tijd werd gemeten door een snelle en van een versterker voorziene CCD camera die bovendien gedurende tijden korter dan 1 nanoseconde aangezet kan worden. Voor een goede analyse van de optredende instabiliteiten in de verschillende ontladingen werd een nieuwe methode voor het karakteriseren van de ruimte-tijd ontwikkeling van de ontlading ontwikkeld. Hiermee kunnen we voor het eerst ook kwantitatief systematische afhankelijkheden in de ontladingsfilamenten en veranderingen in de afmetingen van de ontlading als functie van verschillende experimentele parameters zoals voorionisatiedichtheid, gas samenstelling en elektrode materiaal zichtbaar maken.

Onze experimenten laten zien dat een voorionisatie dichtheid van ongeveer $1\text{x}10^7$ $\text{cm}^{-3}$ $\text{bar}^{-1}$ voldoende hoog is om in een $He/F_2$ lasergas mengsel een elektrische ontlading homogeen te laten starten mits de tijd tussen het aanschakelen van de ionisatie puls en de hoogspanningspuls goed gekozen is. Uit onze studies is gebleken dat hiertussen ongeveer 20 nanoseconden moet zitten.

Tijdens de experimenten werden verschillende elektrode materialen zoals koper, aluminium, brons en roestvrij staal alsmede aluminium elektrodes gecoat met nikkel, chroom en goud, gebruikt. De invloed van deze materialen op de ontladingshomogeniteit van $F_2$ gebaseerde lasergas mengsels werd onderzocht. Uit dit onderzoek bleek dat met nikkel bedekte aluminium elektrodes de meest homogene ontladingen opleverden. Met elektroden gemaakt van koper werd de invloed van de oppervlakte ruwheid op de ontladingshomogeniteit onderzocht. Uit deze experimenten bleek dat de oppervlakteruwheid van de elektrodes geen belangrijke factor is voor de ontladingshomogeniteit van fluor gedoteerde laser gas mengsels.

De experimentele resultaten die in dit proefschrift gepresenteerd worden laten een onverwacht effect zien namelijk dat gasontladingen in $He/F_2$ lasergas mengsels in de loop van de tijd instabiliteiten ontwikkelen. Dit is in tegenspraak met eerdere exper-

imentele resultaten en ook met theoretische modellen. Foto's van ontladingen die het gedrag in tijd en plaats weergeven, tonen dat zelfs ontladingen die onder optimale condities opgestart zijn, in de loop van de tijd en afhankelijk van de gassamenstelling, toch een toenemend aantal filamenten ontwikkelen. De analyse van de resultaten met de eerder genoemde karakteriseringsmethode laat zien dat de vorming van filamenten in de ontlading sterk afhankelijk is van de hoeveelheid $F_2$ en nauwelijks van de hoeveelheid Ar of Kr in het lasergas zoals eerder werd gedacht. We zien verder dat de ontladings instabiliteiten in fluor gedoteerde lasergas mengsels het gevolg is van een zeer plaatselijke afname van de halogeen concentratie in het gasmengsel zoals reeds in de tachtiger jaren door Couts en Webb voorgesteld werd. Onze conclusies laten zien dat dit soort lasers met een goede bundel kwaliteit ontworpen kunnen worden door een juiste keuze van de elektronen dichtheid en van de fluor concentratie.

De invloed van het buffergas op de duur van de homogene ontlading in op fluor gebaseerde lasergas mengsels werd onderzocht. Er werd gevonden dat ontladingen met neon als buffergas stabieler waren dan ontladingen met helium of argon als buffergas. Teneinde een verlenging van duur van het homogene gedeelte van de ontlading te bewerkstelligen werd ook het toevoegen van zeer kleine hoeveelheden van andere gassen aan de bekende lasergas mengsels onderzocht. Hieruit bleek dat door toevoeging van een zeer kleine hoeveelheid xenon de homogeniteit van de ontlading sterk verbeterd kan worden en dat de duur van het homogene gedeelte van een ontlading zeer substantieel verlengd kan worden. Door toevoeging van bijvoorbeeld 1,3 mbar xenon aan een op fluor gebaseerd lasergas mengsel kon de stabiele fase van de ontlading verlengd worden tot 200 nanoseconden, begrensd door het elektrisch circuit. Uit de analyse van de uitgezonden spontane emissie signalen van de twee gevormde excimeren ArF (193 nm) en XeF (351 nm) kunnen we concluderen dat er geen meetbare teruggang in de vorming van ArF excimeer molekulen optreedt bij toevoeging van deze kleine hoeveelheid Xe aan het lasergas mengsel en dus zal deze nieuwe stabilisatietechniek ook geen nadelige gevolgen hebben voor de totale pulsenergie van de ArF laser. De nieuwe stabilisatietechniek, waarvoor patent is aangevraagd, is een zeer eenvoudige en direct toepasbare methode die kan leiden tot een nieuwe generatie van krachtige UV excimeer lasers gebaseerd op met fluor gedoteerde lasergas mengsels en met een lange optische puls met goede bundel kwaliteit.

# References


[1] F.G. Houtermans. Über maser-wirkung im optischen spektralgebiet und die möglichkeit absolut negativer absorption für einige fälle von molekülspektren (licht-lawine). *Helv. Phys. Acta*, 33:933–940, 1960. (In German).

[2] N.G. Basov, V.A. Danilychev, and Y.M. Popov. Stimulated emission in the vacuum ultraviolet region. *Sov. J. Quantum Electron.*, 1(1):18–22, 1971. [Kvantovaya Elektron. **1** (1), 29-34 (1971)].

[3] Ch.A. Brau. *Rare gas halogen excimers.* In Ch.K. Rhodes, editor, *Excimer lasers*, Topics in Applied Physics **30**, chapter 4, pages 87–137. Springer Verlag, Berlin, 2nd enlarged edition, 1984.

[4] R.W. Waynant. A discharge-pumped ArCl superfluorescent laser at 175 nm. *Appl. Phys. Lett.*, 30(5):234–235, 1977.

[5] R.W. Waynant. Inert-gas halide vuv lasers. *Sov. J. Quantum Electron.*, 8(8):1002–1004, 1978. [Kvantovaya Elektron. **5**, 1767-1770 (1978)].

[6] J. T. Verdeyen. *Laser electronics.* Prentice Hall, New Jersey, 2nd edition, 1989.

[7] M. Ohwa and M. Obara. Theoretical evaluation of the buffer gas effects for a self-sustained discharge ArF laser. *J. Appl. Phys.*, 63(5):1306–1312, 1988.

[8] H.H. Michels, R.H. Hobbs, and L.A. Wright. The electronic structure of ArF and $Ar_2F$. *Chem. Phys. Lett.*, 48(1):158–161, 1977.

[9] S. K. Searles and G. A. Hart. Stimulated emission at 281.8 nm from $XeBr^*$. *App. Phys. Lett.*, 27(4):243–245, 1975.

[10] J. J. Ewing and C. A. Brau. 354 nm laser action on $XeF^*$. *App. Phys. Lett.*, 27(8):435–437, 1975.

[11] M. L. Bhaumik, R. S. Bradford, Jr., and E. K. Ault. High-efficiency $KrF^*$ laser. *App. Phys. Lett.*, 28(1):23–24, 1976.

[12] H. J. J. Seguin, J. Tulip, and D. McKen. UV photoionisation density measurements in TEA lasers. *App. Phys. Lett.*, 23(6):344–346, 1974.

[13] R. Burnham, F. X. Powell, and N. Djeu. Efficient electric discharge lasers in XeF and KrF. *App. Phys. Lett.*, 29(1):30–32, 1976.

[14] L. E. Kline and L. J. Denes. Investigations of glow discharge formation with volume preionisation. *J. Appl. Phys.*, 46(4):1567–1574, 1975.

[15] R. P. Akins, G. I., and S. C. Lin. Optimal timing and power enhancement observed in a double-pulse fast-discharge-driven XeF laser. *J. Appl. Phys.*, 49(4):2262–2264, 1978.

[16] R. C. Sze and P. B. Scott. 1/4-J discharge pumped KrF laser. *J. Appl. Phys.*, 49(6):772–774, 1978.

[17] N. W. Harris, F. O'Neill, and W. T. Whitney. Operation of a 15-atm electron-beam-controlled $CO_2$ laser. *App. Phys. Lett.*, 25(3):148–151, 1974.

[18] J. A. Mangano and J. H. Jacob. Electron-beam-controlled discharge pumping of the KrF laser. *App. Phys. Lett.*, 27(9):495–498, 1975.

[19] J. A. Mangano, J. H. Jacob, and J. B. Dodge. Electron-beam-controlled discharge pumping of the XeF laser. *App. Phys. Lett.*, 29(7):426–428, 1976.

[20] R. C. Sze. Rare gas halide avalanche discharge lasers. *IEEE J. Q. Elec.*, 15:61338, 1979.

[21] R. Bruzzese, D. C. Hogan, and C. E. Webb. Discharge stability of electrically excited rare gas halide laser systems. *Nuovo Cimento*, 81:21, 1984.

[22] R. A. Haas. *Chapter 14 in Applied Atomic Collision Physics*. Academic Press, New York, 3rd edition, 1982.

[23] J. D. Daugherty, J. A. Mangano, and J. H. Jacob. Attachment dominated electron-beam-ionised discharges. *Appl. Phys. Lett.*, 28.

[24] H. M. J. Bastiaens. *On the long pulse operation of the molecular fluorine laser*. PhD thesis, University of Twente, Enschede, The Netherlands, 2000.

[25] D. C. Hogan, R. Bruzzese, A. J. Kearsley, and C. E. Webb. Long pulse operation of discharge excited XeCl* laser. *J. Phys. D*, 14:L157–L161, 1981.

[26] M. Kakehata, E. Hashimoto, F. Kannari, and M. Obara. High specific output energy extraction of a vacuum ultraviolet molecular fluorine laser excited at 66 $MW/cm^3$ by an electric discharge. *Appl. Phys. Lett.*, 56(26):2599, 1990.

[27] I. A. Mclntyre and C. K. Rhodes. High power ultra-fast excimer lasers. *J. Appl. Phys.*, 69(1):R1, 1991.

[28] Yu. Bychkov, M. Makarov, A. Suslov, and A. Yastremsky. A 10-J electric discharge-pumped phototriggered XeCl laser. *Rev. Sci. Instrum.*, 65(1):28–33, 1994.

[29] F. A. van Goor, M. Trentelman, J. C. M. Timmermans, and W. J. Witteman. Improved x-ray switched XeCl laser. *J. Appl. Phys.*, 75(1):621–623, 1994.

[30] T. Kitamura, Y. Arita, K. Maeda, M. Takasaki, K. Nakamura, Y. Fujiwara, and S. Horiguchi. Small-signal gain measurements in a discharge-pumped $F_2$ laser. *J. Appl. Phys.*, 81:2523, 1997.

[31] M. Makarov, J. Bonnet, and D. Pigache. High efficiency discharge-pumped XeCl laser. *Appl. Phys. B*, 66:417–426, 1998.

[32] J.C.M. Timmermans. *Double discharge XeCl laser.* PhD thesis, University of Twente, Enschede, The Netherlands, 1995.

[33] M. Trentelman. *Gas discharge excited XeF laser.* PhD thesis, University of Twente, Enschede, The Netherlands, 1993.

[34] Y. P. Raizer. *Gas discharge physics.* Springer-Verlag, — edition, 1991.

[35] A. Garscadden, M.J. Kushner, and J.G. Eden. Plasma physics issues in gas discharge laser development. *IEEE Tr. Plasma Sci.*, 19(6):1013–1031, 1991.

[36] M. Klines and J. Denes. *Applied atomic collision physics, Gas lasers.* Academic Press, New York, 3rd edition, 1982.

[37] R. C. Sze and T. R. Loree. Experimental studies of a KrF and ArF discharge laser. *IEEE J. Q. Elec.*, 14(12):944, 1978.

[38] J. I. Levatter and R. S. Bradfors Jr. Water dielectric blumelein driven fast electric discharge KrF laser. *Appl. Phys. Lett.*, 33(8):742, 1978.

[39] C. P. Wang. High repetition rate transverse flow XeF laser. *Appl. Phys. Lett.*, 32(6):360, 1978.

[40] R. S. Taylor, W. J. Sarjeant, A. J. Alock, and K. E. Leopold. Glow discharge characteristics of a 0.8 J multi-atmospheric rare gas halide laser. *Opt. Commun.*, 25(2):231, 1978.

[41] W. Bötticher, H. Luck, St. Niesner, and A. Schwabedissen. Small volume coaxial discharge as precsision testbed for 0D-models of XeCl lasers. *Appl. Phys. B*, 54(4):295, 1992.

[42] W. H. Long, Jr. M. J. Plummer, and E. A. Stappaerts. Efficient discharge pumping of an XeCl laser using a high-voltage pre-pulse. *Appl. Phys. Lett.*, 43(8):735, 1983.

[43] C. H. Fisher, M. J. Kushner, T. E. DeHart, J. P. McDaniel, R. A. Petr, and J. J. Ewing. High-efficiency XeCl laser with spiker and magnetic isolation. *Appl. Phys. Lett.*, 48(23):1574, 1986.

[44] R. S. Taylor and K. E. Leopold. Magnetically induced pulser laser excitation. *Appl. Phys. Lett.*, 46(4):335, 1985.

[45] J. W. Gerritsen, A. L. Keet, and W. J. Witteman. High-efficiency operation of a gas discharge XeCl laser using a magnetically induced resonant voltage overshoot circuit. *J. Appl. Phys.*, 67(7):3517, 1990.

[46] J. C. M. Timmermans, F. A. van Goor, and W. J. Witteman. A new mode to excite a gas-discharge XeCl laser. *Appl. Phys. B*, 57(6), 1993.

[47] M. Trenetleman, P. J. M. Peters, Qi-Chu Mei, and W. J. Witteman. Gas discharge XeF (B $\rightarrow$ X) laser excited by a prepulse-main-pulse circuit with magnetic swtiching. *J. Opt. Soc. Am. B*, 12(12):2494, 1995.

[48] L. Feenstra, O.B. Hoekstra, P.J.M. Peters, and W.J. Witteman. On the performance of an ArF and a KrF laser as a function of the preionisation timing and the excitation mode. *Appl. Phys. B*, 70(2):231–235, 2000.

[49] T. J. McKee, S. D. Hastie, and R. W. Weeks. Performance of a novel injection-locked excimer laser. *J. Appl. Phys.*, 56(7):2170–2173, 1984.

[50] S. Bollanti, P. di Lazzaro, F. Flora, G. Giordano, T. Letardi, G.Schina, and C.E. Zheng. Parametric study of an x-ray preionizer with plasma cathode. *Rev. Sci. Instrum.*, 65(2):315–322, 1994.

[51] V. V. Borovkov, V. V. Voronin, S. L. Voronov, D. I. Zenkov, B. V. Lazhintsev, V. A. Nor-Arevyan, V. A. Tananakin, G. I. Fedorov, and I. M. Yutkin. Three-electrode discharge laser with a middle control electrode. *Quantum Electron.*, 25(5):414–415, 1995.

[52] L. Feenstra. *On the long pulse operation of a discharge pumped ArF laser*. PhD thesis, University of Twente, Enschede, The Netherlands, 1999.

[53] P. J. Chantry. *Applied Atomic Collision Physics*. Academic Press, New York, 3rd edition, 1982.

[54] M. Rokni, J.H. Jacob, J.A. Mangano, and R. Brochu. Formation and quenching kinetics of $ArF^*$. *Appl. Phys. Lett.*, 31(2):79–82, 1977.

[55] A. M. Boĭchenko, V. I. Derzhiev, A. G. Zhidkov, and S. I. Yakovlenko. Kinetic model of an ArF laser. *Sov. J. Quantum Electron.*, 22(5):444–448, 1992. [Kvantovaya Elektron. **19**, 486-491 (1992)].

[56] S. Nagai, H. Furuhashi, Y. Uchida, J. Yamada, A. Kono, and T. Goto. Formation dynamics of excited atoms in an ArF laser using He and Ne buffer gases. *J. Appl. Phys.*, 77(7):2906–2911, 1995.

[57] D. Lo, A. I. Schedrin, and A. V. Ryabtsev. The upper energy limit of a self-sustained discharge pumped ArF laser. *J. Phys. D:Appl. Phys.*, 29(5):43–49, 1996.

[58] H. Akashi, Y. Sakai, and H. Tagashira. Modeling of a self-sustained discharge-excited ArF excimer laser. *J. Phys. D: Appl. Phys.*, 27:1097–1106, 1994.

[59] S. Nagai, H. Furuhashi, A. Kono, Y. Uchida, and T. Goto. Measurement of temporal behaviour of electron density in a discharge-pumped ArF excimer laser. *IEEE J. Quantum Electron.*, 34(8):942–948, 1998.

[60] J. G. Eden, R. W. Wayanat, S. K. Searles, and R. Burnham. New quenching rates applicable to the KrF laser. *Appl. Phys. Lett.*, 32(11):733, 1978.

[61] J. E. Velazco, J. H. Kolts, and D. W. Setser. Quenching rate constants for metastable Argon, Krypton, and Xenon atoms by fluorine containing molecules and branching ratios for XeF* and KrF* formation. *J. Chem. Phys.*, 65(9):3468, 1976.

[62] S. Watanabe and A. Endoh. Wide aperture self-sustained discharge KrF and XeCl lasers. *Appl. Phys. Lett.*, 41(9):799, 1982.

[63] A. E. Greene and C. A. Brau. Theoretical studies of UV-preionised transverse discharge KrF and ArF lasers. *IEEE J. Quantum Electron.*, 14(12):951, 1978.

[64] C. Wu, T. Kamiya, E. Hotta, and K. Kasuya. Development and application of KrF lasers with different excitation methods. *Fusion engineering and Design*, 44:365–370, 1999.

[65] A. M. Razhev, A. I. Shchedrin, A. V. Ryabstev, and A. A. Zhupikov. Effect of the pump intensity on the efficiency of a KrF excimer electric-discharge laser on a He-Kr-$F_2$ mixture. *Quantum electronics*, 34:901, 2004.

[66] M. Ohwa and M. Obara. Theoretical evaluation of high-efficiency operation of discharge-pumped vacuum ultraviolet $F_2$ lasers. *Appl. Phys. Lett.*, 51(13):958, 1987.

[67] H. M. J. Bastiaens, S. J. M. Peeters, X. Renard, P. J. M. Peters, and W. J. Witteman. Long pulse operation of an x-ray preionized molecular fluorine laser excited by a prepulse-mainpulse system with a magnetic switch. *Appl. Phys. Lett.*, 72(22):2791–2793, 1998.

[68] M. Kakehata, T. Uematsu, F. Kannari, and M. Obara. Efficiency characterisation of vacuum ultraviolet molecular fluorine ($F_2$) laser (157 nm) excited by an intense electric discharge. *IEEE J. Quantum Electron.*, 27(8):269–278, 1991.

[69] M. Takahashi, K. Maeda, T. Kitamura, M. Takasaki, and S. Horiguchi. Experimental study of formation kinetics in a discharge-pumped $F_2$ laser. *Optics Communications*, 116:269–278, 1995.

[70] M. von Dadelszen and D. E. Rothe. Coupled gas discharge and pulse circuit analysis. *IEEE. Trans. on Plasma Sci.*, 19(2).

[71] J. M. Meek. A theory of spark discharge. *Phys. Rev.*, 57:722, 1940.

[72] J. Koppitz. Nitrogen discharges of large cross section at high overvoltages in a homogeneous field. *J. Phys. D*, 6:1494, 1973.

[73] H. Seguin and J. Tulip. Photoinitiated and photosustained laser. *Appl. Phys. Lett.*, 21:414, 1972.

[74] A. J. Palmer. A physical model on the initiation of the atmospheric-pressure glow discharges. *Appl. Phys. Lett.*, 25(3):138–140, 1974.

[75] J. I. Levatter and S. C. Lin. Necessary conditions for the homogeneous formation of pulsed avalanche discharges at high gas pressures. *J. Appl. Phys.*, 51:210, 1980.

[76] G. Herziger, R. Wollermann-Windgasse, and K. H. Banse. On the homogeneization of transverse gas discharges by preionization. *Appl. Phys. A*, 24(3):267–272, 1981.

[77] S. Bollanti, T. Letardi, and C. E. Zheng. Effect of preionization on uniformity of photo-triggered XeCl laserdischarges: modeling and comparison with experimental results. *IEEE Trans. Plasma Sci.*, 19:361, 1991.

[78] R. S. Taylor. Preionisation and discharge stability study of long optical pulse duration uv preionised XeCl lasers. *Appl. Phys. B*, 41:1–24, 1986.

[79] J. I. Levatter, K. L. Robertson, and S. C. Lin. Long pulse behaviour of the avalanche/self sustained discharge pumped XeCl laser. *Appl. Phys. Lett.*, 39(4):297, 1981.

[80] M. R. Osborne and M. H. R. Hutchinson. Long pulse operation and premature termination of a high power discharge pumped XeCl laser. *J. Appl. Phys.*, 59(3):711, 1986.

[81] M. R. Osborne. Rare-gas-halide discharge stability. *Appl. Phys. B*, 45(4):285–291, 1988.

[82] R. Dreiskemper and W. Bötticher. Current filamentation of strongly preionised high pressure glow discharges in Ne/Xe/HCl mixtures. *IEEE Trans. Plasma Sci.*, 23:987, 1995.

[83] L. Friedland, J. H. Jacob, and J. A. Mangano. Volumetric stability of two-step ionisation dominated discharges. *J. Appl. Phys.*, 65.

[84] V. M. Borisov, V. P. Novikov, and O. B. Khristoforov. Instability of a uniform self-sustained discharge in excimer lasers. *High Temperature*, 24:1079, 1986.

[85] J. Coutts and C.E. Webb. Stability of transverse self sustained discharge excited long pulse XeCl lasers. *J. Appl. Phys.*, 59:704, 1986.

[86] J. Coutts. The halogen donor depletion instability - current pulse shape effects. *J. Phys. D*, 21:255, 1988.

[87] R. Bruzzese and D. C. Hogan. Analysis of temporal length limitations in XeCl lasers. *Nuovo Cimento*, 76 B:54, 1983.

[88] A. V. Dem'yanov, I. V. Kochetov, A. P. Napartovich, S. Longo, and M. Capitelli. Theoretical studies on microscopic and macroscopic non uniformities in electric-discharge-excited XeCl lasers. *Plasma Chem. and Plasma Process*, 16:121, 1996.

[89] M. J. Kushner. Microarcs as a termination mechanism of optical pulses in electric-discharge-excited KrF lasers. *IEEE Trans. Plasma Science*, 19:387–399, 1991.

[90] M.M. Turner. Relations between preionisation density distribution, electrode design, and efficiency in high-pressure discharge-excited gas lasers. *Appl. Phys. Lett.*, 63(21):2866–2868, 1993.

[91] G. J. Ernst. Compact uniform field electrode profiles. *Appl. Phys. B.*, 47(1):47, 1983.

[92] T. Y. Chang. Improved uniform field electrode profiles for TEA laser and high voltage applications. *Appl. Phys. B.*, 44(4):405, 1973.

[93] E.A. Stappaerts. A novel analytical design method for discharge laser electrode profiles. *Appl. Phys. Lett.*, 40(12):1018–1019, 1982.

[94] J. Timmermans. Double discharge XeCl laser. *PhD Thesis*, 1995.

[95] O. Uteza, Ph. Delaporte, B. Fontaine, B. Forestier, M. Sentis, and I. Tassy. Influence of cathode surface roughness on discharge homogeneity of a high-pulse repetition frequency long-pulse XeCl laser. *Appl. Phys.*, B 67:185–191, 1998.

[96] M. Makarov. Effect of electrode processes on the spatial uniformity of the XeCl laser discharge. *J. Phys. D: Appl. Phys.*, 28:1083, 1995.

[97] A. Belasri, J. P. Boeuf, and L. C. Pitchford. Cathode sheath formation in a discharge-sustained XeCl laser. *J. Appl. Phys.*, 74:1553, 1993.

[98] M. Bähr, W. Bötticher, and S. Choroba. The time-dependent development of the macroscopic instability of a XeCl laser. *IEEE Tr. Plasma Sci.*, 19(2):369, 1991.

[99] R. Dreiskemper, G. Schröder, and W. Bötticher. Light emission during cathode sheath formation in preionized high-pressure glow discharges. *IEEE Tr. Plasma Sci.*, 23(2):180–187, 1995.

[100] M. Makarov and Yu. Bychkov. The dynamics of XeCl discharge contraction. *J. Phys. D: Appl. Phys.*, 29:350–363, 1996.

[101] W. J. Sarjeant, A. J. Alcock, and K. E. Leopold. Parametric study of a constant E/N pumped high-power $KrF^*$ laser. *IEEE J. Quantum Electron.*, 14(3):177–184, 1978.

[102] Yu. I. Bychkov, I. N. Konovalov, and V. F. Tarasenko. Laser utilizing an Ar-Xe-$NF_3$ mixture with a discharge stabilised by a short-pulse electron beam. *Sov. J. Quantum Electron.*, 9(5):590, 1979.

[103] M. Richardson, A. Alcock, K. Leopold, and P. Burtyn. A 300-J multi gigawatt $CO_2$ laser. *IEEE J. Quantum electron.*, 9(2):236– 243, 1973.

[104] R. S. Taylor, P. Corkum, S. Watanabe, K. Leopold, and A. Alcock. Time-dependent gain and absorption in a 5 J UV preionised XeCl laser. *IEEE J. Quantum electron.*, 19(3):416 – 425, 1983.

[105] R. S. Taylor and K.E. Leopold. Transmission properties of spark preionisation radiation in rare-gas halide laser gas mixes. *IEEE J. Quantum electron.*, 31(12):2195 – 2207, 1995.

[106] A. K. Laflamme. Double discharge excitation for atmospheric pressure $CO_2$ lasers. *Rev.Sci.Instrum*, 41(11):1578–1581, 1970.

[107] R. S. Taylor, A. J. Alcock, and K. E. Leopold. Laser-induced preionisation of a rare-gas halide discharge. *Optics Letters*, 5(6):216–218, 1980.

[108] S. C. Lin and J. I. Levatter. X-ray preionization for electric discharge lasers. *App.Phys.Lett.*, 34(8):505–508, 1979.

[109] S. Sumida, M. Obara, and T. Fujioka. X-ray preionised high-pressure KrF laser. *Appl. Phys. Lett*, 33(11):913, 1978.

[110] H. Shields, A. J. Alcock, and R. S. Taylor. Preionisation kinetics of an x-ray preionised XeC1 gas discharge laser. *Appl. Phys. B.*, 31:27, 1983.

[111] M. Steyer and H. Voges. Parametric study of x-ray preionised high-pressure rare gas halide lasers. *Appl. Phys. B.*, 42:155, 1987.

[112] I. J. BIG10. Preionisation of pulsed gas lasers by radioactive source. *IEEE J. Quantum Electron.*, 14(2):75, 1978.

[113] T. Ganley, J. T. Verdeyen, and G. H. Miley. Enhancement of $CO_2$ laser power and efficiency by neutron irradiation. *Appl. Phys. Lett*, 18(12):568, 1971.

[114] M.M. Turner. Modeling the self-sustained discharge excited XeCl laser in two dimensions. *J. Appl. Phys.*, 71(5):2113, 1992.

[115] F. A. van Goor. Fast rise time x-ray preionisation source using a corona plasma cathode. *J. Phys. D. Appl. Phys.*, 26:404–409, 1993.

[116] S. J. Scott. Development of a long life, 2 khz repetition rate x-ray preionizer. *Appl. Phys. B.*, 56(4):201, 1993.

[117] S. J. Scott. Discharge from hot cao. *Phys. Rev.*, 32:492, 1911.

[118] I. Langmuir. The effect of space charge and residual gases on thermionic currents in high vacuum. *Phys. Rev.*, 2:450, 1913.

[119] S. J. M. Peeters. Een lange puls, gasontlading gepompte, moleculaire fluor laser. Master's thesis, University of Twente, Enschede, the Netherlands, 1996. (In Dutch).

[120] J.W. Gerritsen. *High-efficiency operation of an x-ray preionized avalanche discharge XeCl laser*. PhD thesis, University of Twente, Enschede, The Netherlands, 1989.

[121] S. M. Seltzer and J. H. Hubbel. Taken from http://physics.nist.gov. tables and graphs of photon mass attenuation coefficient and mass energy-absorption coefficients for photon energies 1 keV to 20 MeV for elements Z = 1 to 92 and some dosimetric materials, Appendix to invited plenary lecture by J.H. Hubbell, '45 years (1950-1995) with x-ray interactions and applications', presented at the 51st national meeting of the japanese society of radiological technology, April 14-16, 1995, Nagoya, Japan.

[122] K. J. Nygaard, J. F., Scott R. Hunter, and S. R. Foltyn. Electron attachment in dilute flourine-helium mixtures. *Appl. Phys. Lett.*, 32:351, 1978.

[123] K. Midorikawa, M. Obara, and T. Fujioka. X-ray preionization of rare-gas-halide lasers. *IEEE J. Quantum Electron.*, 20(3):198–205, 1984.

[124] R. C. Gonzalez and R. E. Woods. *Digital Image Processing*. Prentice Hall/Pearson Education International, 2002.

[125] K. J. Nygaard, J. F., S. R. Hunter, and S. R. Foltyn. Electron drift velocities in helium-fluorine gas mixtures. *Appl. Phys.*, 32:612, 1978.

[126] S. Watanabe, A. J. Alock, K. E. Leopold, and R. S. Taylor. Spatially resolved gain measurements in uv preionised homogeneous discharge XeCl and KrF lasers. *Appl. Phys. Lett.*, 38:3, 1981.

[127] H. B. Milloy and R. W. Crompton. Momentum-transfer cross section for electron-helium collisions in the range of 4-12 eV. *Phys. Rev. A*, 15:1847, 1977.

[128] N. Kataoka, M. Itagaki, K. Uchino, K. Muraoka, A. Takahashi, T. Okada, M. Maeda, T. Hori, K. Terashima, A. Suitani, T. Enami, and H. Mizoguchi. Performance improvement of a discharge pumped ArF excimer laser by xenon gas addition. *Jpn. J. Appl. Phys.*, 38:6735, 1999.

[129] T. Hofmann, T. Ishihara, P. P. Das, and A. I. Ershov. Narrow band excimer laser with gas additive, 2000. U.S. Patent, 6014398.

# List of publications

**Patent**

- D. Mathew, P. J. M. Peters, H. M. J. Bastiaens and K. J. Boller, *Stabilisation and temporal extension of stable glow discharges in fluorine based excimer laser gas mixtures by the addition of Xenon*, a patent application is submitted

**Journals**

- D. Mathew, H. M. J. Bastiaens, K. J. Boller and P. J. M. Peters, *Current filamentation in discharge-excited $F_2$-based excimer laser gas mixtures*, Appl. Phys. Lett, **88**, 101502, 2006
- D. Mathew, H. M. J. Bastiaens, K. J. Boller and P. J. M. Peters, *Effect of preionisation, fluorine concentration and current density on the discharge uniformity in $F_2$ excimer laser gas mixtures*, submitted to: J. Appl. Phys., December, 2006
- D. Mathew, H. M. J. Bastiaens, K. J. Boller and P. J. M. Peters, *Stabilisation and temporal extension of stable glow discharges in fluorine based excimer laser gas mixtures by the addition of Xenon*, submitted to Appl. Phys. Lett., March, 2007
- D. Mathew, H. M. J. Bastiaens, K. J. Boller and P. J. M. Peters, *Discharge instabilities in high pressure helium fluorine laser gas mixtures*, Proc. SPIE, **5777**, 589, 2005
- D. Mathew, H. M. J. Bastiaens, K. J. Boller and P. J. M. Peters, *Discharge instabilities in high pressure helium fluorine laser gas mixtures*, Proc. SPIE, **5958**, 59581A, 2005

- D. Mathew, H. M. J. Bastiaens, K. J. Boller and P. J. M. Peters, *Influence of electrode materials and surface roughness on the homogeneity of discharges in fluorine based excimer laser gas mixtures*, Proc. SPIE, 2006, in print

**International Conferences**

- D. Mathew, H. M. J. Bastiaens, K. J. Boller and P. J. M. Peters, *Discharge instabilities in high pressure helium fluorine laser gas mixtures*, Poster presentation, XV. International conference on gas flow and chemical lasers and high power laser conference, GCL/HPL, Prague, Czech Republic, 30 August 3 September, 2004
- D. Mathew, H. M. J. Bastiaens, K. J. Boller and P. J. M. Peters, *Discharge instabilities in high pressure helium fluorine laser gas mixtures*, Oral presentation, International Congress on Optics and Optoelectronics, Warsaw, Poland, 28 August - 2 September, 2005
- D. Mathew, H. M. J. Bastiaens, K. J. Boller and P. J. M. Peters, *Influence of electrode materials and surface roughness on the homogeneity of discharges in fluorine based excimer laser gas mixtures*, Oral presentation, XVI. International conference on gas flow and chemical lasers and high power laser conference, GCL/HPL, Gmunden, Austria, 4 - 8 September, 2006

**National Conferences**

- D. Mathew, H. M. J. Bastiaens, K. J. Boller and P. J. M. Peters, *Study on discharge instabilities in high pressure He/$F_2$ gas mixtures*, Poster presentation, 16th NNV/CPS - Plasma Physics & Radiation Technology Symposium, Lunteren, The Netherlands, 2004
- D. Mathew, H. M. J. Bastiaens, K. J. Boller and P. J. M. Peters, *Temporal development of discharge instabilities in high pressure helium-fluorine gas mixtures*, Poster presentation, 17th NNV/CPS - Plasma Physics & Radiation Technology Symposium, Lunteren, The Netherlands, 2005
- D. Mathew, H. M. J. Bastiaens, K. J. Boller and P. J. M. Peters, *Parametric study of discharge instabilities in $F_2$-based excimer laser gas mixtures*, Poster presentation, 18th NNV/CPS - Plasma Physics & Radiation Technology Symposium, Lunteren, The Netherlands, 2006

- D. Mathew, H. M. J. Bastiaens, K. J. Boller and P. J. M. Peters, *The effect of the buffer gas on the homogeneity of discharges in excimer laser gas mixtures*, Poster presentation, 19th NNV/CPS - Plasma Physics & Radiation Technology Symposium, Lunteren, The Netherlands, 2007

# Acknowledgments

It is difficult for a person to go and live in a country, whose culture and habits are almost entirely different from what the person is used to. It is hard, and it has to be experienced to be understood. However, I was very fortunate to be in the company of many good people, who helped me directly and indirectly during the course of my PhD. Here, I would like to thank all of them.

First and foremost, I would like to express my sincere gratitude and deep satisfaction to Prof. Klaus J Boller for giving me an opportunity to carry out research at the Laser and Non-linear optics group of University of Twente. The high quality and standard of work you set was always impressive. From you, I learned the skills of writing articles. Thank you very much for being the promotor of my thesis.

I would like to express my sincere thanks to Piet, my project leader, for providing assistance and guidance throughout this project. Thanks a lot for your creative ideas and invaluable contributions, which helped me to finish this thesis. The conference trips together with Shaan was always memorable. You always found ways to overcome many administrative hassles. I would especially like to thank you for the dutch summary of my thesis.

Bert, I don't know how to express my thanks to you. Your constant support and invaluable suggestions always encouraged me. Discussions with you were always stimulating and opened new doors when one door closes. Thank you very much for the immense patience and dedication you showed to me. Your good technical skills and guidance helped me to overcome many difficulties during the course of my PhD. Thank you very much for being the assistant promotor of my thesis.

I would like to thank Prof. Christophe Leys, Prof. Fred Bijkerk, Prof. Johan Meijer and Dr. Ramon Hofstra for being in my Ph.D. committee.

I am grateful to Gerard and Jacob who were always ready to help me with their skillful

technical assistance. Thanks a lot to Ab for his assistance in the problems regarding the computer. I also thank Ben, Mario, and Andrea in the mechanical workshop for their quick assistance with all the mechanical works I had in these past four years.

I want to thank all of my colleagues Fred, Peter van der Slot, Jeroen, Peter, Dennis, Ian, Arsen, Chris, Rolf, Arie, Willem, Ronald, Roel, Martijn, Marvin, Huub van Heel, Leon, Cees, Arco for making the work place friendly and enjoyable. Thanks a lot to Cloudia and Simone for the assistance in the paper work. I would also like to thank Otto and Sandeep for the help in surface roughness measurements. Also, I would like to express my gratitude to Dr. F. van der Heijden, Sreenivas and Prashanth for many helpful discussions about the image processing. I would like to thank Ramesh Sir for all the guidance and support provided prior to the start of my PhD.

In this part, I would like to thank my friends who always helped me to find the cheerfulness of the life. I don't know how to say thanks to Rajesh. You were always there to help and support me. Lars, I enjoyed your friendship very much. It was very easy for us to start an endless conversation about anything below the sun. Thanks a lot for being such a nice colleague and friend to me. I am indebted to Mercy, Manesh, Vinu, Reshmi, Sheela, and Sivaji for their friendship and care. Also, I thank my friends Sari and Seema back in Kerala, who were always there for me. Isabel, you were always there to help and cheer me out. Balaji, you were always a good support. Petra, it was always nice to talk to you. Anton, thanks a lot for all the encouraging discussions. Liviu, thanks for all the tips about dutch bureaucracy. Thanks a lot to my flat mates Joan and Francisca. It was always nice to be with you.

Thanks a lot to Jose uncle, Molly Aunty, Daniel and Dominic for always welcoming me and supporting me in all these years. Special Thanks to Lily for making Sundays always enjoyable. My sincere thanks for all your affection and care towards me. I would also like to thank Beni uncle and Kamalamma aunty for their parental affection.

Thanks a lot for all the wonderful times with Selina aunty and family, Biju, Lee, Babu-Indu, Shaji, Vinay, Toni, Komal, Pramod-Vishaka, Kavitha-Kiran, Supriyo, Vasughi, Vijay, Rama, Manish, Jinesh, Subi, Vipin, Deepu, Dilna, Pathiraj and family, Sheshan and family, Aneesh, Jyotsna-Lee, Merrina, Shahina, Jincy, Rani, Mahesh, Jojo, Azees-Bahuja, Lakshmi, Soni and Anisha. Thanks to my new colleagues in Philips for their support in the last two months.

In the last months of my PhD, I was blessed to be a part of a loving and caring family. I would like to thank Papa and Mumma for your prayers, love and affection. I would like to thank Thankachayan, Kunjechi, Kochettan, Lincy chechi, Augustine, Malootty and Chinchu for their support.

Ichaya, if you were not there, I would never had the courage to go to a foreign country to do PhD. From you, I learned how to work systematically. You always encouraged me to be independent, and supported me in all the decisions that I took. I am very fortunate to have a husband like you. Thank you very much for your friendship, love and support.

Papa and Mumma, you have gone through many difficult times, but have always ensured that my education came first in every decision that you took. I am deeply indebted to both of you for the constant support in all my decisions and endeavors. I thank Dennis for always understanding and supporting my decisions.

Above all, I thank God for all the opportunities that was given to me, for all my friends who can make me smile, and especially for Sabichayan and my family.